UNIVERSITÉ D'ORLÉANS

ÉCOLE DOCTORALE Énergie Matériaux Sciences de la Terre et de l'Univers
Laboratoire de Physique et Chimie de l'Environnement et de l'Espace

THÈSE présentée par :

Andrea Larosa

soutenue le : **22 décembre 2021**

pour obtenir le grade de : **Docteur de l'Université d'Orléans**

Discipline/ Spécialité : Science de l'Univers

Constraints on the Switchbacks generation mechanisms and modeling of the Slow Extraordinary Modes magnetic signatures: Parker Solar Probe observations

THÈSE dirigée par :

Dudok de Wit Thierry	Professeur, Université d'Orléans (LPC2E, Orléans)

RAPPORTEURS :

Valentini, Francesco	Professeur, Università della Calabria (Cosenza, Italie)
Velli, Marco	Professeur, University of California at Los Angeles (Etats-Unis)

JURY :

Célestin, Sébastien	Professeur, Université d'Orléans (LPC2E, Orléans), Président du jury
Chen, Christopher	Senior Lecturer, établissement
Dudok de Wit, Thierry	Professeur, établissement
Krasnoselskikh, Vladimir	Directeur de Recherches CNRS émérite (LPC2E, Orléans)
Valentini, Francesco	Professeur, Università della Calabria (Cosenza, Italie)
Vello, Marco	Professeur, University of California at Los Angeles (Etats-Unis)

Résumé

La mission Parker Solar Probe, qui a été lancée en 2018, est la première à pénétrer profondément dans la couronne solaire, ouvrant de nouvelles perspectives pour étudier in situ le jeune vent solaire jusqu'à 9.85 rayons solaires du Soleil.

Parmi les principales découvertes de la mission figure l'omniprésence de brusques inversions du champ magnétique appelées switchbacks. Ces structures suscitent un fort intérêt mais leur origine n'est pas bien comprise.

Dans cette thèse, nous présentons et étudions deux nouveaux résultats. Premièrement, nous donnons une description détaillée des propriétés locales des switchbacks et nous nous concentrons sur leurs propriétés ainsi que sur leurs frontières. Nous montrons que leur écart par rapport à l'alfvénicité et les corrélations entre le champ magnétique et la densité du plasma sont indicatives de fluctuations de type mode lent et rapide. Ce résultat est important car il permet de contraindre les mécanismes de génération de ces structures. Nous postulons que l'instabilité du tuyau d'incendie pourrait générer certains des switchbacks.

Un deuxième résultat est la première observation de la signature magnétique des modes extraordinaires lents associés aux sursauts radio solaires de type III. Pour comprendre l'apparition de ces signatures, nous fournissons un cadre théorique qui révèle une proportionnalité inverse entre l'intensité du champ magnétique et l'indice de réfraction du plasma. En utilisant des simulations de propagation d'ondes dans des plasmas inhomogènes, nous démontrons que la signature magnétique (jusqu'ici invisible) des ondes devient observable parce que les inhomogénéités de densité font chuter l'indice de réfraction.

Abstract

The Parker Solar Probe mission, which was launched in 2018, is the first to penetrate deep into the inner solar corona, opening new opportunities for studying in situ the young solar wind down to 9.85 solar radii from the Sun.

Among the major findings of the mission is the omnipresence of sudden magnetic field reversals called switchbacks. These structures have received considerable attention but their origin is still unclear.

In this thesis we present and investigate two novel results. First we give a detailed description of the local properties of switchbacks and focus on their properties and on their boundaries. We show that their deviation from alfvénicity and the correlations between magnetic field and plasma density are indicative of slow and fast mode-type fluctuations. This result is important as it helps constrain the possible generation mechanisms. We argue that the firehose instability could generate some of the switchbacks.

A second result is the first observation of the magnetic signature of slow extraordinary modes associated with type III solar radio bursts. To understand the occurrence of these signatures we provide a theoretical framework that reveals an inverse proportionality between the intensity of the magnetic field and the plasma refractive index. Using simulations of wave propagation in inhomogeneous plasmas, we demonstrate that the (hitherto unseen) magnetic signature of the waves become observable because density inhomogeneities cause the refractive index to drop.

Acknowledgments

The three years spent in Orléans have been an amazing journey in which I grew up both as a person and as a scientist. The beauty of the journey is completely due to the amazing people I had the honor to meet and become friend with and I wish to thank them all from the bottom of my heart.

I would especially like to thank my supervisors Thierry and Volodya for believing in me and for all the help in both work and life issues. Their understanding and kindness are limitless.

I wish to thank Vamsee, Melody, Luca, Federico, Matthieu, Sebastien, Pietro, Gaetane, Anna, Nini, Minna, Clara, Claire, Pierre (Senior and Junior), Manu and Jeremie, Nina, Frank. I shared a lot with you guys, you supported me and you were there in all the tough and happy moments. Thanks a lot.

I'm really grateful to all the people in that laboratory that were always there to help.

My gratitude goes also to my uncles Damiano, Maurizio, Salvatore and my cousin Domenico and Maria. They always cheered me up when needed by reminding me the importance of having a job that makes you happy even if far from home.

I want to thank also my friend Domenico, just for the wonderful person he is. He has always given me a lot under both, the human and academic point of view.

I take the chance to thank my siblings Cosimo and Chiara for taking care of things at home and for the rides to the airport. I love you guys.

I thank my mom for the unconditioned love she always makes me feel and for being so kind with everyone, mom you are the definition of kindness.

During the thesis period I spent a lot of time apart from you Tania. You didn't join me but you were always there waiting for me. I know we approach life in different ways, but I'm sure our love will prevail on our differences.

The sweetest thanks goes to Domi, Giada, Nico and Tommaso, my lovely nephews. Playing with you is the best anti-stress drug. Describing the happiness you give me is impossible, you are a pure blessing.

Finally I thank my father, Nicodemo. Dad I hope you are somewhere watching over us as you used to when you where here, I hope you went past all the bad things you lived. This achievement is yours more than main, thanks for everything.

Contents

Chapter 1

Introduction: Physics of the Inner Heliosphere

The solar wind is a continuous flow of charged particles that leave the Sun and fill the entire Heliosphere. These particles are mainly protons and electrons. Other minor constituents are alpha particles (double ionised helium nuclei), which represent typically 5% of the proton density and smaller concentrations of heavier ions. The first in situ measurements of the solar wind were made in 1959 by the soviet Luna 1 probe. However, the existence of such a flow of matter was already expected from the deflection of comet tails from the anti-radial direction (Hoffmeister, 1943). Such deflections could not be explained in terms of radiation pressure only and required the presence of solar corpuscular radiation. Biermann (1951) hypothesised that Coulomb collisions should be responsible for momentum coupling between the solar plasma and the comet tail, but this required a plasma density that would be much larger than what is observed. The problem was solved considering the presence of a frozen in magnetic field embedded in the flow (Alfvén, 1957).

These early observations of the solar wind challenged the mechanisms by which such a continuous outflow of matter could occur in the vicinity of a massive star with a strong gravity field. At the same period, spectroscopic observations of the Sun at UV wavelengths revealed the presence around the Sun of a corona whose temperature exceeded that of the surface (the photosphere) by more than two orders of magnitude, reaching millions of degrees Kelvin (Foukal, 2004). A direct consequence of such high temperatures is the high conductivity of the solar wind. This provided the basis for the hydrostatic model by Chapman and Zirin (1957), which was one of the first physical models of the solar corona.

Unfortunately, the solution of Sydney Chapman's model predicted a density excess at 1 AU of the order of 100 cm^{-3} and unrealistic high pressures in the interstellar medium. The latter problem was pointed out by Eugene Parker who proposed a dynamical model for an expanding corona (Parker, 1965). Since the corona cannot remain in static equilibrium but must be continually expanding to sustain an interstellar pressure, Eugene Parker assumed a steadily expanding solar wind. In spite of its many assumptions (e.g. isothermal and single fluid) the model is considered as a milestone of solar physics as its prediction of a supersonic solar wind flow was later confirmed by the Mariner 2 mission (Neugebauer and Snyder, 1966).

These early models and observations highlighted two major problems of solar wind physics: what accelerates the solar wind and what heat the solar corona. Intensive investigations and discussions are still surrounding the aforementioned problems, supported by the growing number of spacecraft missions as well as dramatic advances in the modeling capabilities due to modern supercomputers. Currently there are two competing classes of models to explain solar wind acceleration and heating: one involves MHD waves and turbulence (Cranmer, van Ballegooijen, and Edgar, 2007) and the other interchange reconnection (Fisk, Schwadron, and Zurbuchen, 1999; Fisk, 2003). In the first class of models the solar wind is released only from open field lines and the its type depends on the degree of expansion of the lines (Wang and Sheeley, 1990). In the second the solar wind is released from a reconnection process between an open and a closed field line. In this case fast or slow winds are released depending on the type of plasma inside the reconnecting magnetic tube.

The true picture, however, is more complex, and it would be better to consider a continuum of solar wind regimes, in which the wind speed is an important but certainly not the sole criterion. Viall and Borovsky (2020), for example, show that the release can be due to open flux, interchange reconnection and to closed-flux reconnection. Once the plasma is released the different types of mechanisms can act to produce different types of solar wind parcels. Several mechanisms could be at play and the determination of the dominant one is complicated by the fact that the physical processes involved in the solar wind cover over 8 orders of magnitude in spatial and in temporal scales when going from the energy injection scales of the system to kinetic scales.

Let us stress that the understanding of the solar wind and its sources is not only relevant for solar physics, but also applies to Sun-like stars. Conversely, the evolutionary stages of Sun-like stars is helping us today better understand the past and future evolution of the Sun (Vidotto, 2021). In this sense, the quest for understanding the origin and the heating of the solar wind is truly an astrophysical problem.

1.1 Solar wind types

The solar wind can be divided into different types according to its coronal sources (Xu and Borovsky, 2015; Rouillard et al., 2021). Traditionally, the picture is simplified by considering two classes only : fast winds (500-800 km/s) and slow winds (250-400 km/s). Fast winds tend to be highly alfvénic, i.e. they exhibit a high correlation between velocity and magnetic field fluctuations, and have a nearly constant amplitude $|\mathbf{B}|$ of the magnetic field as compared to the individual components of B. Fast winds also exhibit higher proton temperatures and lower densities than slow winds. Additionally, these winds also differ in their isotopic composition, their degree of anisotropy, etc. The coronal sources of fast winds are regions of open magnetic field lines such as coronal holes. For that reason fast winds are primarily observed above polar regions, and more occasionally at lower latitudes, depending on the presence of coronal holes at such latitudes.

The exact origin of the slow solar wind is still one of the outstanding open questions in solar physics. Slow winds can originate from various regions, such as the boundary of coronal holes (Wang, 1994) and patches of open magnetic field lines that are associated with active regions (van Driel-Gesztelyi et al., 2012; Culhane et al., 2014). The slowest and densest solar winds are usually associated with coronal structures that are called streamers. In Chapter 3 we shall pay special attention to so-called slow alfvénic winds (D'Amicis and Bruno, 2015) that have characteristics similar to the fast wind (composition and high degree of alfvénicity) while their speed is that of a slow wind.

1.2 The heliospheric magnetic field

The dynamics of the solar wind is governed by the heliospheric magnetic field, which is the extension of the coronal magnetic field into the Heliosphere

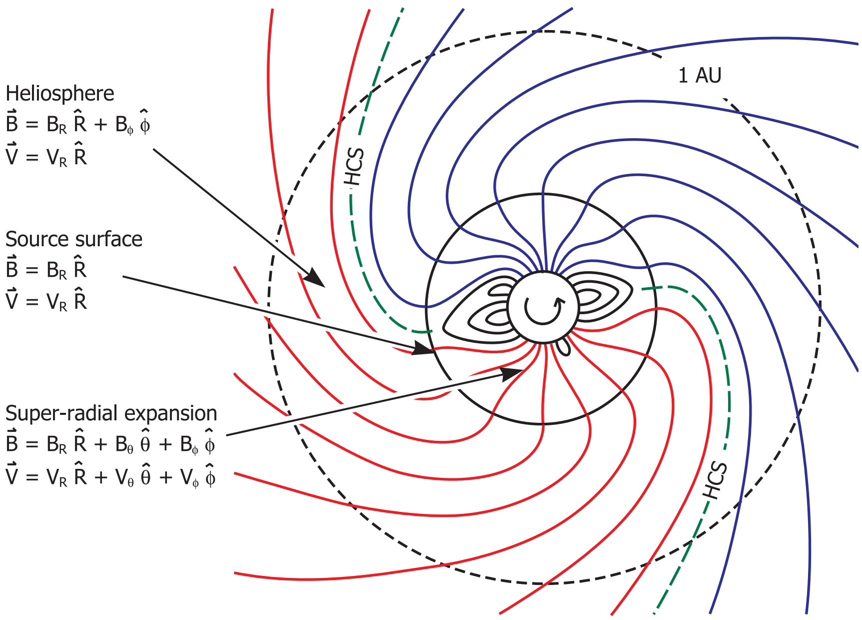

Figure 1.1 Sketch of the heliospheric magnetic field in the ecliptic plane. Regions with opposite polarity as shown in different colours. Figure taken from (Owens and Forsyth, 2013)

(Owens and Forsyth, 2013). This magnetic field is dragged away from the Sun by the solar wind because it is essentially frozen into the solar wind plasma. The footpoints of the field lines are fixed in the solar photosphere but, due to the solar rotation, in the Heliosphere they give rise to an Archimedean spiral structure (Parker, 1958). Figure 1.1 illustrates the structure of the heliospheric magnetic field in the ecliptic plane.

This large-scale structure of the Heliosphere is distorted by the interaction of fast and slow solar wind streams, and by the interplanetary manifestation of transient events such as coronal mass ejections. On still smaller scales, the heliospheric magnetic field exhibits a rich variety of waves, and discontinuities. Finally, and not least, it represents an excellent laboratory for studying plasma turbulence (Bruno and Carbone, 2013) and for understanding how energy spectral energy is transferred across different scales.

The presence of a macroscopic heliospheric magnetic field has a major impact on the solar wind because it causes an anisotropy in space that affects wave propagation, instability development, shock formation, and more. At the largest scale of the system we have the dipolar field of the Sun, which expands in the Heliosphere. The heliospheric current sheet separates the two regions with opposite polarities.

Fluctuations of the heliospheric magnetic field are observed at all scales from DC to the MHz range, with a rich diversity of structures and waves. Although many studies have been devoted to their investigation near 1 AU (Balogh and Erdõs, 2013; Matthaeus et al., 2015), with a particular focus on turbulence (Bruno and Carbone, 2013; Kiyani, Osman, and Chapman, 2015; Chen, 2016), much less is known about the properties of the solar wind deeper in the Heliosphere, and about the radial evolution of these properties.

The first mission to provide major insight into the radial structure of the heliospheric magnetic field was Helios with its twin spacecraft, between 1975 and 1986. The closest encounter with the Sun was made by the Helios-B spacecraft at 0.31 AU or 66.6 solar radii and provided a wealth of new results (Musmann, Neubauer, and Lammers, 1977). After the early years of the space age the scientific community had to wait for three decades until the launch of two spacecraft that are presently providing us with an unprecedented view of the inner Heliosphere (Velli et al., 2020): Parker Solar Probe (PSP), which was launched in 2018 (Fox et al., 2015) and Solar Orbiter, which was launched in 2020 (Müller et al., 2013).

In this thesis, we shall focus only on the Parker Solar Probe mission (see Chapter 2), which is dedicated to the in situ investigation of the solar wind down to 9.8 solar radii. In comparison, Solar Orbiter will have a perihelion at 60 solar radii but will be better equipped with remote sensing instruments and will move out of the ecliptic plane.

For its first solar encounter in November 2018, Parker Solar Probe has revealed a highly structured solar wind with an unexpected large amount of sudden deflections of the magnetic field, which have been called switchbacks (Bale et al., 2019). Figure 1.2 illustrates the radial component of the magnetic field for that first encounter and reveals the omnipresence of the so-called magnetic switchbacks. The increase in magnitude at the time of closest approach is also clear. The perihelion was then at 35.8 solar radii.

1.3 Particles in the solar wind

Protons are the main ion species of the solar wind. Their density is of the order of few particles per cubic centimeter at 1 AU. Mass conservation implies a

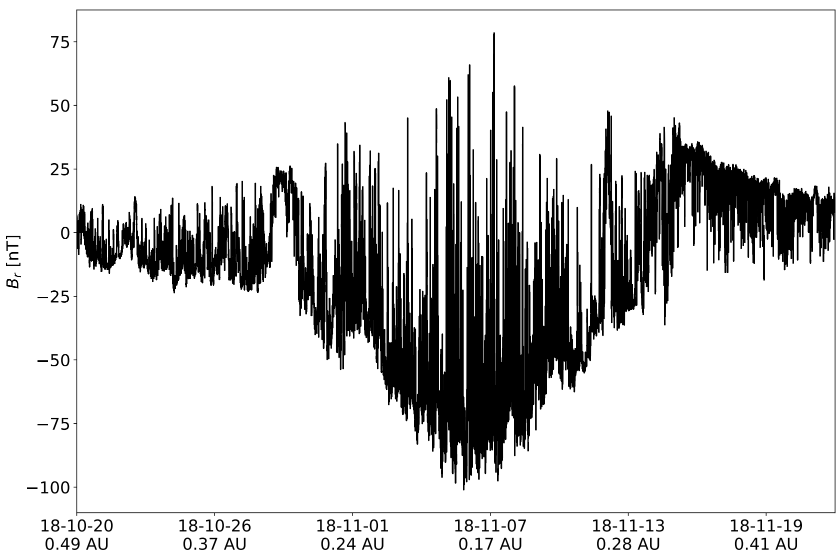

Figure 1.2 Radial component of the magnetic field as measured by PSP during its first perihelion pass in November 2018. The ticks of the x axis indicate the date and the radial distance is given in AU

radial scaling of the density with R^{-2}. Proton velocity distributions functions (VDFs) are usually non-maxwellian because of the non-collisionality of the solar wind plasma. In addition they are non isotropic because of the ambient magnetic field. As a consequence, temperatures are not the same, depending on the direction in velocity space. Since the presence of the magnetic field introduces a privileged direction, the anisotropy is usually described by defining a temperature along a cut of the VDF in the direction parallel to the magnetic field ($T_{||}$) and another one along a cut perpendicular to it ($T_{\perp}$).

The ratio $R_p = T_{\perp}/T_{||}$ of the two temperatures is called the proton temperature anisotropy and is known to drive various instabilities when its value deviates sufficiently from one (Gary, 1993; Klein and Howes, 2015). These instabilities tend to bring R_p closer to one. This is usually shown by means of the so-called "Brazil plot" (see Figure 1.3) whose two axes represent two key quantities for understanding the stability of the the plasma, namely the temperature anisotropy and the parallel proton beta

$$\beta_{||,p} = \frac{n_p k_B T_{||}}{B^2/2\mu_0} \tag{1.1}$$

where n_p is the proton density, k_B Boltzmann's constant and B is the mod-

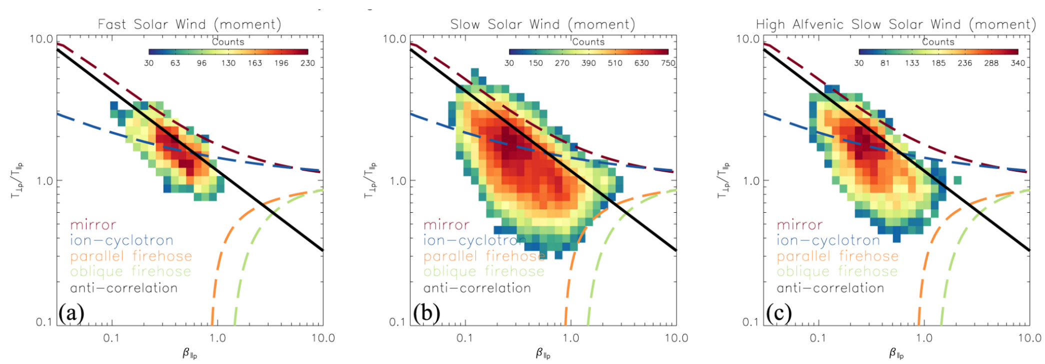

Figure 1.3 Parallel proton beta vs temperature anisotropy for fast (a), slow (b) and slow alfvénic solar wind between 30 and 40 solar radii from the Sun. The instabilities thresholds, adapted from Hellinger and TráVníčEk (2006), are indicated by dotted lines. The black lines indicates the relation between the plasma beta and the anisotropy derived in Marsch, Ao, and Tu (2004). Figure from Huang et al. (2020).

ulus of the magnetic field; $\beta_{||,p}$ quantifies the ratio between magnetic and proton kinetic pressure along the direction of the magnetic field.

The data shown in Figure 1.3 were obtained from PSP's first perihelion pass at 35.8 solar radii. We can see that the observations are constrained by theoretical thresholds of the different proton micro-instabilities. A temperature anisotropy below one offers favourable conditions for the generation of the parallel and oblique firehose instability; $R_p > 1$ offers favourable conditions for the ion-cyclotron and mirror instabilities.

Another interesting characteristic of proton VDFs is the presence of proton beams whose properties are sensitive to the structure of the radial magnetic field (Verniero et al., 2020).

The second most common type of ions in the solar wind are alpha particles, which typically represent between 2% and 5% of the ion density according to the type of wind. Alpha particles also exhibit temperature anisotropy but shows different radial trends as compared to protons. When moving towards the Sun, the proton perpendicular temperature $T_{\perp,p}$ increases faster than their parallel temperature $T_{||,p}$ (Huang et al., 2020), while for alpha particles the opposite occurs (Stansby et al., 2019). As a consequence, the opportunity for alpha and proton distributions to generate instabilities do not evolve in the same way when moving radially.

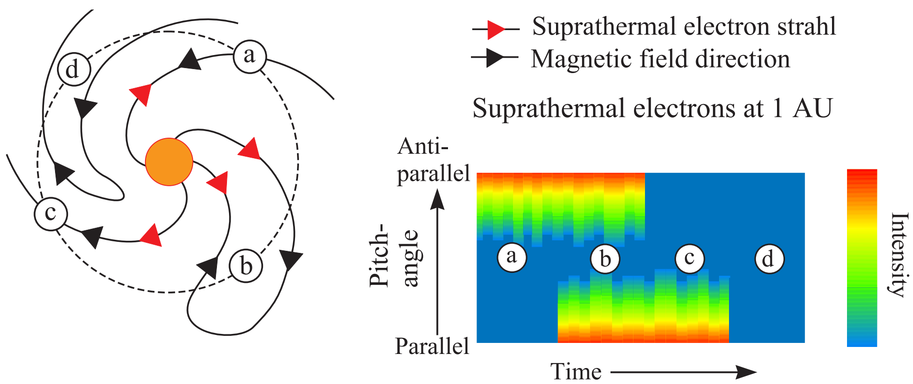

Figure 1.4 Sketch illustrating the use of strahl electrons for determining the topology of the heliosheric magnetic field. The left panel shows a view of the ecliptic plane with four different cases of topology/connectivity of the magnetic field lines. The right plot shows the pitch-angle distribution of the strahl, i.e. whether the strahl propagates parallel or antiparallel to the magnetic field. Figure taken from (Owens and Forsyth, 2013).

Numerical simulation have shown that alpha particles can also be firehose unstable (Matteini et al., 2015); higher abundances of alpha particles seem to be associated with higher rates of switchbacks (Bale et al., 2021), whose exact origin is still hotly debated. These different properties of alpha particles and protons will be addressed in Chapter 3 with the aim to better constrain the origin of switchbacks.

Electrons are much more mobile than ions and for that reason play a major role in the spatial transfer of thermal energy due to the high heat flux (Verscharen et al., 2021). The electron VDF in the solar wind is traditionally divided into three components (Pierrard, Maksimovic, and Lemaire, 2001; Maksimovic et al., 2005): an thermal core, a smaller population of energetic halo electrons, and a highly focused beam of outward propagating energetic electrons, called strahl, which are moving along the magnetic field. Since the strahl always flows in the anti-sunward direction along the field, it can be used to diagnose whether a magnetic field line is connected to the Sun, or has a kink, see Figure 1.4 for open field lines. This property was used, for example, to determine whether switchbacks are kinked magnetic field lines and are magnetically connected to the Sun (Kasper et al., 2019; Whittlesey et al., 2020).

Considerable attention has been given to the key role of electrons in magnetic reconnection, shocks and turbulence in a variety of astrophysical environments such as solar flares (e.g., Lin and Hudson, 1971), interplanetary shocks (e.g., Yang et al., 2019) and planetary magnetospheres (e.g., Ergun et al., 2018). Flare-accelerated electrons propagate in the Heliosphere, at extremely high speeds, resulting in bursts of radio emission (known as Type III radio bursts) and plasma oscillations such as Langmuir waves. These aspects of electron dynamics and how they affect the solar wind environment will be the focus of Chapter 4.

1.4 Outline of this thesis

Let us now briefly summarise the main physical questions that will be addressed in this thesis. First, this work provides insight into two new observations that were made thanks to the PSP mission: they deal with magnetic switchbacks and with the magnetic signatures of waves that are observed during solar radio bursts. The terminology will be made clear in the dedicated chapters. Here we describe briefly the main problems and raised questions.

A. Omnipresence of magnetic field reversals (switchbacks) in the inner Heliosphere.

- Switchbacks are known to be alfvénic structures while also showing evidence for compressibility. Are compressional switchbacks a significant component with respect to the purely alfvénic ones?
- The boundaries of switchbacks separate them from the surrounding plasma. Are these open or closed boundaries? Which kind of plasma exchange occurs at them?
- Are these structures consistent with the marginal stable state of plasma micro-instabilities?

The above-mentioned questions are important for putting constraints on the physical mechanisms that may give rise to them. This is presently a hotly debated issue to which we provide new answers.

These results have been published in (Larosa et al., 2021).

B. First observation of the long-sought magnetic signature of the slow extraordinary modes associated with solar radio bursts.

- Is the rarity of this magnetic signature related to observational limitations?
- Are these observations related to wave propagation in an inhomogeneous plasma?
- Which plasma properties are more favorable for their generation?

Our study on the generation and propagation of these wave modes provides a theoretical background for their understanding in relation to plasma inhomogeneities and beam property.

These results have been submitted to (Larosa et al., 2022).

The thesis consists of 5 chapters, including the present introduction. In Chapter 2 we provide a brief description of the instruments from PSP that are of interest for this work. Chapter 3 is dedicated to the investigation of switchbacks. We provide a detailed description of their properties and reveal a significant presence of compressional structures. We also show that their boundaries can be interpreted in terms of MHD discontinuities and discuss which generation mechanisms are most plausible. In Chapter 4 we show the first observation of the magnetic signature of slow extraordinary modes and discuss how their generation can be associated with the propagation in an inhomogeneous plasma. We conclude and provide some outlooks in Chapter 5.

1.5 Résumé en français: introduction

Ce chapitre pose le cadre des études menées dans cette thèse. Nous commençons par une description du vent solaire, qui est le système physique sur lequel nous allons nous concentrer. Le vent solaire est un gaz ionisé constitué essentiellement de protons et d'électrons, émis en permanence par le Soleil et qui balaye tout l'espace interplanétaire. Ce plasma est supersonique et non-collisionnel. Le vent solaire nous permet de faire de la physique des plasmas dans des conditions impossibles à reproduire en laboratoire.

Les mesures des champs électromagnétiques et des particules du vent solaire sont effectuées grâce à des sondes spatiales. La majorité de sondes se trouvent à proximité de la Terre, à une distance d'environ une unité astronomique (1 UA, environ 150 millions de kilomètres) du Soleil. Avant août

2018, qui est la date de lancement de la mission Parker Solar Probe, la distance plus proche au Soleil jamais atteinte par une sonde spatiale était de 0.3 UA avec HELIOS. Parker Solar Probe nous a depuis permis d'étudier les propriétés du vent solaire jusqu'à moins de 0.1 UA. A terme, elle descendra à moins de 0.05 UA.

Cette thèse est entièrement basée sur les observations de Parker Solar Probe, et plus particulièrement sur les mesures du champ magnétique qui est une variable-clé pour la compréhension de la dynamique du vent solaire.

Le manuscrit est constitué de 5 chapitres et démarre par la présente introduction. Le chapitre 2 donne une description de la mission Parker Solar Probe et de ses instruments. Le cœur de la thèse se trouve dans les chapitres 3 et 4 : le chapitre 3 aborde les structures magnétiques appelées switchbacks, qui sont un des découvertes majeures faites par Parker Solar Probe. L'origine exacte de ces structures n'est pas connue à ce jour; or elle devrait nous apporter des réponses importantes sur la nature des instabilités qui sévissent dans la couronne solaire. Nous allons nous concentrer sur les propriétés de compressibilité des switchbacks, sur leurs frontières et sur les mécanismes qui leur donnent naissance.

Le chapitre 4 est consacré à la récente observation inédite de la composante magnétique d'ondes de haute fréquence appelées modes extraordinaires lents. Nous nous interrogeons sur leurs origine et sur les raisons qui nous permettent de les observer.

Enfin, le chapitre 5 clôt cela par une conclusion des travaux effectués et des perspectives d'avenir.

Chapter 2

The Parker Solar Probe Mission

2.1 Introduction

Parker Solar Probe (PSP) holds the record for the closest approach to the Sun by a man-made object. The spacecraft was launched on 12 August 2018 and is providing a wealth of new information on the solar wind and its origins. PSP, which has a nominal lifetime of 7 years, will reach in 2024 a minimum distance from the Sun in of 9.85 solar radii (Fox et al., 2015).

The three main scientific objectives of this mission are to :

- discover the coronal heating and the solar wind acceleration mechanisms;
- determine the magnetic field topology and dynamics at the sources of the solar wind;
- investigate the possible mechanisms for energetic particles acceleration.

In order to reach these goals it is necessary to measure the electromagnetic fields and plasma properties in a vast range of temporal and spatial scales, which PSP is able to cover thanks to four instrument suites. These suites are (Fox et al., 2015): SWEAP, FIELDS, IS$\odot$IS and WISPR. SWEAP (Kasper et al., 2016a) and IS$\odot$IS (McComas et al., 2016) respectively make in situ observations of the thermal and energetic particles, while FIELDS (Bale et al., 2016) measures in situ electromagnetic fields. WISPR is the only camera onboard PSP, and observes the solar corona in white light (Vourlidas et al., 2016). In this work me make use of the first three suites only, which will be detailed below.

2.2 FIELDS

Figure 2.1 gives an overview of the FIELDS instrument suite (Bale et al., 2016). As its name suggests, this suite probes electromagnetic fields. Its main instruments are four electric field antennas (V1-V4) that are located at the front, near the heat shield. The rear of the spacecraft has a 4-meter boom that carries two fluxgate magnetometers MAGi and MAGo, a search-coil magnetometer (SCM), and a small electric field antenna (v5).

The four electric field antennas V1-V4 are coupled with the ambient plasma primarily through photoelectrons that are generated by UV radiation. They are located at the front in order to probe the solar wind without being affected by the spacecraft wake while. The V5 antenna is located in the shade and therefore is primarily coupled through thermal electrons. Because of its much shorter length it is more affected by the sheath surrounding the spacecraft.

The signals from these different instruments are processed in different ways. While the two fluxgate magnetometer generate waveforms that are sampled up to 293 Hz, all other instruments provide either waveforms or spectral products. The latter are computed by the Digital Fields Board (DFB) (Malaspina et al., 2016) and by the Radio Frequency Spectrometer (RFS) (Pulupa et al., 2017). High frequency burst waveforms are captured by the Time Domain Sampler (TDS) (Bale et al., 2016). Each of these instruments will be of interest for our study.

The TDS provides triggered waveforms in five channels with a typical cadence of 1.92 MHz and a duration of 16 milliseconds. These waveforms generally consist of the voltage differences from mutually perpendicular electric dipole antennas V1-V2 and V3-V4, voltages from monopole antennas V2 and V5, and the high frequency magnetic field from the SCM. TDS has an adjustable trigger. During the first two encounters the instrument mainly detected impulsive dust impacts while for later encounters it was more sensitive to Langmuir wave events.

The RFS is a digital receiver and spectrometer whose inputs are the four antennas V1-V4, and possibly a high frequency antenna of the SCM although

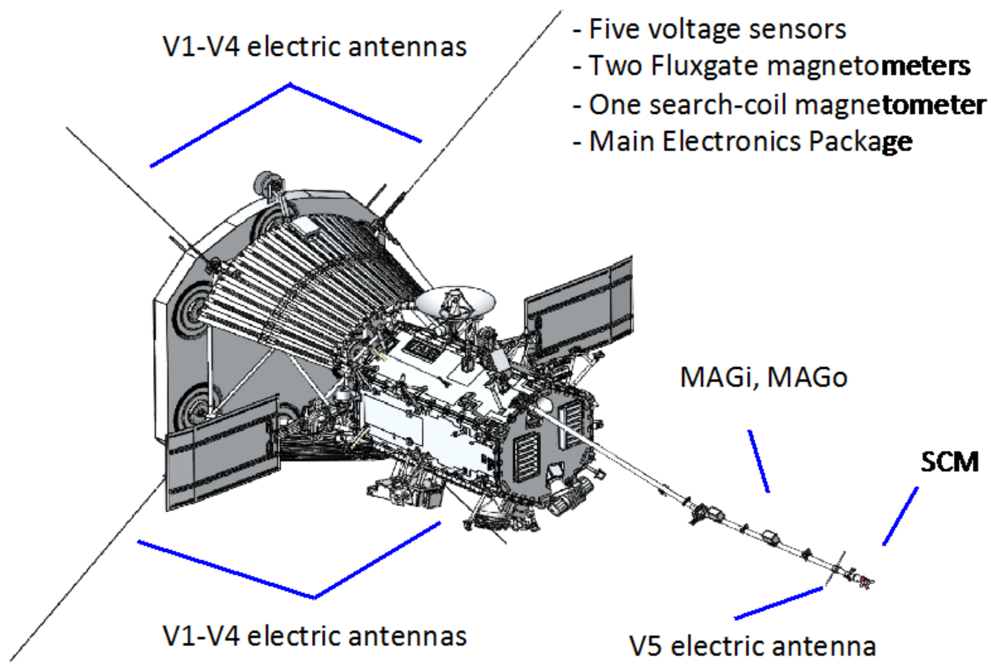

Figure 2.1 The FIELDS suite on PSP. Figure from Bale et al. (2016)

this possibility has not been used so far (Pulupa et al., 2017). The main data products are autospectra and cross spectra. The instrument can measure electromagnetic and electrostatic fluctuations between 10 kHz to almost 20 MHz (Bale et al., 2016). This frequency range allows the investigation of type III solar radio bursts that will be of interest for Chapter 4. RFS also allows to monitor the evolution of the plasma frequency, from which the local electron density is estimated (Moncuquet et al., 2020).

2.2.1 MAG

PSP has two triaxial fluxgate magnetometers (MAGs), both of which are located on the boom in the anti-sunward direction. These instruments were built by NASA/GSFC and are similar to those that are successfully operating on STEREO, MAVEN, MESSENGER and on other spacecraft (Bale et al., 2016). Fluxgate magnetometers measure the voltage induced by changing the relative permeability of a periodically saturating ferromagnetic core (Miles et al., 2018). Because of this, they can measure the low frequency part only of magnetic fields, typically from DC up to approximately 100 Hz. On PSP, the waveforms are usually sampled at 146 Hz or at 293 Hz.

We use the full cadence waveforms of the MAG instrument for the individuation of the magnetic structures such as switchbacks and for the investigation of their boundaries in Chapter 3.

2.2.2 SCM

The Search Coil Magnetometer (SCM) consists of three antennas that measure magnetic field fluctuations along their axis (Jannet et al., 2021). Each antenna is made of a magnetic material core with a coil wound around it. The measurement principle is based on Faraday's law of induction, which can be expressed as follows:

$$V = -N\frac{d\Phi_B}{dt} = -N\frac{d(SB)}{dt}.$$

Here, N is the number of windings, Φ_B is the magnetic flux and V is the output voltage induced by the time derivative of the magnetic flux. The latter is the product of the cross-section of the antenna S multiplied by the magnetic field B. Since S is constant the only contribution to the output voltage comes from the fluctuating magnetic field. In comparison to flux-gate magnetometers, search-coils have their optimum sensitivity at higher frequencies. For that reason the two instruments are often used together with complementary frequency ranges.

The SCM has two single-band antennas that operate between 3 Hz and 50 kHz; we shall call this the low frequency (LF) range. The third antenna is a double-band one, which covers both the LF and the medium frequency (MF) range between 10 kHz and 1 MHz. The LF range is suitable for studying ion-cyclotron waves, whistler waves and turbulence in the kinetic range, whereas the MF range is more appropriate for studying waves around the plasma frequency.

In this work, the SCM LF waveforms will be used to characterize magnetic fluctuations in the vicinity of discontinuities such as switchbacks, see Chapter 3. MF waveforms recorded by TDS will serve in Chapter 4 to show the presence of a magnetic field component for slow extraordinary modes.

2.3 SWEAP

The Solar Wind Electrons Alphas and Protons (SWEAP) suite consists of four instruments: the Solar Proton Cup (SPC), and SPAN-Ai, SPAN-Ae and SPAN-B (Kasper et al., 2016b), where SPAN stands for Solar Probe ANalyzer. The SPAN instruments are electrostatic analyzers, while SPC is a Faraday cup. In this work we use data from SPC and SPAN-Ai.

A detailed description of the SPC instrument is given in Case et al. (2020). The instrument is similar to the Faraday cup of many previous missions. For PSP, however, since the instrument is directly exposed to sunlight, its special design has to withstand extreme temperatures Case et al. (2020). SPC measures flow angles and fluxes as a function of energy from 50 eV/q to 8 keV/q for ions and 50 eV to 2 keV for electrons (Kasper et al., 2016b).

The SPAN-Ai measures ions as a function of energy/charge ratio and direction from several eV/q to 20 keV/q. In addition, it has a time of flight section that enables to distinguish different ion species according to their mass/charge ratio.

SPC points always radially towards the Sun, while SPAN-Ai points towards the ram direction. As a consequence, SPC is more suitable when the solar wind flow is mostly radial, whereas SPAN-Ai has a better field of view when the flow is more tangential (e.g. because of the angle of the Parker spiral with respect to the radial direction). Therefore, it is important to choose the appropriate instrument to evaluate the plasma properties in presence of magnetic field deflections, like the one we are going to investigate in Chapter 3.

2.4 IS⊙IS

The Integrated Science Investigation of the Sun (IS⊙IS) (McComas et al., 2016) is made of two energetic particle instrument (EPI) which in order of increasing measured energy are called EPI-Lo and EPI-Hi, lo for lower and hi for higher. EPI-Lo covers a range of energies of 20keV/nucleon to 15 MeV for ions and ion composition and a range of 25 to 1000 eV for the the electrons. EPI-Hi can measure ions with energy between more or less 1 and 200 MeV and electrons from about 0.5 to 6 MeV (McComas et al., 2016).

We used data from EPI-Lo to investigate the presence of energetic electrons for the events of interest in Chapter 4.

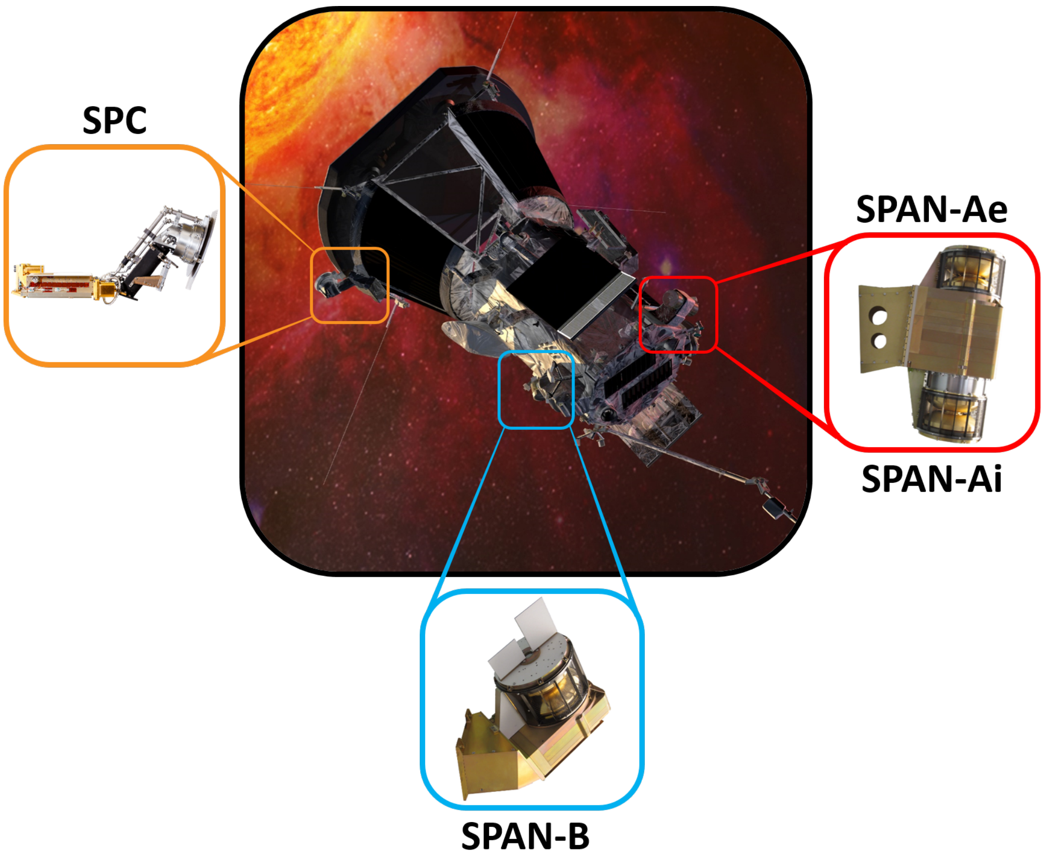

Figure 2.2 The SWEAP suite on board PSP. Figure from from http://sweap.cfa.harvard.edu/SWEAP.html

2.5 Résumé en français: Parker Solar Probe

Jamais une sonde spatiale n'aura frôlé le Soleil de si près que Parker Solar Probe. La sonde, lancée en 2018, sera au plus proche du Soleil en 2024, avec une distance de 9.85 rayons solaires. Elle a pour objectif scientifique de répondre aux questions fondamentales sur la physique du vent solaire, comme les origines du chauffage de la couronne, les mécanismes d'accélération du vent solaire, la topologie du champ magnétique aux sources du vent solaire et les mécanismes d'accélération des particules énergétiques.

Les instruments de la sonde peuvent être regroupés en quatre suites: SWEAP, FIELDS, IS⊙IS et WISPR. SWEAP et IS⊙IS effectuent respectivement des observations in situ des particules thermiques et énergétiques, tandis que FIELDS mesure in situ les champs électromagnétiques. WISPR est la seule caméra à bord du satellite, et observe la couronne solaire en lumière blanche. Dans ce travail, nous n'utiliserons que les trois premières suites.

Les principaux instruments de la suite FIELDS sont: 4 antennes électriques placées sur la partie de la sonde faisant face au soleil, et à l'arrière un bras de 4 m sur lequel sont placés une cinquième antenne électrique, deux magnétomètres de type fluxgate et un magnétomètre de type search coil. Ce dernier a été conçu et réalisé par le LPC2E. Les mesures effectuées par ces instruments sont traitées de différentes manières pour fournir des formes d'onde et des données spectrales à différentes fréquences allant de quelques Hz à plusieurs MHz pour le champ magnétique et électrique. Les données qu'ils fournissent sont au cœur de ce travail de thèse.

La suite SWEAP est composée de trois analyseurs électrostatiques et d'une cavité de Faraday. Comme le satellite ne tourne pas sur lui-même, un seul détecteur de particules ne suffit pas à couvrir tout le champ de vision disponible. Pour surmonter ce problème, on dispose plusieurs détecteurs sur les différentes faces du satellite. Les mesures d'ions sont effectuées dans la direction du soleil par une cavité de Faraday et dans la direction du vent solaire par l'un des analyseurs électrostatiques (SPAN-Ai). Les mesures des électrons sont effectuées dans la direction du Soleil par une cavité de Faraday et dans les directions du vent solaire par deux analyseurs électrostatiques (SPAN-Ae et SPAN-B). La gamme combinée des énergies accessibles va de quelques eV/q à 20 keV/q pour les ions et de plusieurs keV à 20 keV pour les électrons.

La suite IS⊙IS est composée de deux instruments à particules énergétiques

(EPI) qui, par ordre croissant d'énergie mesurée, sont appelés EPI-Lo et EPI-Hi. EPI-Lo couvre une gamme d'énergies allant de 20 keV/nucléon à 15 MeV pour les ions et la composition des ions, et une gamme de 25 à 1000 eV pour les électrons. EPI-Hi peut mesurer des ions dont l'énergie est comprise entre 1 et 200 MeV, et les électrons entre 0.5 et 6 MeV. Nous avons utilisé les données de EPI-Lo pour étudier la présence d'électrons énergétiques pour les événements décrits dans le chapitre 4.

Chapter 3

Statistical Properties of Switchbacks

3.1 Introduction

This chapter focuses on the magnetic field deflections that are called switchbacks (SBs) jets, or velocity spikes (Bale et al., 2019; Kasper et al., 2019; Dudok de Wit et al., 2020; Horbury et al., 2020; McManus et al., 2020) and which are one of the most striking results of PSP. SBs are sudden deflections of the (otherwise mostly radial) magnetic field. They occur in slow alfvénic solar winds and can last from seconds to hours. SBs had been observed before in fast streams of the polar solar wind by the Ulysses spacecraft (Balogh et al., 1999). They were recognised as folds in the field, which were distinguished from other in situ structures (Yamauchi et al., 2004). SBs were also observed in fast wind streams by Helios (Horbury, Matteini, and Stansby, 2018) and were associated with one-sided radial jets (Gosling et al., 2009). PSP has revealed how numerous these structures become when approaching the Sun. Clearly, their investigation is one of the keys towards understanding the evolution of the young solar wind. Not surprisingly, many simulation studies have been devoted to them (Zank et al., 2020; Squire, Chandran, and Meyrand, 2020; Ruffolo et al., 2020a; Sterling and Moore, 2020; Drake et al., 2021; Tenerani et al., 2021). Furthermore, their understanding could contribute to reach some of the main objectives of the PSP mission such as the understanding of coronal heating and the topology of the magnetic field at the solar wind source regions (Fox et al., 2016).

SBs stand out with respect to other fluctuations by their high alfvénicity (i.e. the magnitude of the magnetic field barely changes) and by the sudden deflection of the magnetic field by an angle between 0° and 180°. While the largest deflections only are true SBs, the latter term is today used indiscriminately for almost all deflections. These deflections occur simultaneously with that of the proton bulk velocity, which is also enhanced within the structure. Additionally, the variations in the total magnetic field and in proton velocity are highly correlated (Kasper et al., 2019).

The distribution of the electron pitch angle indicates (Whittlesey et al., 2020) that SBs are not polarity changes of the magnetic field, but correspond to deflections or reversals of the same magnetic field line. The radial Poynting flux associated with these structures represents approximately 10% of the kinetic energy flux (Bale et al., 2019), which may seem too small to carry a significant amount of the energy. However, closer to the Sun, these structures might carry a larger fraction of the energy flux because the ratio of alfvénic flux to proton kinetic flux is inversely proportional to the alfvénic Mach number. For that reason, radial Poynting flux increases close to the Sun, along with the intensity of the magnetic field.

The proton radial temperature is found to be higher inside SBs (Kasper et al., 2019; Mozer et al., 2020; Krasnoselskikh et al., 2020), except for the largest deflections with complete reversal (Woolley et al., 2020). These properties, combined with the increased radial velocity, are reminiscent of the more general strong correlation found between proton temperature and solar wind speed at larger scales (Grappin, Mangeney, and Marsch, 1990; Grappin, Velli, and Mangeney, 1991). Woodham et al. (2021) reveal that the parallel temperature is enhanced inside patches of SBs, while the perpendicular one is mostly constant, even though it is higher than the parallel one.

The origin of SBs is still a hotly debated today, with two competing families of models. One involves processes that occur locally in the solar wind, such as Kelvin-Helmholtz instabilities, turbulence, the expansion of the magnetic field, and combinations thereof (Ruffolo et al., 2020b; Squire, Chandran, and Meyrand, 2020). The other family involves processes acting deeper inside the corona, typically in the transition region, such as magnetic field reconnection and jets of plasma that propagate into the solar wind as alfvénic structures (Kasper et al., 2019; Fisk and Kasper, 2020; Horbury et al., 2020; Drake et al., 2021). Although the radial evolution of the properties of SBs should help shed light on the nature of the processes, as of today attempts to establish such a radial scaling have remained inconclusive, e.g. (Mozer et al., 2021). Recently, Patches of SBs were found to have spatial scales that are consistent with granulation and supergranulation scales (Fargette et al., 2021). Bale et al. (2021) further suggest the existence of a link with between the magnetic network and patches of SBs, which would result from PSP crossing the magnetic network field lines after these undergo expansion.

SB boundaries generally appear as sharp discontinuities. The interest in such discontinuities in the solar wind goes back to the beginning of the space age (Burlaga, 1968; Burlaga and Ness, 1969). Discontinuities are indeed accountable for a significant fraction of the wave power spectral density (Borovsky, 2010). In addition, their type determines how efficiently particle and energy exchanges are between plasma populations on both sides of the discontinuity.

Regarding SBs observed by PSP, Phan et al. (2020) noticed the absence of reconnection at SB boundaries. From this they concluded that these discontinuities should be of a rotational type. On the contrary, Farrell (2020) revealed the presence of magnetic dips at some SB boundaries. Froment et al. (2021) in addition found that some SBs undergo reconnection right at their boundaries. This is an important result since reconnection can erode the structures and heat the background solar wind. This may also explain why SBs are much more numerous at a few tens of solar radii than at 1 AU.

Krasnoselskikh et al. (2020), in a series of case studies, pointed out the presence of strong currents at these boundaries and an enhanced radial Poynting flux. These observations suggest that some boundaries may be unstable with respect to the Kelvin-Helmholtz instability (Kasper et al., 2019; Mozer et al., 2020). Finally, most boundaries exhibit enhanced wave activity at frequencies ranging from MHD scales (as we are going to show below) to the whistler frequency range (50-150 Hz) (Agapitov et al., 2020; Jagarlamudi et al., 2021) and beyond.

In this chapter, after the detailed analysis of a representative SB we concentrate on a dataset of 70 SBs that selected during PSP's first encounter with the aim to perform a statistical analysis of the characteristics of their boundaries. In particular, we want to answer the following questions:

- What is the proportion of alfvénic versus compressional structures?
- What are the sources of the different types of structures and which of the proposed mechanisms can explain the observational results?

Table 3.1. Major plasma parameters for the alfvénic structure

Parameter	Before encounter	Inside structure	After encounter
magnetic field vector nT	[-76, -17, 22]	[-46, 27, -64]	[-74, 19, 23]
magnetic field magnitude nT	81	83	80
velocity vector km/s	[324, 27, 31]	[360, 50, -75]	[331, 56, 34]
velocity magnitude km/s	326	371	337
ion plasma density cm^{-3}	324	412	361
ion temperature eV	18	57.2	28.4
ion beta	0.36	1.47	0.6
ion inertial length c/ω_{pi} km	12.6	11.2	12.0
ion Larmor radius V_{Ti}/Ω_i km	5.2	9.5	6.4

- What are the characteristics of their boundaries and is there any connection between them and the discontinuities that are observed farther away from the Sun (by other missions)?

This chapter is based on two articles: Krasnoselskikh et al. (2020) and Larosa et al. (2021).

3.2 Observational characteristics and micro-physics

The aim of this section is to give a detailed description of the observational properties of SBs, to investigate their micro-physics and to thoroughly illustrate how we conduct the analysis, which we are going to apply in a systematic way in the next section. Let us describe a typical SB that was observed on 6 November 2018 between 23:32:48 and 23:39:05 UT, one day before PSP's first perihelion pass, when is was at 36 solar radii from the Sun. The main plasma parameters for this structure are listed in Table 3.1.

Figure 3.1 illustrates the main properties of the electromagnetic field and of the thermal particles before, during and after the SB crossing. Panel a shows that the encounter begins with strong increase of the normal component of magnetic field, which grows from a few nT to more than 50 nT. At

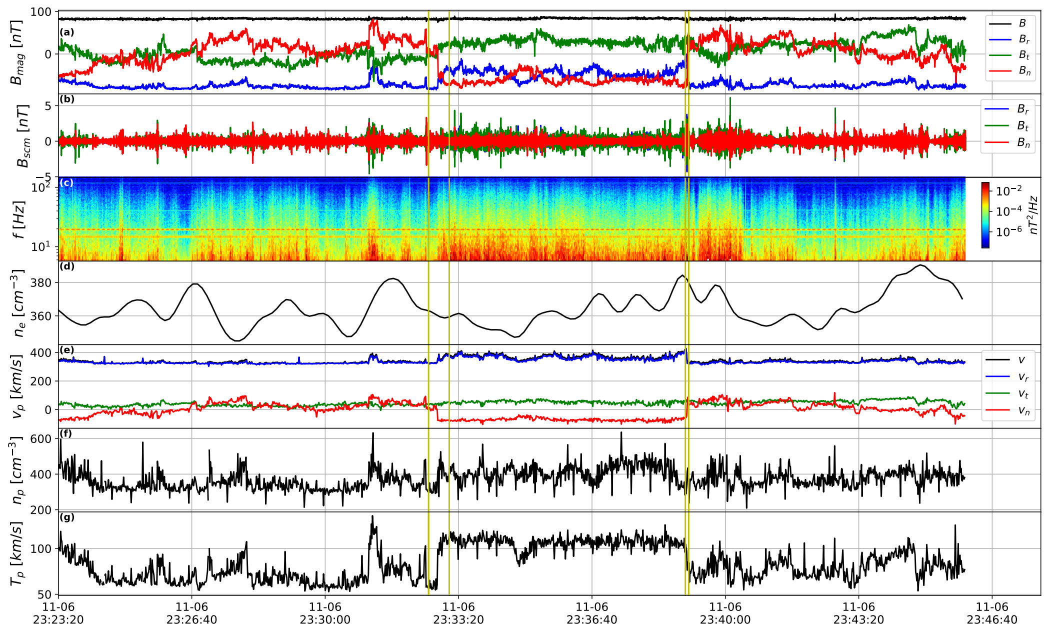

Figure 3.1 The alfvénic type magnetic structure detected on November 6, 2018: a) the magnetic field components in the RTN reference frame (the radial component is in blue, the tangential one in green and the normal one in red). The magnetic field magnitude is shown with the black curve. b) magnetic field fluctuations from the SCM instrument (the colours are the same as in panel a. c) the magnetic field fluctuations dynamics spectrum. d) the averaged electron plasma density from the QTN technique e) the plasma flow velocity from the SWEAP instrument measurements (the components colours are the same as in panel a. f) the ion (proton) density from the SWEAP instrument measurements. g) the ion (proton) thermal velocity from the SWEAP instrument measurements.

the same time the magnitude of the radial component decreases from about 80 nT to 60 nT. These variations lead to a rotation of the magnetic field of about 62° with respect to the value before the SB.

Panels b and c reveal the presence of enhanced wave activity up to frequencies of approximately 20 Hz indide the SB. The magnitude of the normal component of the velocity (panel d) increases from zero to about 80 km/s, and the radial component slightly increases too. The event lasts up to 23:39:04/05. After a 5-second transition the magnetic field goes back to a configuration that is comparable to the one it had before the SB crossing. It is worth noting that during all these variations the magnitude of the magnetic field remains almost constant, as expected for alfvénic structures.

Panels d and f reveal different values and evolutions for the measured electron and proton densities respectively. This apparent discrepancy can be explained by the different ways the two densities are estimated: the electron density is estimated by using the Quasi Thermal Noise (QTN) technique (Moncuquet et al., 2020), while the ion density is calculated as the zero'th order moment of the ion velocity distribution function measured by the SWEAP suite.

The QTN technique relies on a peak in the power spectral density of the electric field (as measured by RFS) to evaluate the plasma frequency, from which the electron density can be determined. This peak corresponds to a zero of the dielectric permittivity (Meyer-Vernet, Issautier, and Moncuquet, 2017; Moncuquet et al., 2020). When the electron gyrofrequency is much smaller than the plasma frequency (as is the case in the solar wind) the location of this peak is an excellent proxy for the local plasma frequency. A major advantage of the QTN technique is its high absolute accuracy and its independence of the satellite potential and of the instrument itself. However, because the finite frequency resolution of the RFS instrument (9.375 kHz), the frequency resolution and therefore the density resolution are coarse grained. In addition, a temporal smoothing is often required to reduce the effect of noise in the spectra, so that the practical time resolution is 10-20 s.

The determination of the ion density (and of other moments of the ion distribution function) is based on the Faraday cups from SWEAP (Kasper et al., 2016a) and is sensitive to the floating potential of the satellite to the angular view of the instrument. In contrast to the QTN technique, however, the Faraday cups are better in resolving short time scales, which is important for analysing sharp boundaries of structures. In our example, the sampling period for the ion density 0.87 s. These differences between the two instruments explain why the evolution of the density in panels d) and f) of Figure 3.1 may not fully match. In the following we shall not distinguish the ion and proton densities since the solar wind predominantly consists of protons.

Panel g displays the thermal velocity, which reveals a large and sharp increase at the leading edge of the SB and again rapidly drops at the trailing edge of the structure. The variance inside the SB is two times higher than outside, which corresponds to a temperature that is four times higher. An estimate of the proton temperature and the plasma proton beta (using density measurements by the SWEAP instrument) shows that plasma proton beta outside the structure is about 0.36 before the structure and about 0.6 after. This temperature increase is accompanied by a clear increase in the plasma proton beta, which varies from 0.3-0.6 outside of the SB to approximately 1.5 inside it. The total dynamic pressure, however, is significantly larger.

3.2.1 Boundaries

Let us now examine in more detail the boundaries of the structure shown in Figure 3.1. To do so we rely on the Minimum Variance Analysis (MVA) technique (Sonnerup and Scheible, 1998), which determines three eigenvalues and their corresponding eigenvectors from the covariance matrix of the magnetic field during a short interval that is centered on the boundary crossing. The largest, intermediate and minimum eigenvalue eigenvectors indicate, respectively, the direction along which the magnetic field exhibits the largest variance (i.e. the strongest gradients), a milder variance and the smallest variance. For 2D structures, the smallest eigenvalue is considerably smaller than the two other ones, and the corresponding eigenvector defines the direction that is perpendicular to the boundary. Using these three eigenvectors we can rotate the magnetic field from the RTN frame into a new orthogonal frame that is defined by the topology of the boundary. As we shall see later, these boundaries (which occur in the intervals that are bounded by yellow vertical yellow lines in Figure 3.1) can be identified as signatures current sheets.

Figure 3.2 shows the boundary transition for the leading edge of our structure and with the magnetic field represented in both the RTN and MVA frames. In the MVA frame, only one component exhibits a significant variation during the boundary crossing, which suggests that the boundary is essentially a 1-D structure. Panel c of Figure 3.2 shows that the velocity re-

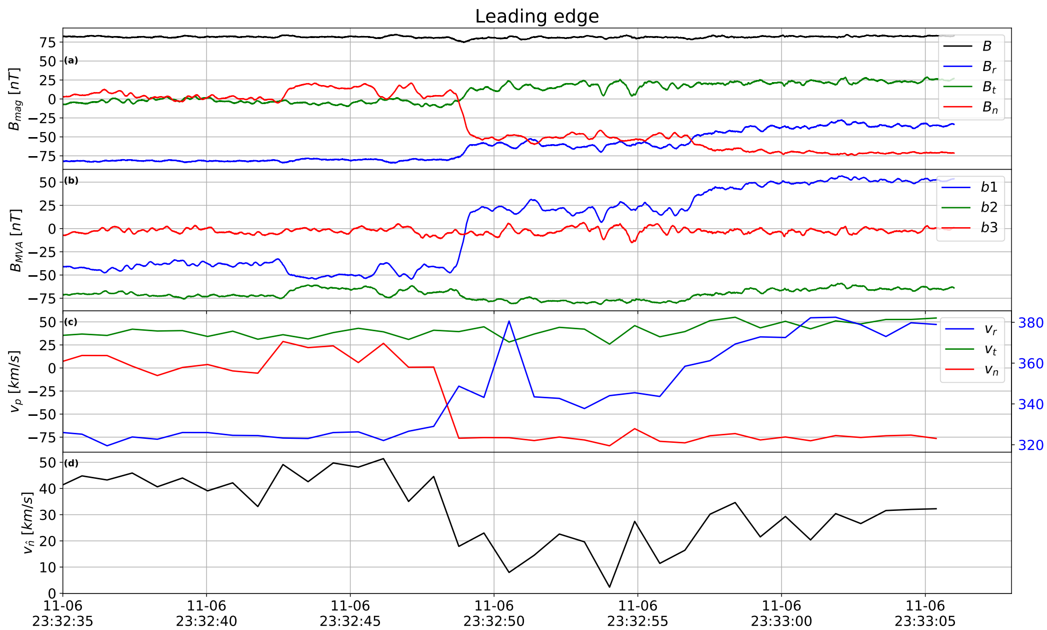

Figure 3.2 Excerpt of the leading edge of the SB shown in Figure 3.1. a) Magnetic field in the RTN frame; b) Magnetic field in the MVA frame; c) Plasma bulk velocity in the MVA frame; d) Component of the proton bulk velocity that is normal to the SB boundary. The colours of the components in the RTN frame are identical those used in Figure 3.1. In the MVA frame the order of the colours is different: blue is for the largest eigenvalue, green for the intermediate eigenvalue, and red for the smallest eigenvalue.

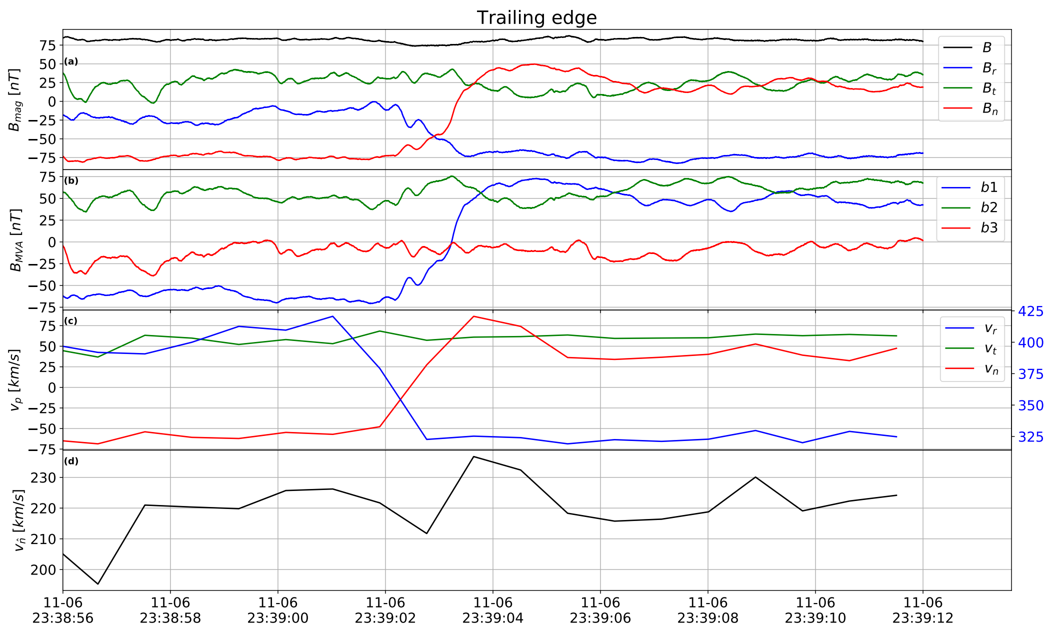

Figure 3.3 Magnetic field and plasma bulk velocity at the trailing edge of the structure shown in Figure 3.1. The format is the same as in Figure 3.2.

mains strongly correlated with the magnetic field at the boundary. Panel d represents the projection $v_{\hat{n}}$ of the proton velocity along the direction that is normal to the boundary. Its mean value in the vicinity of the boundary, multiplied by the crossing time of that boundary gives us an estimate of its size.

Figure 3.3 repeats the same analysis for the trailing edge boundary of the SB. The crossing of the trailing edge takes approximately 2 seconds, which is approximately twice that observed at the leading edge. The normal velocity is larger than that of the leading edge, so that the thickness of the boundary is considerably larger. Here too the maximum variance component of the magnetic field is highly correlated with the proton velocity.

An important feature of alfvénic fluctuations is the high linear correlation between fluctuations of the velocity and magnetic fields. In an MHD approximation this correlation can be expressed as:

$$\delta \mathbf{V} = c \mathbf{V}_A \frac{\delta \mathbf{B}}{B}$$

where c is a constant that should be close to 1. As already noted by Kasper

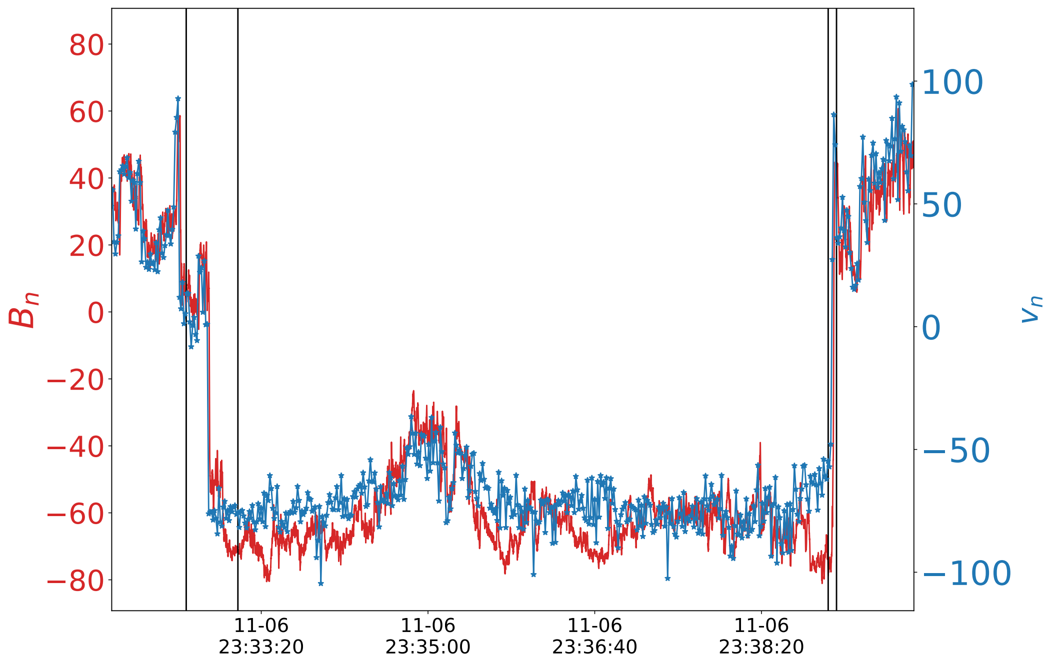

Figure 3.4 The normal component of the magnetic field (B_n) and plasma bulk velocity (v_n) in the RTN frame during the crossing of the SB shown in Figure 3.1, revealing a strong linear correlation. The leading and trailing edges of the SB are bounded by vertical lines.

et al. (2019) this correlation does not hold for most of the SBs.

In Figure 3.4 we present the normal components of the magnetic field and the velocity. Both undergo large variations during the SB crossing, whose boundaries are depicted by vertical lines. The jump in the velocity at the leading edge boundary is approximately $\delta\mathbf{V} = 100\,\mathrm{km/s}$. The jump of the magnetic field multiplied by the Alfvén velocity is $\frac{\boldsymbol{\delta}\vec{B}}{\boldsymbol{B}} \mid \boldsymbol{V}_A \mid = 93\,\mathrm{km/s}$. This gives us a value $c = 1.08$ in equation 3.2.1, which is compatible with a value of 1, given the uncertainties of the measurements. We conclude that for this structure $c \approx 1$, as would be expected for an alfvénic structure.

For the trailing edge we have $\delta\mathbf{V} = 141\,\mathrm{km/s}$ and $\frac{\boldsymbol{\delta}\vec{B}}{\boldsymbol{B}} \mid \boldsymbol{V}_A \mid = 125\,\mathrm{km/s}$. Here we obtain $c = 1.12$, which is again compatible with an alfvénic structure.

In most SBs we observe an increase in the level of wave activity at the boundaries and during the structure, see panels b and c of Figure 3.1). Figure 3.5 illustrates the fluctuation of the magnetic field in the 1 Hz to 4 Hz

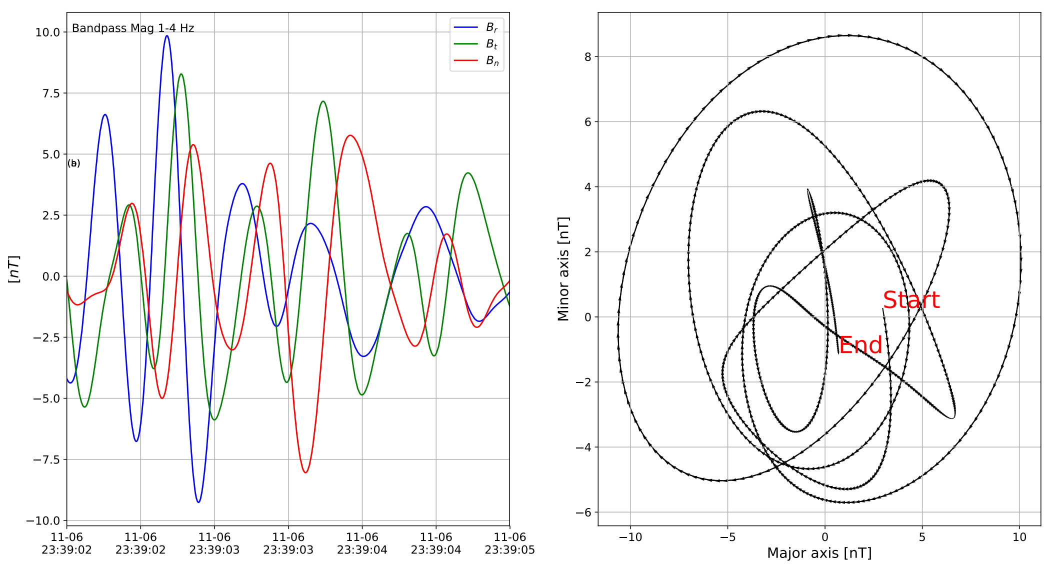

Figure 3.5 a) Waveforms of magnetic field fluctuations in the RTN frame, filtered in the 1-4 Hz frequency band during the 3 second time interval that is centered on the trailing edge of the structure shown in Figure 3.1. b) Hodograph of the magnetic field (in the plane transverse to the wave normal) showing close to circular polarisation of the observed wave.

frequency range, which captures a major fraction of the spectral power. By MVA analysis we estimate the direction of the wave-vector (associated with the direction is smallest variance) whose angle with respect to the normal of the boundary is approximately 60°. This provides a strong indication that the fluctuations correspond to a surface wave (Hollweg, 1982). The presence of this type of waves can increase the particle transfer across the boundary because the electric field is perpendicular it. In section 3.3.1 we are going to see that this is not just a sporadic event but also applies to other SB events.

Finally, we show in Figure 3.5 the hodogram of these fluctuations, which is the magnetic field projected on the plane that is perpendicular to the wave-number. The circular orbits of the hodogram suggest that these fluctuations exhibit a circular polarisation. However, one should remain careful in the interpretation of these properties since we are analysing a transient event in a narrow frequency band.

3.2.2 Local geometry hypothesis

The properties of the SB that have been discussed so far allow for a natural interpretation in terms of a crossing of magnetic flux tube, as sketched in Figure 3.6. The transverse diameter of the SB we consider here can be computed, as a first order approximation, by considering the average normal to the boundary velocity multiplied by the crossing time

$$L \simeq \frac{(V_{lead} + V_{trail})}{2}\delta t \ , \tag{3.1}$$

where V_{lead} is in the range of 10 km/s to 40 km/s, V_{trail} in the range of 200 km/s to 220 km/s and the crossing time is typically $\delta t = 7$ minutes (see Figures 3.1, 3.2 and 3.3). From this we obtain a transverse size of approximately $L = 5 \times 10^4$ km.

This size is orders of magnitude larger than typical plasma kinetic scales. Indeed, the ion Larmor radius for this event is typically 5 km to 10 km and the ion inertial length is 11 km to 12 km (see Table 3.1). From this we conclude that the macroscopic plasma flow may be treated in the MHD approximation and in terms of "frozen-in motion" with the plasma moving along the magnetic field lines. This result, combined with the hypothesis that we are crossing flux tubes implies that the velocity orthogonal to the magnetic field can be attributed to the motion of the tube and not to the plasma, which is flowing along the magnetic field. The velocity may then

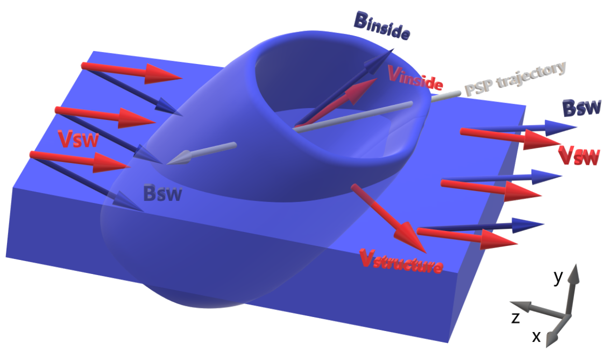

Figure 3.6 Sketch of the magnetic structure shown in Figure 3.1. The solar wind plasma bulk velocity is shown by red vectors $\mathbf{V}_{SW}$ (for the background solar wind) and $\mathbf{V}_{inside}$ (inside the structure); the magnetic field is shown by blue vectors $\mathbf{B}_{SW}$ and $\mathbf{B}_{inside}$, respectively. The solar wind bulk flow velocity ahead and behind of the encounter is about the same while the magnetic field vectors have slightly different directions indicating that currents are flowing at the boundary of the structure. The velocity of the plasma flow inside the structure has two components: the flow along the field lines parallel to the tube axes $\mathbf{V}_{inside}$ (along the magnetic field in the structure), and as the component related to the structure motion $\mathbf{V}_{structure}$. Thus the total bulk flow velocity of the plasma inside the structure is $\mathbf{V}_{flow} = \mathbf{V}_{inside} + \mathbf{V}_{structure}$. The gray line illustrates the trajectory of the PSP across the structure.

be separated into two parts: the velocity of the plasma along the field lines $\mathbf{V}_{par}$ and the velocity of the magnetic tube itself perpendicularly to its axes (which is parallel to the magnetic field inside the structures) as $\mathbf{V}_{\perp}$. We estimate these vectors are in the RTN frame.

Before the encounter with the leading edge the plasma flow moves along the magnetic field lines with a velocity of 297 km/s. The magnetic field lines of the flux tube have a relative velocity with respect to the spacecraft (in the orthogonal direction) equal to

$$\mathbf{V}_{1\perp} = [46, -35, -111] \text{ km/s}.$$

We cannot estimate the different components of the velocity of the flux tube with single point measurements. Let us therefore attribute it to plasma flow motion. Figure 3.6 suggests that the magnetic field lines of the flux tube are directed mostly radially from the Sun and move preferentially in the direction from North to South (positive to negative in the N direction) with a small deviation in the tangential direction.

After crossing the leading edge of the structure PSP observes a drastic change of the direction of the magnetic field; the average velocity vector also changes. The velocity of the plasma flow along the field lines inside the structure is approximately 129 km/s, and the velocity of the tube in the orthogonal direction is

$$\mathbf{V}_{2\perp} = [287, 91, -172] \text{ km/s},$$

whose magnitude is $V_{2\perp} = 347$ km/s. Kasper et al. (2019) called such structures "jets", because the total measured velocity with respect to external observer (the PSP satellite) inside the structure is larger than the total velocity of the flow and field lines outside of the structure.

After crossing the trailing boundary the direction of the flux tube axis changes drastically again and returns to its initial orientation. The flow velocity parallel to the local magnetic field becomes $V_{par} = 284$ km/s, and perpendicular velocity of the field lines is

$$\mathbf{V}_{\perp} = [209, 211, -17] \text{ km/s},$$

3.2.3 Currents at switchback boundaries

Interestingly, our SB shows evidence for currents flowing at its boundaries. Since we are considering MHD scales, we have

$$\vec{j} = \vec{\nabla} \wedge \vec{B}/\mu_0 \tag{3.2}$$

In the picture of the flux tube the direction of minimum variance corresponds to the normal to the surface of the flux tube, and determine the direction along which spatial variations are smallest. The corresponding component of the magnetic field is $b3$ in Figure 3.2 and in Figure 3.3). Conversely, the direction of maximal variance is the one along which physical quantities undergo large spatial variations. The corresponding component is $b1$.

The cross product between $b1$ and $b3$ defines the direction of intermediate variance, which also should give us the direction of the current. Indeed, Ampère's law states that the current flows perpendicularly to the direction of the largest spatial variation in $\mathbf{B}$ but also perpendicularly to the normal of the surface. That is, the eigenvector of intermediate variance should give an indication of the direction of the current flow (Artemyev et al., 2018). The magnitude of the current density should then be given by the ratio of the magnitude of the maximum jump of the magnetic field divided by μ_0 and by the thickness of the boundary

$$j \approx \frac{\delta B}{\mu_0 \delta L}$$

Let us now estimate this current density.

The leading edge of the SB (which might also be called ramp by analogy with shocks) was crossed on 6 November from between 23:32:48.4 and 23:32:49.6 UT which gives us a duration of the crossing of approximately 1.2 s, see panels a and b of Figure 3.4. The jump of the magnetic field during the crossing of the leading edge was approximately 75 nT although one could argue that the crossing actually occurred in steps, with secondary jumps in between. For the sake of simplicity let us therefore consider the total duration of the crossing as the time required to evolve from the stationary state before it to the stationary state inside the SB, which is 1.8 seconds. The average normal velocity during this period was approximately 25 km/s (panel d of Figure 3.4), which gives us a characteristic spatial scale of the layer of approximately $\delta L = 45$ km.

To evaluate the average magnetic field before crossing the leading edge of the SB we consider the interval from 23:29:10 to 23:30:49 when the variations of all three components of the field are relatively small (less than 10 %). We subsequently apply a low-pass filter with a cutoff filter at 1 Hz to exclude spurious wave activity and in particular ion cyclotron waves that are often observed (Bowen et al., 2020). We evaluate the average magnetic field during that interval and do the same from 23:33:51 to 23:38:12 to obtain the average field after crossing the leading edge. The two averages and their difference are respectively

$$\begin{aligned}\langle \mathbf{B} \rangle_{before} &= [-76, -17, 22.5]\ \mathrm{nT} \\ \langle \mathbf{B} \rangle_{inside} &= [-46, 27, -64]\ \mathrm{nT} \\ \delta \mathbf{B} &= [30, 44, -86]\ \mathrm{nT}\end{aligned}$$

with a magnitude of $|\delta \mathbf{B}| = 101.6\,\mathrm{nT}$.

It is worth noting that the angle between the normal to the boundary and the average magnetic field before the crossing is 82°. The normal component of the magnetic field is found to be $B_n = (-2.5 \pm 3.2)\,\mathrm{nT}$, which is weak enough to justify the notion of quasiperpendicular boundary layer, or tangential discontinuity (Neugebauer et al., 1984; Horbury et al., 2001). Finally, the evaluation of the current density from equation 3.2.3 gives us approximately $j = 1800\,\mathrm{nA/m^2}$.

Interestingly, the presence of such an important current suggests that SBs correspond to the crossing by PSP of localised kinked magnetic flux tubes Krasnoselskikh et al. (2020). The current flows along the narrow surface of the flux tube, whose thickness is of the order of 4-5 ion Larmor radii. The current makes an angle of 23° with the direction of the magnetic field outside the tube, and an angle of 30° with the axes of the magnetic tube. Thus the current density along the axis of the flux tube, and perpendicular to it, which we call respectively aligned and azimuthal components, are

$$\begin{aligned}j_{align} &= 1530\,\mathrm{nA/m^2} \\ j_{az} &= 950\,\mathrm{nA/m^2}\end{aligned}$$

Our angles have large uncertainties of typically ten degrees. However, we are merely interested in the proof of concept.

The difference between the magnetic fields on both sides of the SB is considerably smaller than the difference between the fields inside and outside the SB. Therefore, as a first order approximation we can assume the current closure to occur on both sides of the flux tube. Interestingly, the current density j_{align} that is aligned with the flux tube exceeds the azimuthal component j_{az}, which suggests that the current flows obliquely with respect to the axis of the flux tube. The reason for this obliquity is easy to understand : the current should provide a magnetic field that equals the difference between the fields on both sides of the boundary of the SB. If we consider that the magnetic field of the SB to be produced by a current loop then its current should flow in the plane that is perpendicular to the difference between the two magnetic field vectors.

Let us now consider the trailing edge of the SB. The crossing time is also approximately two seconds, from 23:39:02 to 23:39:04. However, the normal component of the velocity is now approximately ten times larger than for leading edge, which results in a larger thickness of approximately $\delta L = 440\,\text{km}$. Again, the width of that layer is sufficiently larger than any characteristic scale of the plasma, allowing us to stay in the MHD approximation. This time, the difference between the average magnetic field on both sides of the boundary is

$$\delta\mathbf{B} = [28, 9, 87]\ \text{nT}$$

with a magnitude of $|\delta\mathbf{B}| = 91\,\text{nT}$ that gives a current density of approximately $j = 165\,\text{nA/m}^2$.

The current density we observe at the trailing edge is an order of magnitude smaller than the one at the leading edge because of the larger thickness. Its orientation is almost opposite that of the current at the leading edge. The angle with respect to the axis of the tube axes is now approximately 33° so that the aligned and azimuthal components of the current density become

$$\begin{aligned} j_{align} &= 139\,\text{nA/m}^2 \\ j_{az} &= 89\,\text{nA/m}^2 \end{aligned}$$

A schematic illustration of this current element is shown in Figure 3.7.

To sustain such currents an electric field is needed. Braginskii (1965), however, have shown that strong gradients in ion temperature and in the ion pressure may produce the same effect as such an electric field. Figure 3.3 confirms that such gradients are indeed present. For the narrow current sheet at the leading edge the current may be associated with the difference of ion and electron dynamics due to the relatively small thickness of the layer in comparison with the ion Larmor radius, which is only a few times larger than it. This is not true anymore for the thicker layer at the trailing edge for which anomalous collisions due to wave activity may be a candidate. Indeed, as shown Figure 3.5 there is intensive wave activity going on at both layers, with surface waves whose k-vector makes an angle of approximately 60° with respect to the surface normal. These waves may affect the motion of electrons, as the field aligned currents are carried preferentially by the

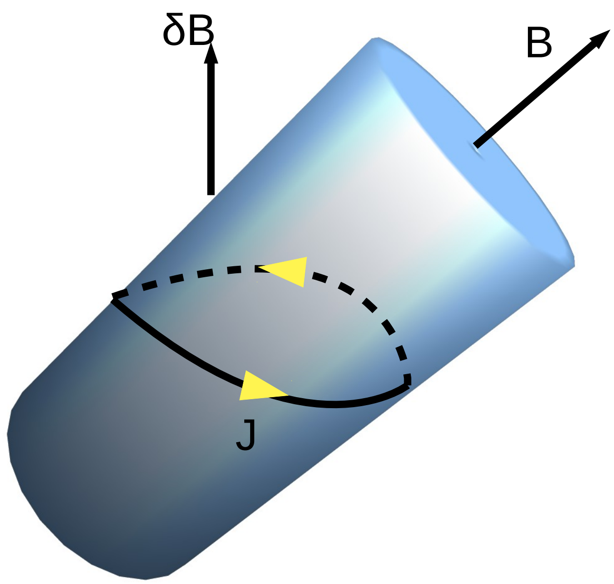

Figure 3.7 The geometry of the current system on the surface of the flux tube. Here $\mathbf{B}$ is the magnetic field vector directed along the axis of the flux tube, and $\delta\mathbf{B} = \mathbf{B}_{inside}$–$\mathbf{B}_{outside}$ is the difference between the magnetic fields inside and outside the tube. The elementary current loop is located in a plane that is perpendicular to $\delta\mathbf{B}$.

electrons. They may also lead to an important energy and impulse exchange between ions having different energies, which results in azimuthal deviations of ion trajectories and may lead to ion currents flowing orthogonally to the magnetic field. Since the characteristic scale of the waves is smaller then the thickness of the boundary layer, this may produce a rippling on the boundary surface. Such wave activity may also enhance diffusion through the boundary, which may then contribute to its widening.

3.3 Statistical properties

In section 3.2 we highlighted the properties of a single SB and our interpretation of its geometry. We found this structure to be alfvénic. However, not all SBs possess this property. Even though all of them show a high correlation (by visual inspection) between magnetic and velocity variations, there are also exceptions, as we are going to show next.

To carry out a more systematic analysis of the properties of SBs we identified a subset of 70 SBs during PSP's first solar encounter. All of them stand out by having sharp boundaries and a deflection of the magnetic field of more than 30°. These events occurred between 3 November 2018 and 8 November 2018 and represent a small fraction only of the numerous switchbacks that are observed but often show more complex boundaries or have smaller deflections. This same data set has served for the analysis by Larosa et al. (2021).

In Figure 3.8 we summarize their main statistical properties of these SBs with with respect to the surrounding plasma. The first plot represents the distribution of average magnetic field magnitude inside the SB relative to the average magnetic field magnitude outside of it. Although most structures are alfvénic, with a ratio that is close to one, there is also a smaller population of more compressible structures. If we consider structures with ratios between 0.95 and 1.05 to be alfvénic, then 73% of the SBs are alfvénic and 27% are compressible. The ratios are chosen considering that for a 100 nT magnetic field magnitude, a change greater than 5% cannot be attributed to wave activity whose magnitude is observed of be of the order of 5 nT or less in the data.

The second histogram in Figure 3.8 likewise expresses the ratio between velocities inside/outside and reveals a net and systematic increase that is on the order of 100 km/s; this value is comparable to the Alfvén velocity. The

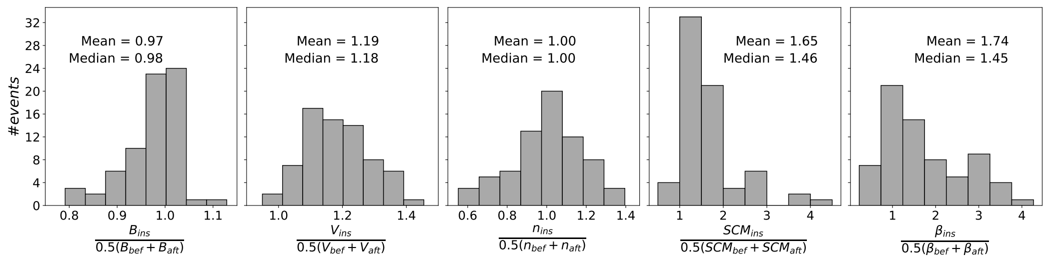

Figure 3.8 Main statistical properties of SBs, showing their average value inside of the SB relative to that observed outside for different quantities. From left to right: magnetic field magnitude, proton velocity, proton density, amplitude of the magnetic field fluctuations as measured by the SCM, and radial plasma β.

proton density (third histogram) and the electron density (not shown) do not show any preferential variation. The amplitude of broadband magnetic fluctuations above 3 Hz as registered by the SCM search-coil magnetometer (fourth histogram) are in most cases higher inside the SB. The largest increases occur for those few isolated SBs that are embedded in exceptionally quiet intervals of the solar wind.

The fifth histogram displays the plasma radial β, in which we use the radial temperature to compute β. The histogram agains shows values that are systematically higher inside than outside. When plotted against the deflection angle of the magnetic field across the boundaries, this ratio peaks at around 90°. This dependence suggests that higher values of β may be caused by a temperature anisotropy rather than by higher temperatures inside the SBs. If we compute the same β ratio by artificially keeping a constant temperature across the structures, then the enhancement is still apparent though weaker, with a median value of the ratio that decreases from 1.45 to 1.26.

In an effort to classify the SBs, let us plot their ratio of the magnetic field against that of the proton density, see Figure 3.9. In this plot, we consider as alfvénic structures those who lie between the two vertical dashed lines. For 10 structures the variations in the density and in the magnetic field are anticorrelated and for 9 they are correlated. This correlation between density and magnetic field variations can be used for wave mode identification. Indeed, in isotropic and homogeneous plasmas we can associate such correlations with fast magnetosonic waves when they are positive and with slow modes when they negative (Stix, 1992). This useful property was used by

Chaston et al. (2020) in their study of wave decomposition into eigenmodes obtained in the MHD approximation; their study is based on observations made by PSP during its first encounter for frequencies ranging from 0.0002 to 0.2 Hz. The authors find the prevalent wave mode to be shear Alfvén waves, with approximately 20-30 % of the energy carried by slow mode waves. It is worth noting that they excluded SB boundaries from their analysis and thus did not identify which wave mode should be attributed to the SBs themselves. Note that this correspondence between correlations and the type of mode is valid for linear theory, and may not fully hold for large-amplitude structures such as SBs. Let us nevertheless proceed with the analogy.

How are the characteristic sizes of the SBs distributed ? We found before that their transverse size can be approximated as (equation 3.1)

$$L \simeq V_n \delta t \ , \tag{3.3}$$

where V_n is the projection of the proton velocity along the normal to the boundary and δt is the crossing time. We define the size of the full structure as the sum of the sizes of the boundaries together with the size of the interior part. To estimate the latter, we approximate V_n as the average of the normal velocities at the leading and trailing edges. The results are shown in Figure 3.10.

The distribution of the sizes reveals a considerable scatter by several orders of magnitude. These values are consistent with those found in studies (Horbury et al., 2020; Laker et al., 2021) that used different techniques to evaluate them. The size of the largest structure in our data set is approximately 0.65 $R_\odot$. Given the position of the spacecraft (from 35.8 to 40 $R_\odot$) and an expansion factor that varies radially as R, these sizes are compatible with structures at the solar surface whose size is that of granulation (1×10^3 km) and supergranulation (1×10^4 km) cells. Recently, this correspondence has been put on firmer ground by two studies suggesting that SBs appear in patches precisely because of granulation and supergranulation patterns (Fargette et al., 2021; Bale et al., 2021).

The sizes of the boundaries exceed the ion inertial length by one to three orders of magnitude. The structures may therefore be interpreted as MHD discontinuities. These discontinuities will be further investigated below in Section 3.3.1.

Let us now we estimate the currents that generated at both sides of each of the 70 SBs, using the same approach as in Section 3.2. The results are

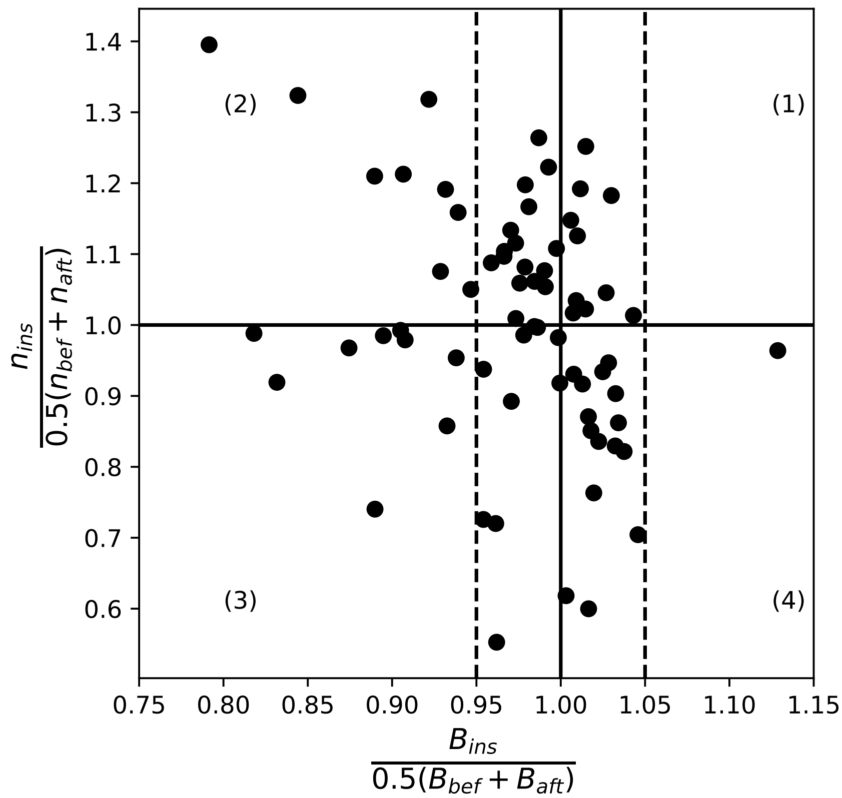

Figure 3.9 Comparison of magnetic field and density with ratios of values inside/outside SBs. The black vertical and horizontal lines split the values into four quadrants. Quadrants (1) and (3) correspond to structures in which fluctuations are positively correlated, and quadrants (2) and (4) correspond to anticorrelated fluctuations. We consider the structures that are located between the two vertical dashed lines to be alfvénic.

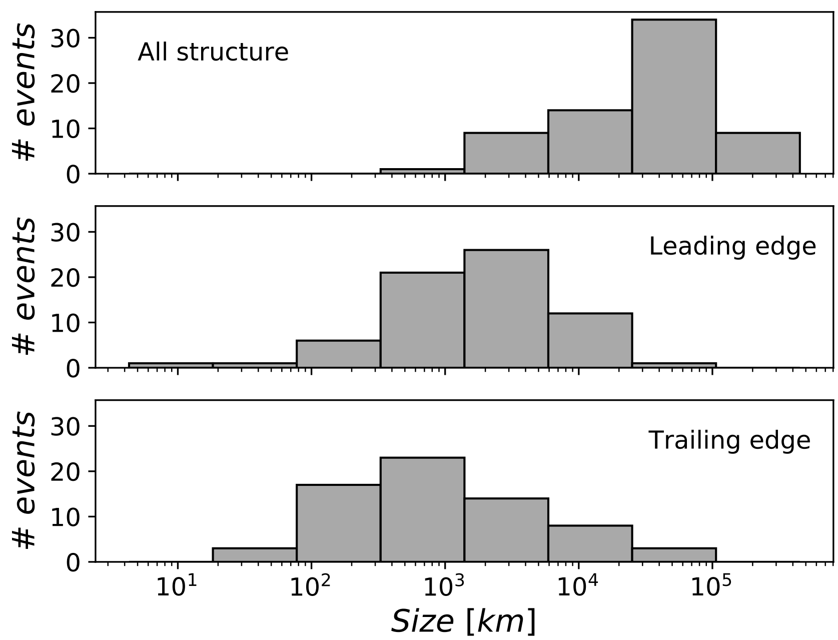

Figure 3.10 Distribution of the sizes of SB leading and trailing edges, and full structure.

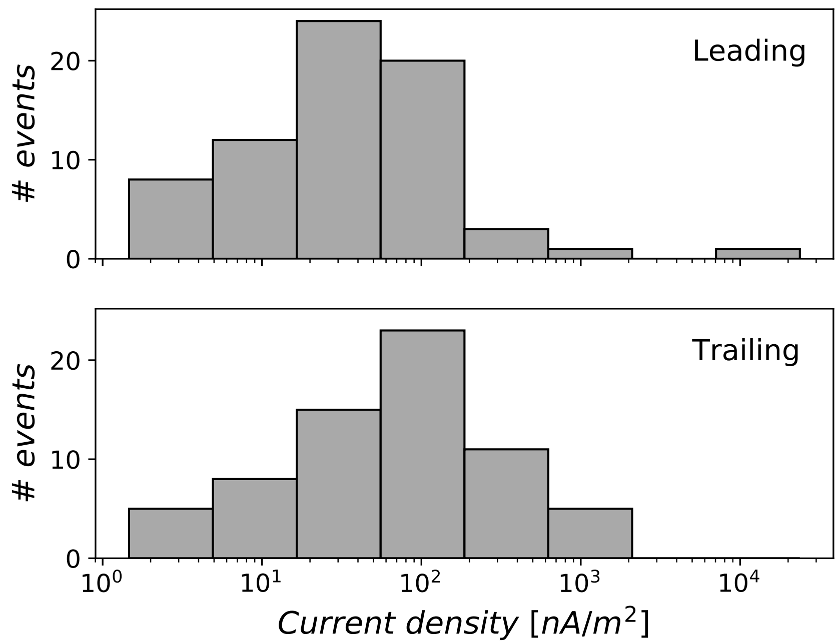

Figure 3.11 Distribution of the magnitude of the current density at SB boundaries.

shown in Figure 3.11, which again reveal a broad distribution. The current densities we find are between one and two orders of magnitude larger than those observed in solar wind discontinuities at 1 AU (Artemyev et al., 2018), for structures that are comparable in size. The main difference between the two resides in the stronger magnetic field at the location of PSP. This may suggest that the SBs boundaries we observe are not intrinsically different from other types of discontinuities in the solar wind.

3.3.1 Characterisation of the boundaries

We now seek to characterise the boundaries of the SBs to determine what insight this may give into their origin. The results of our MVA analysis of SB boundaries are summarised in Figure 3.12, in which we use the same classification scheme as in Neugebauer et al. (1984) and Horbury et al. (2001). In Figure 3.12 displays both leading and for trailing edges in order to have a better statistics.

MHD discontinuities in the solar wind are traditionally divided into rotational (RD) and tangential (TD) discontinuities. RDs are alfvénic in nature because they allow small changes only in the total magnetic field; they possess a significant component of the magnetic field along the direction normal to the boundary, which enables plasma motion through it. TDs, on the contrary, have no magnetic field component normal to the boundary, and usually do not preserve the magnetic field magnitude.

Similarly to the study by (Neugebauer et al., 1984) we consider as RD those discontinuities for which $\vec{B} \cdot \hat{n}/|B| > 0.4$ and $\delta|B|/|B| < 0.2$ and consider as TD those for which $\vec{B} \cdot \hat{n}/|B| < 0.4$ and $\delta|B|/|B| > 0.2$. Discontinuities that seem alfvénic but have a small normal component are denoted by "Either" (ED) because they correspond to values that do not allow to unambiguously distinguish between rotational and tangential discontinuities. Conversely, discontinuities that do not seem alfvénic and have a large normal component are denoted as "Neither" (ND) because they are inconsistent with characteristics of MHD discontinuities.

We find that 32% of the SB boundaries are RDs, 17% are TDs, 42% are in the "Either" area, and 9% are in the "Neither" area. These results are consistent with similar studies performed at 1 AU (see Table 2 of (Neugebauer, 2006)). The higher occurrence of RDs with respect to TDs is expected for alfvénic winds emerging from coronal holes (Söding et al., 2001).

We note that periods when $\delta|B|/|B|$ is above 40% are typically associated with sharp dips in the magnetic field that happen right at the boundary of the SBs. The field quickly recovers its magnitude once the boundary is crossed. This is the reason why such sharp changes were not taken into account in first distribution of Figure 3.8.

The structures for which $\vec{B}\cdot\hat{n}/|B|$ is close to one are SBs in which the MVA direction is close to the radial direction. For that reason, they have a large normal component. This happens for alfvénic fluctuations that propagate nearly parallel to the ambient magnetic field (Söding et al., 2001). TDs can be generated either at the stream interface by the mirror instability (Söding et al., 2001) or by the diamagnetic component of boundaries current (Krasnoselskikh et al., 2020; Farrell, 2020).

This gives us two scenarios for SBs that are embedded between two TDs. In the first one, since no significant velocity shear is observed across the boundaries, the SB has to be generated deeper down in the corona where supposedly the shear occurred. In the second case, the TDs would be just the result of the mirror instability at SB boundaries or the effect of the diamagnetic currents.

RDs could be the steepened edge of a large amplitude Alfvén waves (Tsurutani et al., 1994), a picture that is consistent with the constant magnetic field magnitude SBs with rotational discontinuities as boundaries. However, in most cases, we find the type of the discontinuity to be different at the leading and at the trailing edges. Most SBs have a TD at their leading edge and an RD at their trailing edge, or vice versa.

The MAG and SCM magnetometers often reveal enhanced levels of magnetic wave activity at SB boundaries. Most waves are broadband with frequencies typically ranging between 0.1 and 30 Hz. To analyze these waves, we bandpass filtered them and performed a polarisation analysis (Santolík, Parrot, and Lefeuvre, 2003) in the frequency band that has the largest power. This analysis was complemented by a visual inspection of the hodograms. In the following, we only consider those waves whose polarity exceeds 0.7.

Of the 140 SB boundaries, we analyzed only 32 which presented polarised waves matching our criteria. Less than one quarter of the SBs boundaries present plane polarised waves. Most of them have frequencies around 3 Hz. The angle between the normal to the boundary and their wavenumber vector (see Figure 3.13) is restricted between 0 and 90 degrees due to the intrinsic ambiguity of the polarisation analysis method. With this, we find the median value to be approximately 60 degrees; this large angle is consistent with the presence of surface waves, as suggested by Krasnoselskikh et al. (2020). Waves propagating more parallel to the boundary normal are probably gradient drift waves that are generated by the gradients of the plasma parameters across SB boundaries.

3.4 Generation mechanisms

So far five different theoretical models have been proposed for the formation and evolution of SBs. These models can be divided into two classes: those that support the in situ formation of SBs and those involving a formation deeper in the solar corona. Here we detail each of these models and subsequently discuss to what degree they are compatible with the statistical properties that have been detailed in the previous sections.

1. Squire, Chandran, and Meyrand (2020) support the in situ formation of SBs. Their model is based on the idea that the Alfvén waves, which

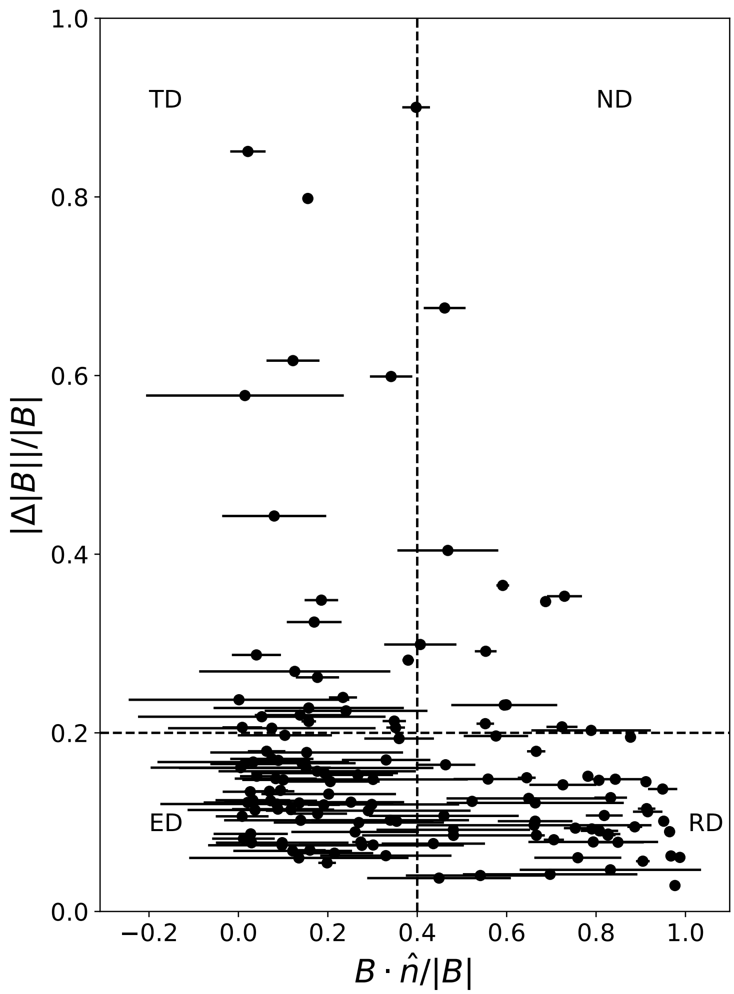

Figure 3.12 Boundary classification comparing the field threading through the discontinuity surface normalised to the field magnitude (x axis) and the highest median magnetic field magnitude between the two sides of the discontinuity (y axis). The dotted lines separate different types of discontinuities. The $\pm1\sigma$ error bars in the x direction are estimated by block bootstrapping.

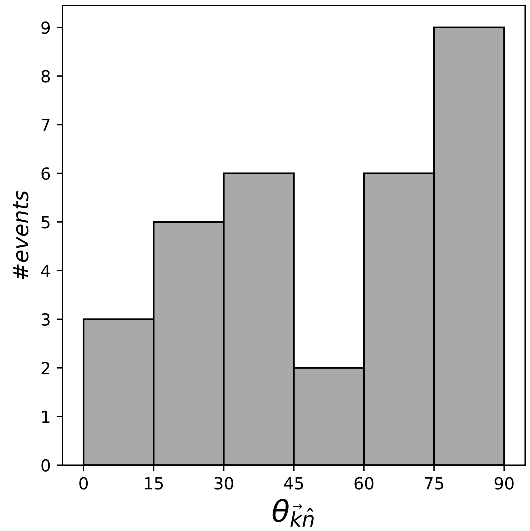

Figure 3.13 Distribution of the angles between the normal to the boundary and the k vector of the wave located at that boundary.

are naturally present in the chromosphere, can steepen due to the expansion of the solar wind during its anti-sunward propagation. The physical reason for this steepening is that the radial magnetic field decreases in magnitude faster than the fluctuations, thereby increasing the ratio $\delta b_{\perp}/B_r$. At the same time the magnetic pressure tries to keep the modulus of the magnetic field locally constant (Cohen and Kulsrud, 1974; Vasquez and Hollweg, 1998) and this gives rise to strong discontinuities.

The authors solved the MHD equations numerically for an expanding parcel of solar wind (Grappin, Velli, and Mangeney, 1993) and were able to reproduce the deflection of the magnetic field and the velocity. However, they achieved a lower rate of occurrence than observed, presumably because of limitations of their numerical simulations (Bale et al., 2019). Their result also suggests that the strongest deflection are bounded by tangential discontinuities, which is in agreement with some of the structures in our dataset. Both this model and a theoretical one based on the same idea (Mallet et al., 2021) are able to reproduce a small fraction of the SBs with slow and fast mode like properties in agreement with Figure 3.9. The radial evolution of the SBs simulated by Tenerani et al. (2021) could be consistent with this model. However, the recent observations by Fargette et al. (2021) of patches of SBs with the same angular extent of (super-)granules) supports a solar origin or at least a strong dependence on solar conditions, which these models do not properly reproduce.

2. The model proposed by Schwadron and McComas (2021) explains the formation of SBs in terms of sub-Parker and super-Parker spirals. The model is based on the possibility for parcels of solar wind with different speeds to interact in the upper corona due to the motion at the surface of the Sun of the footpoint of the magnetic field lines. When this motion causes the fast wind to be followed by a slow wind a rarefaction region and a less bent (respect to the Parker spiral) magnetic field are formed. On the contrary, when slow wind is followed by a fast one, the latter is capable of overtaking the first, which leads to a compression region and causes the magnetic field lines to be more bent until SBs are eventually formed.

   This model needs the presence of jets to explain the increased velocity inside SBs (Bale et al., 2019). In a way it can be seen as a mix of the two classes of models (reconnection/in situ) since it requires the presence of jets and foot-point motion (elements found deep down in the corona) with the in situ interaction of streams that have different speeds.

   The strength of this model is its ability to explain the one-sided tangential flow observed in SBs (Kasper et al., 2019) through the co-rotating motion of the magnetic and velocity field below the Alfvén critical surface (Schwadron and McComas, 2021). A weak point of this model could be the fact that it considers the formation of SBs tied with compression regions that are reasonable for compressible SBs but not for alfvénic ones, which are much more numerous.

3. Drake et al. (2021) developed a model which assumes SBs to result from the crossing by PSP of flux ropes. These flux ropes are produced by interchange reconnection (Fisk, 2005). Each flux rope is embedded in the unidirectional magnetic field of the solar wind; as it propagates outward it has on one side a magnetic field oppositely directed respect to the SW magnetic field and on the other side a field parallel to it.

Reconnection on the side which presents a magnetic shear can be suppressed thanks to the velocity shear between the SW and the flux rope (Chen, Otto, and Lee, 1997). While this can increase the lifetime of the flux ropes it is not clear whether this remains true up to several tens of solar radii, where PSP is located.

This model is capable of reproducing the reversal of the magnetic field, the constancy of the angle between strahl electrons and magnetic field as observed by Whittlesey et al. (2020), the dips that sometimes observed at the boundaries (Krasnoselskikh et al., 2020; Farrell et al., 2020; Larosa et al., 2021) and, supposedly, the elongation of the structures from the merging and the propagation of multiples flux ropes (Laker et al., 2021).

The main limitation of this mechanism is that flux ropes do not naturally possess the property of alfvénicty. For that reason a possible relaxation towards an alfvénic state with the flow and the field aligned is invoked by the authors. It seems that dips in the magnetic field are always present at the boundary of the flux rope whereas the majority of the boundaries we observe are rotational discontinuities for which B is close to constant (Phan et al., 2020; Krasnoselskikh et al., 2020; Larosa et al., 2021).

4. According to Fisk and Kasper (2020) SBs are generated by interchange reconnection which is set into place by the global circulation of the magnetic flux on the Sun (Fisk, 2005). This model assumes that the open magnetic field lines move in latitude from the poles towards the equator in order to keep magnetic pressure balance. During their equatorward motion the open field lines encounter closed field line structures such as loops, whose opposite polarity starts a reconnection process. The word interchange comes from the fact that after the reconnection the open and closed magnetic field lines swap positions so that an effective displacement of the open magnetic field line is obtained. The new open field is left with an S-shaped shape. The possibility of this kink to propagate up to tens of solar radii was investigated by Zank et al. (2020), who proposed a linear MHD model to study their propagation. This model assumes that the SBs are fast magnetosonic-like structures (and not alfvénic structures) due to the observed compressibility in the data.

The model by Zank et al. (2020) is able to reproduce the clustering (Dudok de Wit et al., 2020) and the variability in SBs shape according to different crossing directions of PSP. An issue with this model is that it cannot account for the slow mode features such as the anti-correlation between magnetic field and proton density variations, see Figure 3.9.

5. Finally, Ruffolo et al. (2020b) see the SBs as the result of crossing roll-up structures that are generated by the nonlinear Kelvin-Helmholtz instability, or more generally by a magnetic mixing layer. They assume that below the Alfvén critical surface (which is the layer at which the transition from sub alfvénic to super alfvénic occurs), where the magnetic pressure is supposed to be dominant, adjacent flux tubes filled with plasma and with different speeds, are stable. Outside this surface, in the anti-sunward direction, the magnetic tension is not sufficient to prevent the plasma in different tubes to mix. If the velocity gradient across the flux tubes exceeds the local Alfvén velocity then the Kelvin-Helmholtz instability can be triggered, which eventually produces the roll-ups.

   The observational motivation for this model comes from the transition from striation to flocculation as pointed out by DeForest et al. (2016) by using enhanced coronograph images of the solar corona. Striation is interpreted as a magnetically dominated solar wind, while flocculation would be the result of the mixing and developing shear driven turbulence. This mechanism mainly leads to a slow-mode (pressure-balanced) contributions to the SBs. Such structures exhibit an anti-correlation between the density and magnetic field variations, which is in agreement with our observations. Conversely, alfvénic structures are unlikely to occur.

3.5 A different possibility: Firehose instability

After this summary of the five main models that have been proposed so far to explain the generation of SBs, we consider a sixth candidate that involves kinetic instabilities and has not yet been thoroughly investigated in the literature.

The excess of parallel streaming is known to produce field reversals (Tenerani and Velli, 2018); the well known instability behind this is the so-called firehose instability. There are different possibilities for growing right handed polarised waves, which are the equivalent to the modes that are excited by the firehose instability. To illustrate them we consider a mix of protons and alpha particles.

The standard proton firehose instability requires a temperature anisotropy. The condition required to develop the instability only with the core anisotropy is

$$\beta_{||} - \beta_{\perp} \geq 2 \tag{3.4}$$

This condition is rarely met at PSP locations since the perpendicular temperature is always greater than the parallel during SBs observations (Woodham et al., 2021; Bale et al., 2021). Inside SBs the parallel temperature is comparable to the perpendicular one (Woodham et al., 2021), but condition 3.4 still is not met.

The presence of proton or alpha particle beams represents another form of excess of parallel streaming that can trigger the growth of similar instabilities. A firehose-like mode could also grow by the cyclotron resonant interaction of a parallel propagating wave of the fast magnetosonic-whistler branch with alpha particles in the presence of an alpha-proton drift that is equal to or greater than 1.7 Alfvén speeds (Verscharen and Chandran, 2013). However, the observations by Woolley et al. (2021) show that the maximum value of the drift does not exceed 1.5 Alfvén speeds.

The firehose instability can also be triggered by the anisotropy in the alpha particle distribution. This possibility seems to be the most likely one for PSP observations. Such conditions have been simulated by Matteini et al. (2015) and Perrone et al. (2013). Let us compare them with the observations of alpha particles by Woolley et al. (2021) and Bale et al. (2021):

1. The presence of an alpha to proton drift (even below the Alfvén speed) enables the development of the instability even when the parallel beta for alpha particles is $\beta_{||,\alpha} < 1$;

2. The modes that are unstable for the alpha firehose instability have larger spatial scales than the ones that are excited by the proton firehose instability;

3. The alpha firehose instability implies a cooling in the parallel direction and a heating in the perpendicular direction, even for isotropic protons;

4. A relative alpha abundance of 5% is enough to influence the proton dynamics.

The observations of alpha particle properties (Woolley et al., 2021) reveal that the alpha temperature anisotropy is of the order of $T_\perp/T_{||} \simeq 0.75$, with $\beta_{||,\alpha} \approx 0.03$. However, the mean alpha to proton drift is of the order of 0.85, which suggests that the instability can be triggered, see condition 1 above.

During SBs the parallel proton temperature is only slightly less than the perpendicular proton temperature (Woodham et al., 2021), as it would be the case for the marginal instability of the alpha firehose, in agreement with condition 3. The relative abundance of alpha particles is not clear yet. Some authors (Woolley et al., 2021) mention levels below 1% while others (Bale et al., 2021) mention levels as high as 5 %. Such high levels would agree with condition 4.

Regarding the spatial scales, the alpha firehose instability should produce structures whose characteristic size is at most 1000 km. This value is one to two orders of magnitude below that of the observed transverse scale of SBs, see Figure 3.10. However, both sizes can easily be reconciled by taking into account expansion effects.

3.6 Discussion

In this chapter, after the detailed analysis of a typical SB, we have presented a statistical study of the characteristics of 70 SBs with their boundaries. Their characteristic transverse sizes vary from several thousands of kilometers up to half solar radius. Our sample is based on SBs that are quite uniform, with well-defined boundaries. During each perihelion crossing, however, we observe many more switchbacks, most of which exhibit more complex shapes. Some, for example, show evidence for embedded structures. These have been deliberately ignored to avoid ambiguous results.

Using this subset of well-defined SBs, we have revealed the presence of two different types of structures: alfvénic and compressible ones. The former are more frequent than the latter. Our study also reveals that the majority of SBs present important plasma density variations from outside to inside. The density can either increase or decrease, but typically it does not remain the same as outside. We found that the density and magnetic field jumps are positively correlated for some SBs and anticorrelated for others. Most of them present density jumps while the magnetic field strength remains almost constant.

For most SBs wave activity is enhanced at their interior and at their boundaries, where surface waves are probably present. The radial β is also enhanced inside the structures. SB boundaries, which can be interpreted as MHD discontinuities, show evidence for both rotational and tangential discontinuities; the former are two times more frequent. Interestingly, the strong currents that flow at the surface of SBs corroborate the idea proposed by Krasnoselskikh et al. (2020) that these structures are localised kinked magnetic tubes which are separated from the surrounding plasma by surface currents.

In Section 3.4 we discussed various possible generation mechanisms, highlighting the strong and weak points of each, while in Section 3.5 we payed particular attention to the alpha particle firehose instability as an alternative mechanism.

The presence of a mix of alfvénic, fast, and slow mode signatures in SBs is an important condition for determining the most plausible generation mechanism. The best candidates for explaining all three types modes are clearly the evolution of Alfvén waves in the expanding solar wind and firehose instabilities.

There is a caveat, however. Our analysis does not unambiguously attribute the structures to a certain type of wave mode, since it is only based on the correlation and anticorrelation of the density perturbations and magnetic field magnitude. As shown by Hau and Sonnerup (1993), in anisotropic plasmas, fast modes always show a positive correlation, whereas slow modes can lead to both positive and negative correlations depending on parameters such as the angle between the wave-number vector and the magnetic field, the level of anisotropy, and the chosen state equation for moment closure. Their result is of particular interest for us since it shows that under anisotropic conditions, which favorable to the triggering of the firehose instability, slow modes may exhibit a positive correlation for a wider range of angles between the magnetic field and wave-number.

The proton firehose is known to produce waves that can be both alfvénic (Tenerani and Velli, 2018) and behave as a slow mode (Hellinger and Matsumoto, 2000). However, according to the results by Hau and Sonnerup (1993) the observations of fast modes could still be consistent with this instability.

However, as discussed in the previous section, the plasma condition observed by PSP are not favorable for the proton firehose, but they are for the alpha firehose.

The latter seems a promising mechanism of generation, but the possibility for this instability to produce fast and slow modes has not been yet investigated and it is an interesting topic for further studies.

3.7 Résumé en français: Switchbacks

Dans ce chapitre 3 nous nous focalisons sur les inversions brutales du champ magnétique appelées switchbacks. L'omniprésence de ces structures magnétiques dans le vent solaire alfvénique constitue l'un des résultats les plus intrigants de la mission Parker Solar Probe.

Le chapitre commence par une brève introduction et nous amène ensuite à une description détaillée d'un seul switchback que nous prenons comme cas d'étude. Nous détaillons les principales propriétés telles que l'alfvénicité et les échelles typiques impliquées, tant dans la structure complète que dans ses frontières. La structure est ensuite interprétée comme étant un tube de flux magnétique courbé, sur les frontières duquel circulent de forts courants. Les frontières sont interprétées comme des discontinuités MHD puisque leur taille est beaucoup plus grande que la longueur d'inertie des protons.

Notre investigation se poursuit par l'étude statistique d'un ensemble de 70 structures. Leur analyse statistique révèle qu'environ 27% des switchbacks de cet échantillon montrent des signes de compressibilité magnétique; ils soit corrélés, soit anticorrélés avec les variations de densité. Les courants aux frontières, quant à eux, sont plus forts que ceux observés à 1 UA. Enfin, les discontinuités de type rotationnel sont plus fréquentes que les discontinuités tangentielles.

Nous comparons ensuite ces observations avec les caractéristiques des switchbacks telles qu'elles sont prédites par les différents modèles actuellement en lice. Le modèle qui reproduit au mieux nos observations est celui dans lequel les structures sont supposées être formées pendant la phase d'expansion turbulente du vent solaire; en effet, l'amplitude des fluctuations diminue à un rythme plus lent par rapport au champ magnétique ambiant. Cette différence peut conduire à une croissance significative des fluctuations par rapport au champ ambiant qui peut conduire à un renversement du champ magnétique.

Nous proposons enfin une autre explication. Diverses instabilités de plasma dans le vent solaire sont liées à la formation d'inversions du champ magnétique. L'instabilité de type firehose entraînée par les particules alpha constitue un candidat sérieux pour expliquer la présence de switchbacks.

Chapter 4

Magnetic signature of Slow Extraordinary modes

4.1 Introduction

Type III radio bursts and Langmuir/Slow extraordinary waves (L-SE) can both be seen as byproducts of particle acceleration processes that occur in the lower solar corona (Reid and Ratcliffe, 2014). Both have been studied for several decades using either ground-based (Bastian, Benz, and Gary, 1998; Pick and Vilmer, 2008) or space-borne instruments (Kellogg et al., 1999).

The typical observational signature of a type III radio burst is the drifting frequency tone that evolves in time from high to low frequencies. A typical example is shown in Figure 4.1. As the the energetic electron beam that generates the type III radio emission is propagating away from the Sun, the emission that occurs at the plasma frequency drifts in time because of the decreasing plasma density, hence the decreasing tone.

Usually, type III bursts start around 10-100 MHz. Some, however start at several GHz. The lowest frequency is reached when the electron beam is farthest away from the Sun. For a beam at 1 AU, this frequency is the local plasma frequency, which is typically 20-50 kHz near the Earth (Reid and Ratcliffe, 2014).

The mechanism by which accelerated electrons generate electromagnetic waves was first proposed by Ginzburg and Zhelezniakov (1958). Their model is based on a two-step process wherein the accelerated electrons first give rise to electrostatic Langmuir waves through the bump-on-tail instability;

these Langmuir waves are then scattered by the ions, producing electromagnetic emissions at the fundamental frequency while the coalescence of two Langmuir waves generates emissions at the harmonic frequency. Another mechanism contributing to the mode conversion of Langmuir waves is the three-wave decay process (Melrose, 1982).

The problem of the Ginzburg model, as highlighted by Sturrock (1964), is that in an homogeneous plasma the growth of the waves and the subsequent flattening of the electron distribution function occurs over a distance of meters, while in the observations the beam can last until 1 AU and beyond.

Attempts to explain why the instability lasts for so long were made in the context of weak (Sagdeev and Galeev, 1969) and strong (Galeev et al., 1977a; Galeev et al., 1977b) turbulence theory. In the first case the wave growth is reduced thanks to the decay instability: the Langmuir wave decays into a daughter Langmuir wave and an ion sound wave. This then causes the daughter wave to be out of phase with the beam. In the second case involves the modulational instability, which also brings wave energy out of resonance. Although processes enable a more progressive beam relaxation, none of them can reproduce the long distances over which the electron beam generates type III emissions.

Two other mechanisms are capable of solving the problem of the beam relaxation distance. One, described by Mel'Nik (1995) (and references therein), consists in the production of Langmuir waves at the front of the beam and their absorption at the rear of it during the propagation. This reabsorption of the energy is made possible by the change in phase speed that is caused by the monotonically decreasing density. This mechanism was proven to be valid in numerical simulations (Mel'Nik, Lapshin, and Kontar, 1999).

The second mechanism is based on the fact that density fluctuations can shift the Langmuir waves out of resonance with the beam by changing their wave-vector. Muschietti, Goldman, and Newman (1985) showed that the density fluctuations can quench the growth of the bump-on-tail instability, while Voshchepynets and Krasnoselskikh (2015) revealed that they can prevent the formation of a plateau in the distribution, leaving the plasma in a marginally stable state as first suggested by Robinson (1992).

Density fluctuations may also enable the transfer of energy from the Langmuir waves to the tail of the distribution, i.e. they may lead to particles acceleration (Voshchepynets et al., 2015). These different cases suggest that the presence of density fluctuations or density gradients are a key ingredient and may help solve the problem of the persistence of the electron beam over large distances, which can be observed in situ.

The first observations of a bump on tail unstable distribution function were made by Lin et al. (1981). However, the Langmuir waves that are generated by this instability were observed much earlier. Langmuir waves have been routinely observed in the solar wind and in the Earth's electron foreshock since the early observations made by Gurnett and Frank (1975). Although these waves, which are part of the Langmuir-slow extraordinary (L-SE) branch, have received considerable attention (Bale et al., 1998; Malaspina and Ergun, 2008; Malaspina, Cairns, and Ergun, 2011; Kellogg et al., 2013) there remain many open questions regarding the mechanisms by which these electrostatic waves are subsequently mode converted into electromagnetic waves (Hinkel-Lipsker, Fried, and Morales, 1991; Krasnoselskikh, Voshchepynets, and Maksimovic, 2019). One of the major obstacles toward a better understanding of these waves is the absence of a direct observation of their elusive magnetic signature. The great abundance of observations of Langmuir waves in the electric field contrasts with the scarcity of observations of their magnetic signature, especially in the solar wind. The only exception that we are aware of are early observations in 1968 by the OGO 5 spacecraft (Scarf et al., 1971). The interpretation of the spectral signatures of magnetic waves near the plasma frequency, however, has remained ambiguous. As a consequence, most of the evidence for the existence of L-SE waves has come so far from the detailed analysis of the electric field at the plasma frequency.

In this context, Bale et al. (1998) showed by studying the phase relation with the interplanetary magnetic field that these waves are not purely longitudinal as expected for Langmuir waves. They suggested that they are actually z-modes. There exists some confusion in the terminology of these waves. According to Gary (1993) the slow extraordinary waves are called z-mode when the electron gyro-frequency is larger than the plasma frequency. Actually they are part of the same branch and therefore we shall refer to them as Langmuir-Slow Extraordinary (L-SE) wave modes.

Malaspina, Cairns, and Ergun (2011) found a positive correlation between the perpendicular electric field (indicative of the presence of a slow extraordinary mode) and the electron beam energy. They supposed that the key ingredient for the production of the L-SE is the reduction of the intensity of the wave-vector, which implies a stronger perpendicular electric field. To achieve this decrease, the authors invoke the presence of positive density gradients (in an otherwise decreasing electron density) and exclude the possibility of an electrostatic decay. Interestingly, in the presence of a double peak around the plasma frequency (a common feature of these waves), for the lower frequency peak the transverse component of the electric field typically has a larger amplitude than the parallel component.

Malaspina and Ergun (2008) investigated wave bursts in STEREO observations and concluded that about 75% of the events are linearly polarised. The remaining ones are two-dimensional and three-dimensional structures that can be interpreted as eigenmodes of solar wind density cavities.

In all these cited studies the major experimental evidence for the presence of a L-SE is the observation of a circular or elliptical polarization of the electric field. The simultaneous observation of the magnetic component of these waves would provide new constraints. This is precisely what we report on here, by providing the first direct experimental observation of the magnetic signature of the L-SE. In addition, we provide an effective theoretical approach to explain their rare occurrence and we support the theoretical result with numerical simulations.

4.2 Data and Methods

Our analysis mainly relies on waveforms sampled by the Time Domain Sampler (TDS) instrument onboard Parker Solar Probe (Bale et al., 2016). This instrument provides high cadence waveforms that are sampled here at 1.92 MHz and last for 17.07 ms. Five channels are sampled with a tunable configuration. Here the five channels capture two voltage differences between opposite antennas (V1-V2 and V3-V4), two monopole measurements (V3, and V5, which is on the same boom as the SCM), and finally one magnetic component measure by the MF antenna of the search-coil magnetometer. More details on the instrument can be found in Chapter 2.

Since the launch of Parker Solar Probe in August 2018, the TDS has been routinely recording bursts, with tens to several hundred events per day depending on the mode of operation. During the first two orbits around the Sun, the burst detection algorithm was more sensitive to dust impacts, so that few Langmuir wave events were recorded. For subsequent encounters the instrument mainly records Langmuir wave events.

The presence of Langmuir wave events in TDS bursts can be readily detected from a peak near the plasma frequency in the Fourier power spectral density. For the electric field, the peak amplitudes are generally orders of

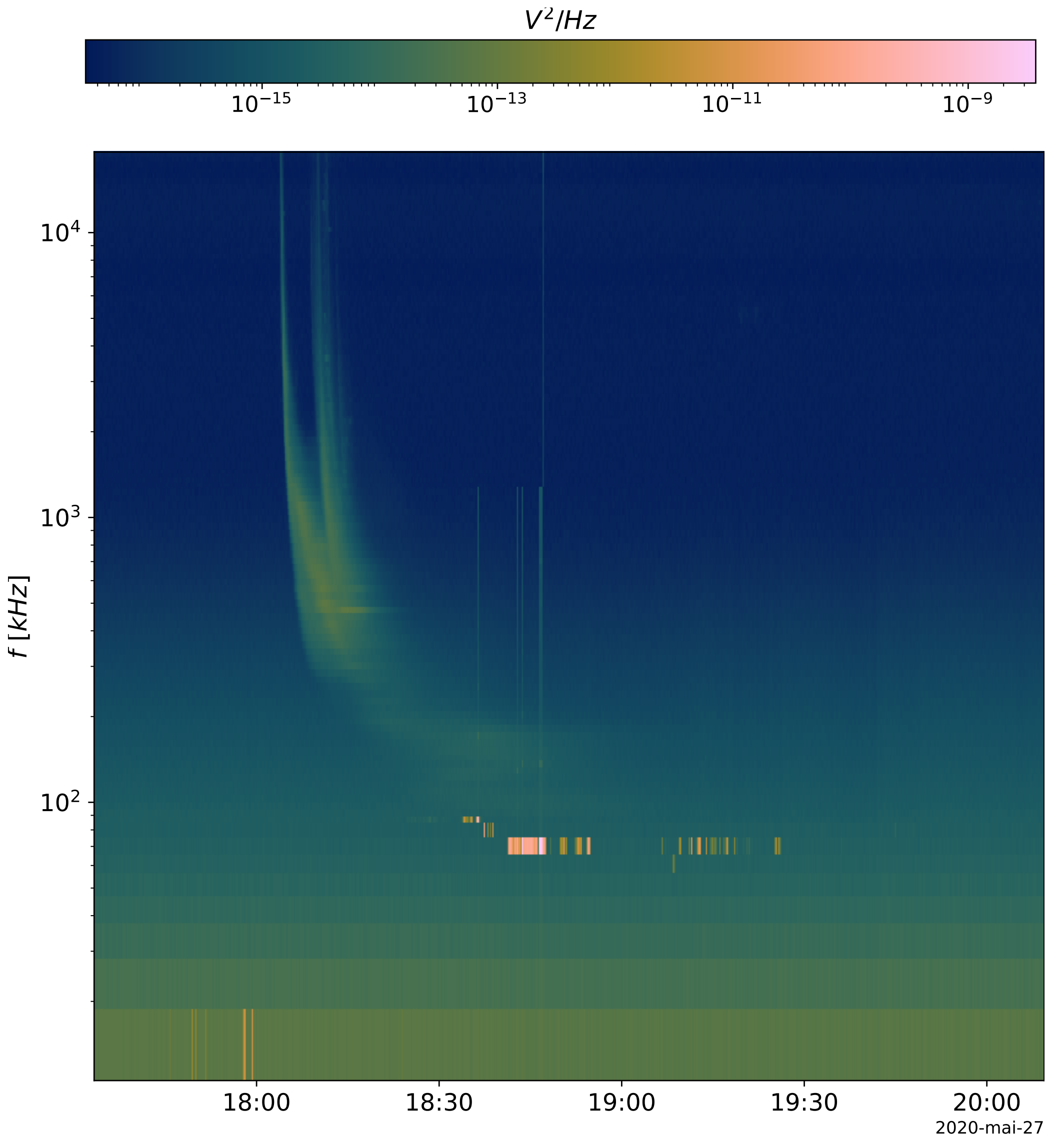

Figure 4.1 Typical example of a type III radio burst observed by PSP at a distance of about 80 solar radii, measured by the RFS instrument. The most intense features around 70 kHz are L-ES waves whose waveforms in the electric and magnetic fields are also measured by the TDS instrument.

magnitude above the noise level. For the SCM, however, the peak at the same frequency (if any) is much weaker and rarely exceeds the noise level by more than one order of magnitude (Dudok de Wit et al., 2021). In addition, all waveforms, and in particular the magnetic ones, are affected by line interferences that are due to the spacecraft.

To better reveal the presence of narrowband waves in the Fourier spectra, we normalise the power spectral density to the 30th percentile for that day. That is, for each frequency, we sort all values of the power spectral densities and keep the 30th percentile. The latter consists of a noise floor with narrow interference lines; these stick out because they are extremely stable in amplitude and in frequency. Signatures of plasma waves, however, are removed because their frequency changes from burst to burst. By normalising the power spectral densities that way we removed spurious peaks associated with interferences and the magnetic signatures of the L-SE mode are better evidenced, see Figure 4.2.

The detection of in situ Langmuir bursts by TDS is generally preceded by the observation of type III solar radio bursts by the Radio Frequency Spectrometer (RFS) (Pulupa et al., 2017). In the following, we also consider electron strahl and core properties from observations made by the Solar Wind Electrons Alphas and Protons (SWEAP) instrument suite (Halekas et al., 2020) (see CHapter 2 for more details). The count rate of high energy electrons is provided by the EPI-Lo instrument from the Integrated Science Investigation of the Sun (IS⊙IS) suite (McComas et al., 2016). Here we integrate the count rate over energies in the range 29.4 keV to 234.4 keV (to isolate the electron response) and across all the arrival directions (to maximise the chance to observe an electron and to improve the low statistics of the low count rate). The ion background does not reveal any increase for the interval of interest, therefore we are confident that we are measuring energetic electrons only.

4.3 Magnetic signature

We investigated all 30139 TDS bursts recorded between October 1, 2018 and May 1st, 2021 and first isolated all events exhibiting coherent wave packets in the electric field with a frequency located near the plasma frequency. Subsequently, we isolated all events that showed a statistically significant peak (at a level of 95%) in the magnetic field, at the same frequency. We found 26 such events only, all of which occurred on May 27 (18 events) and 28, 2020 (8 events). On those dates, the spacecraft was on its inbound leg of its 5th orbit around the Sun, at a distance of 0.34 au to 0.37 au.

Figure 4.2 shows a typical example of a L-SE wave burst with a distinctive signature in the normalised magnetic field. In this example, the peak in the power spectral density is 6 times above the noise floor whereas for the electric the spectral power exceeds the noise floor by more than 10^6. This weak amplitude of the magnetic signature is consistent with the quasi-electrostatic nature of these waves. The three columns on the left show the raw waveforms recorded in the electric field (V1-V2, and V3-V4), and in the magnetic field. Note that no coherent wave activity is apparent in the latter because the signal is dominated by interference noise coming from the spacecraft.

The three columns on the right of Figure 4.2 show the corresponding power spectral densities, estimated by Welch's method. The electric field has a double-peaked spectral signature that has often been observed before in the solar wind (Bale et al., 1996; Krasnoselskikh, Dudok de Wit, and Bale, 2011; Malaspina, Cairns, and Ergun, 2011). These peaks correspond to the incident and reflected wave. Interestingly, in all the events we observed, the spectral peak of magnetic field coincides with the largest of the spectral peaks of the electric field, which is the one that has the lowest frequency and corresponds to the incident wave. The second peak (the reflected wave) might have a magnetic signature as well, which just happens to remain hidden in the noise floor.

Interestingly, these events were preceded by a type III solar radio burst whose energetic electrons provided the necessary conditions for observing L-SE waves. Figure 4.3 provides a global picture of the plasma conditions on May 27, 2020. Panel a) displays the magnetic field. Panel b) shows the spectral amplitude of V1-V2, as measured by the RFS instrument, with two type III solar radio bursts around 18:10. The outward propagating electron beam reaches the spacecraft by 18:30, when it produces enhancements in the RFS signal and distinct Langmuir wave packets in the TDS. The frequency of the latter is reported in panel c) and tracks the drop in the electron density shown in panel d). The last panel reveals a small but significant increase in the number of energetic electrons with energies between 27 and 375 keV

The electrons that generate the L-SE mode are expected to have energies between 1-3 keV, which is much lower than what EPI-Lo measures. We obtain this estimate in two different ways. First, we assume that the time interval between the beginning of the type III radio burst and the first in

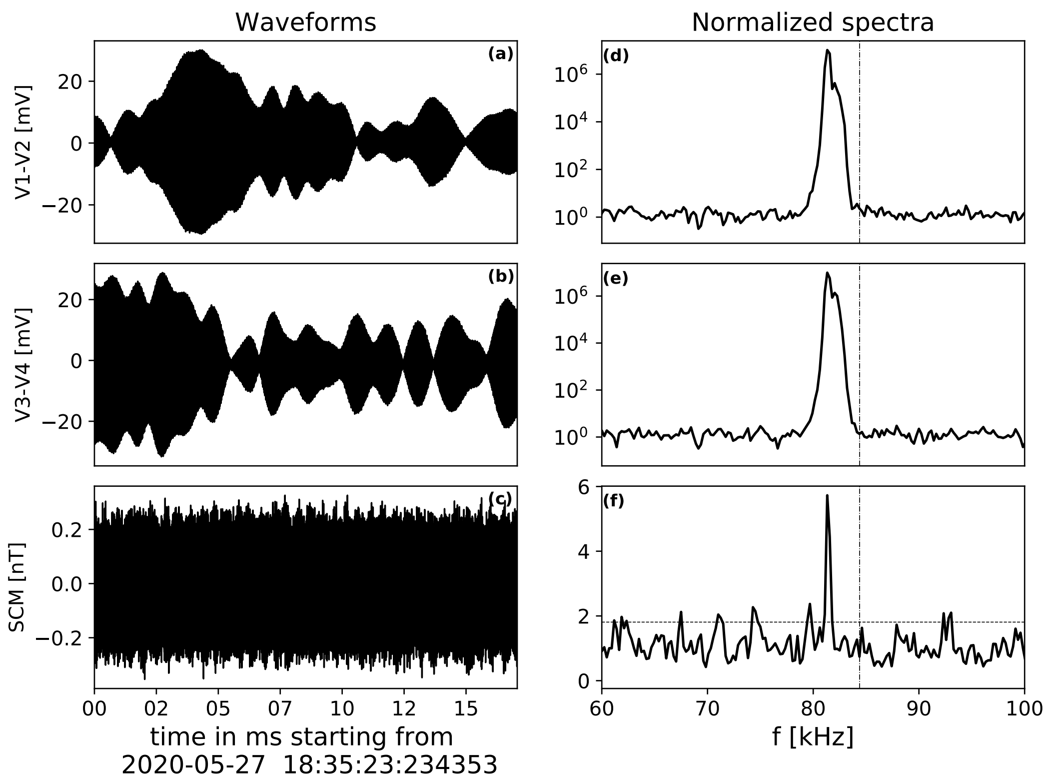

Figure 4.2 Example of a L-SE wave burst with a magnetic signature. On the left, from top to bottom: raw waveforms from the dipolar electric field V1-V2, V3-V4 and the SCM search-coil. On the right, their corresponding normalised power spectral densities. The vertical dashed line indicates the location of the plasma frequency.

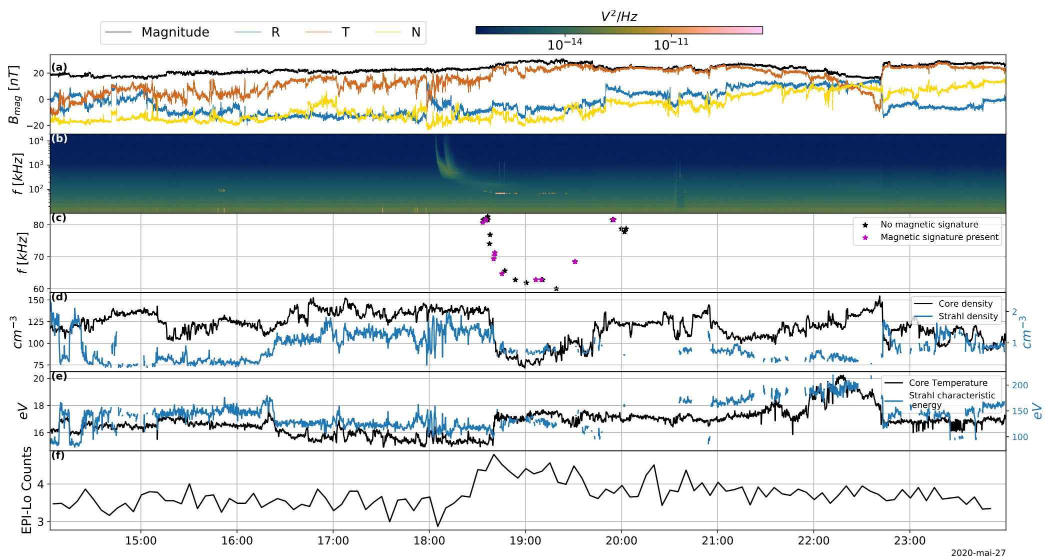

Figure 4.3 General view of the plasma conditions on May 27, 2020. From top to bottom : a) the magnetic field from MAG, b) spectrogram of the V1-V2 dipole voltage from RFS (with color-bar at the top), c) peak frequency of the L-SE bursts observed by TDS panel, d) density of the electron core (black) and strahl (blue) population, e) electron core temperature (black) and strahl characteristic energy (blue), f) energetic electron counts from EPI-Lo.

situ L-SE burst equals the time needed by electron beam to travel from 1 solar radius ($R_\odot$) to the location of the spacecraft near 80 $R_\odot$. This gives us a velocity and hence an energy of the electron beam in the 1-3 keV range.

We obtain the same estimates by considering the density profile as a function of the radial distance from the Sun, using the method by Leblanc, Dulk, and Bougeret (1998). This profile can be converted in a radial profile for the plasma frequency. Using the highest and lowest frequencies of the radio burst we can invert the formula to obtain the distance from the Sun, and from these the beam energy.

Unfortunately, there is an energy gap between SWEAP and IS⊙IS that prevents us from assessing the presence of electrons in the 1-3 keV range of interest. For that reason, the electrons that are observed by EPI-Lo probably represent the high energy tail of the enhancement that causes the L-SE bursts. These energetic electrons, however, are part of the same burst of ejected energetic electrons and therefore provide additional evidence for the latter. With this, Figure 4.3 clearly shows that the L-SE bursts were generated in an highly inhomogeneous plasma. As we shall show next, this aspect is of crucial importance for the presence of magnetic signatures.

4.4 Theoretical framework

The key to the understanding of the occurrence of magnetic signatures of the L-SE mode is the relationship between fluctuations of the magnetic field, of the electric field and the value of the refractive index N. The three are related through Faraday's law in the Fourier space

$$\vec{B} = \vec{N} \times \vec{E}. \tag{4.1}$$

In equation 4.1 $\vec{N}$ is a vector whose magnitude equals the value of the refractive index N and which is directed along the wave-vector $\vec{k}$ of the wave. This expression suggests that the ratio between electric and magnetic field perturbations is proportional to the refractive index of the wave. However, careful analysis of the polarization properties of the L-SE wave mode shows that paradoxically the dependence is roughly inverse. Indeed, from the dispersion relation of a warm magneto-active plasma, combined with Faraday's law, we find (see Appendix A for more details):

$$\delta\vec{B} \approx \frac{\delta E}{N}\begin{pmatrix} -i\frac{\Omega_c}{\omega_p}\cos\theta\sin\theta \\ 3k^2\lambda_D^2\cos\theta\sin\theta \\ i\frac{\Omega_c}{\omega_p}\sin^2\theta \end{pmatrix} \tag{4.2}$$

where θ is the angle between $\vec{B}$ and $\vec{k}$, ω_p is the electron plasma frequency, Ω_c is the electron cyclotron frequency and λ_D is the Debye length.

In Equation 4.2 we consider monochromatic fluctuations around the plasma frequency. By taking the modulus on both sides we obtain the relationship in Fourier space at fixed frequency between the fluctuation amplitudes of the magnetic and the electric field, and the refractive index. Assuming a small angle of propagation of $\theta = 10°$ (because the modes are mostly electrostatic), and $\omega \approx \omega_{pe}$, we obtain

$$\delta B^2 \approx 10^{-5}\frac{\delta E^2}{N^2}. \tag{4.3}$$

Equation 4.3 reveals that the conditions for having a strong magnetic component of the wave are the presence of strong electric fluctuations and a small value of the refractive index. Such conditions typically arise in the presence of density inhomogeneities in the plasma. Let us investigate this by studying the propagation of a wave in an inhomogeneous plasma.

4.4.1 Wave propagation in inhomogeneous media: a Hamiltonian approach

The dispersion relation for quasi-electrostatic slow extraordinary waves may be written as in in equation 4.4. Here we neglect the contribution of ions, and without loss of generality the average magnetic field is chosen to be along the z axis.

$$\omega = \omega_p\left[1 + \frac{3}{2}k_z^2\lambda_D^2 + \frac{\Omega_c^2}{2\omega_p^2}\sin^2\theta\left(1 - \frac{\omega^2}{c^2k^2}\right)\right] \tag{4.4}$$

The term $k_z^2\lambda_D^2$ is equal to v_{th}^2/v_b^2, assuming a resonant interaction between the electron beam and the wave, i.e. $v_{beam} \approx v_{phase}$. For the events we observe in the solar wind, this ratio is of the order of 10^{-2}. The last term of equation 4.4 is of the order of 10^{-4} since the ratio between the plasma and cyclotron frequencies is approximately 10^{-2}. The ratio $\frac{\omega^2}{c^2k^2} = \frac{1}{N^2}$ is much smaller than one since the modes we consider are quasi-electrostatic. From these considerations, and as a first order approximation, we can neglect the last term of equation 4.4 and evaluate the variation of the z-component of the wave-vector when the wave propagates in inhomogeneous plasma and the density varies. Assuming that $\delta\omega \approx 0$ we obtain:

$$\delta k \approx -\frac{\delta n}{n}\frac{1}{3\lambda_D^2 k^2}k_z. \tag{4.5}$$

Equation 4.5 shows that when the density fluctuations are of the same order as $k_z^2\lambda_D^2$ the variations of the k-vector are of the order of the k-vector itself, since the parallel component (z) is the main one. This implies that k_z goes through zero and therefore the wave gets reflected. The refractive index N reaches its minimum when the wave gets reflected, which then also increases the chances of observing magnetic signatures.

These considerations can be further developed by considering that in the case of stationary wave propagation the frequency is constant along the wave path. Therefore, by analogy with the energy in mechanical systems, the frequency may be considered as a Hamiltonian function. Let us therefore rewrite the equations of motion by making use of the similarity between the momentum of the particle and the k-vector, with coordinates that convey the same meaning as in classical mechanics.

We follow a single wave packet in an inhomogeneous plasma with varying electron density and magnetic field. A more detailed explanation of this kind of approach can be found in Suchy (1981). The Hamilton equations for wave propagation, under the eikonal approximation, are the following:

$$\frac{d\vec{k}}{dt} = -\frac{\partial\omega}{\partial\vec{x}} \tag{4.6a}$$

$$\frac{d\vec{x}}{dt} = \vec{V}_{gr} = \frac{\partial\omega}{\partial\vec{k}}. \tag{4.6b}$$

where $\vec{V}_{gr}$ is the group velocity.

The resulting system of equations in a two-dimensional space, where one direction is parallel to the magnetic field (z) and the other orthogonal to it (x), reads (see appendix B):

$$\frac{dx}{dt} = \xi^2 \frac{k_x}{k^4} \left[k_z^2 - \frac{v^2}{k^2} \left(k_z^2 - k_x^2 \right) \right] \tag{4.7a}$$

$$\frac{dz}{dt} = 3k_z \tag{4.7b}$$

$$\frac{dk_x}{dt} = -\frac{\partial n}{\partial x} - \xi \frac{k_x^2}{k^2} \left(1 - \frac{v^2}{k^2} \right) \frac{\partial \xi}{\partial x} \tag{4.7c}$$

$$\frac{dk_z}{dt} = -\frac{1}{2} \frac{\partial n}{\partial z} \tag{4.7d}$$

In system 4.7 all the quantities are dimensionless. Lengths, time and k-vector are respectively normalised by the Debye length, the electron plasma frequency and the inverse of the Debye length. The dimensionless density fluctuations n are normalised with respect to the background electron density. The variation of the magnetic field appears in the dimensionless variable $\xi = \frac{\Omega_c}{\omega_p}$. The parameter $v = \frac{v_{th}}{c}$ represents the ratio of the electron thermal speed to the speed of light.

4.5 Simulation

We simulate the system of equations 4.7 on a fixed grid that does not evolve in time and we study the variation of the refractive index in the presence of pre-specified density profile n and changes in the profile of ξ. We solve the equations with a 4th order Runge-Kutta scheme. The aim is to further elucidate the effect discussed through equations 4.2 and 4.5.

Figure 4.4 illustrates the evolution of a wave in the presence of a density depletion (along x and z) and a magnetic field that gradually increases along x. We initialise the simulation at $x_0 = 0$ and $z_0 = 0$, $kx_0 = 0.01$ and $kz_0 = 0.1$. The choice of the initial position is arbitrary, the choice of the wave-vector initial value is motivated by the fact that the L-SE mode is mainly parallel to the magnetic field and by the assumed beam plasma interaction which, as discussed in section 4.4.1, gives $k \approx 1/10\lambda_D$. Therefore we consider a value of 0.1 for the normalised k_z.

The density profile is shown in panel (a). We use a normalised background density of one with fluctuations up to 8 %. This is consistent with the observations of Krupar et al. (2018). The black line represents the trajectory of the wave. The ratio $\xi = \Omega_c/\omega_p$ determines the main motion direction, with a value of 10^{-2} the motion is mostly along the parallel direction z. The inset highlights the reflection of the wave. We approximate the shape of the density cavity by a Gaussian shape

$$n(x, z) = 1 + \alpha \exp((x/l)^2) + \beta \exp((z/l)^2) \tag{4.8}$$

where $l = 100$ in order to have the length scale for the variation of the density that is much longer than the wavelength - in agreement with the WKB approximation. The parameters α and β are used to tune the level of density fluctuations in the two directions. In figure 4.4 α is chosen smaller than β ($\alpha = \frac{\beta}{6}$) in order to allow the wave to propagate more along the x direction before being reflected towards the $-x$ direction. The aim is to obtain more minima of the wave-vector in panel (d), for a better illustration.

Panel (c) show the profile for the variation of the magnetic field, which is incorporated in the parameter ξ. The increase is chosen consistently with the one observed in the data of figure 4.3, the profile is $\xi = 0.01(1 + x/l)$. The factor 10^{-2} represents the giro-frequency to plasma frequency ratio. With this value different profiles of ξ do not modify significantly the wave motion.

Panel (b) illustrates the position of the wave on the grid respect to time. The periodic motion with respect to the z component and the drift in the x direction are evident. This drift is enhanced and the reflection points as can be seen from panel (b) of figure 4.4. In fact from the first equation of system 4.7 we can see that when $k_z \approx 0$ the ratio $v/k \approx v/k_x \approx 1$ and the right hand side become proportional to $1/k$ instead of $1/k^2$ as when k_z is dominant. This means that more relative power goes in the perpendicular direction at the reflection point in agreement with the observations of Malaspina, Cairns, and Ergun (2011). In agreement with this, panel (d) shows that at the reflection points k (and therefore the refractive index) is the lowest and this imply that the magnetic component is stronger as indicated by equation 4.2. The drop is of the order of 90%, which corresponds to a drop of 99% in N^2.

In panel (d) we can also observe that k_x is decreasing in time. This behaviour has a simple mechanical analogy. When moving towards x, the wave/particle sees an increasing density/potential and therefore its k_x/momentum keeps on decreasing until it is reflected in the x direction at later times.

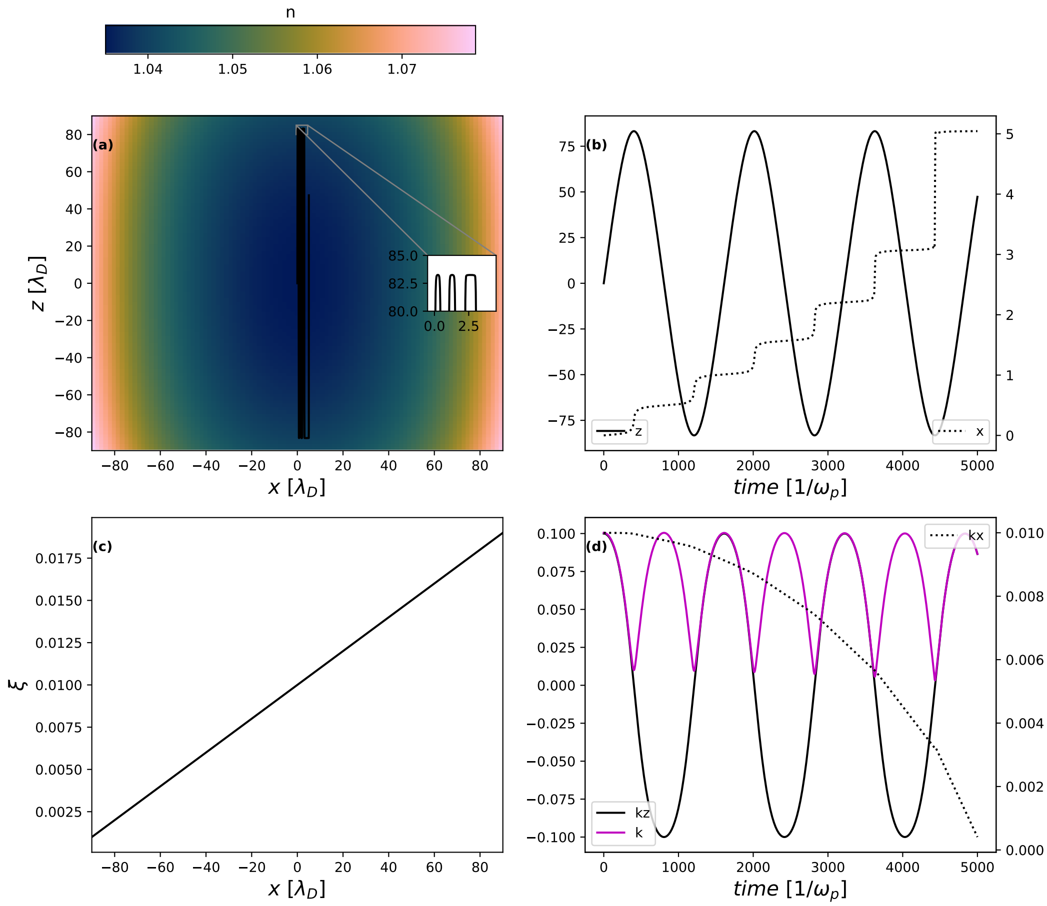

Figure 4.4 Numerical integration of system 4.7. Panel (a) density cavity in the xz plane and wave trajectory in black. Panel(b) Wave position respect to time, solid line z, dotted line x. Panel (c) ξ parameter profile. Panel (d) k-vector components (z solid line, x dotted line) and magnitude (magenta line). In panel (b) and (d) the ticks on the left correspond to the quantities with legends on the left and the ticks on the right correspond to the ones on the right.

4.6 Conclusions

In 2.5 years of observations made by Parker Solar Probe, we found only two days with clear evidence for magnetic signatures of L-SE waves. These events occurred during conditions of strong density fluctuations and took place when the spacecraft was located close to an electron beam associated with a type III solar radio burst.

To interpret these results we investigated the analytical relation between the level of magnetic and electric fluctuations, and the refractive index N of the waves. The inverse proportionality between N and the ratio $\delta B/\delta E$ reveals that the propagation in an inhomogeneous media in which N changes substantially is a key factor.

To put this on firmer ground we studied the Hamilton equation for the propagation of a single wave and by simulating this equation found that in the presence of density depletions a drop in the refractive index occurs at the reflection point of the wave.

These results raise the question as to why such magnetic signatures are not observed more frequently. First, let us stress that Parker Solar Probe and Solar Orbiter are the first missions in the solar wind whose magnetic sensor covers the frequency range of Langmuir waves. A handful of missions such as POLAR had a high-frequency magnetic sensor (Gurnett et al., 1995) but were mainly flying in the Earth's magnetospere. For these reasons, no systematic study of the magnetic signature of L-SE waves had been carried out so far in the solar wind.

An important element here is the sensitivity of the instrument chain, which has two contributions : one comes from the sensitivity or noise floor of the SCM, which is $0.01\,\mathrm{pT/Hz^{1/2}}$ in the frequency range of interest. The other is the resolution of the TDS, which is $0.05\,\mathrm{mV}$ and is equivalent to $0.1\,\mathrm{pT}$. From this we conclude that the observability of magnetic signatures is primarily constrained by the resolution of the TDS. As shown by Dudok de Wit et al. (2021), the magnitude of the magnetic signature is bounded by that of the electric fluctuations $\delta B \leq \alpha \delta E$, where α is a constant. The events that have a distinct magnetic signature correspond to the largest values of δE observed by Parker Solar Probe. This suggests that many more events may potentially have a magnetic signature, but just happen to be too weak to exceed the $100\,\mathrm{fT}$ noise floor.

Likewise, the coherent wave packets exhibit two peaks in the power spectral density of δE with a magnetic signature that always coincides with the lower-frequency peak, i.e. the incident wave. Here again we cannot conclude whether the reflected wave has a magnetic signature too because the amplitude of the latter has remained so far below the noise floor.

4.7 Résumé en français: signature magnétiques des modes extraordinaire lents

Le chapitre 4 est consacré aux premières observations révélant sans ambiguité la signature magnétique de modes de type extraordinaire lent. L'importance de ces observations tient au problème de l'émission dans un plasma, c'est-à-dire à la façon dont un signal électrostatique est converti en un signal magnétique dans un plasma. Or ceci joue un rôle fondamental dans la compréhension des émissions radio solaires.

Les mesures des signatures magnétique de ces modes d'onde ont de tout temps constitué un défi instrumental car leur faible amplitude est proche du niveau de bruit ambiant, alors que leur composante électrique dépasse généralement ce niveau de bruit de plusieurs ordres de grandeur.

Nous avons trouvé ces signatures dans les données Parker Solar Probe seulement pendant deux jours et pour quelques dizaines d'événements. Motivés par leur rareté et leur nouveauté, nous avons étudié leur apparition d'un point de vue théorique et numérique. Du point de vue observationnel, nous avons d'abord remarqué que ces événemenmts surgissent dans des conditions où le plasma est hautement inhomogène et en présence d'un faisceau d'électrons.

De nombreuses études ont montrée que la présence d'un tel faisceau d'électrons conduit à la bump on tail instability qui génère des modes électrostatiques. En partant du système linéarisé de Vlasov-Maxwell, nous avons trouvé la relation liant l'amplitude du champ magnétique de l'onde, l'amplitude du champ électrique et l'indice de réfraction du milieu. Nous trouvons ainsi que la composante magnétique est directement proportionnelle à la composante électrique et inversement proportionnelle à l'indice de réfraction. Il s'ensuit que si l'indice de réfraction baisse en raison, par exemple, de la présence d'inhomogénéités de la densité, alors les chances d'observer la composante magnétique sont plus grandes.

Pour tester ce résultat, nous avons calculé les équations de Hamilton pour suivre la propagation d'une onde de type extraordinaire lent. Nous avons résolu numériquement ces équations sur une grille 2D inhomogène et stationnaire. Le résultat de la simulation confirm la validité de notre approche théorique et révèle que la probabilité d'observer une signature magnétique augmente lorsque l'onde est réfléchie suite à la présence d'un gradient de densité.

Le chapitre se termine par des considérations sur d'autres aspects qui devraient être pris en compte, tels que l'énergie du faisceau d'électrons et la sensibilité des instruments. Ces aspects sont laissés pour des travaux futurs.

Chapter 5

Conclusions and Perspectives

Magnetic field observations are the leitmotiv of this thesis. Parker Solar Probe gave us the opportunity to investigate magnetic field structures and waves from MHD scales up to the electron plasma frequency in the inner Heliosphere, in a young and much more structured solar wind than what is routinely observed at 1 AU.

In this thesis we have focused on two different topics both related to novel measurements in the inner Heliosphere. The first one deals with sudden magnetic deflections that are called switchbacks (SBs), which are ubiquitous in slow alfvénic solar winds and have received considerable attention. One of the major questions of interest is the nature of the processes that give rise to such structures in the solar wind.

To answer this question we investigated their properties with a special focus on their boundaries by carrying out a detailed statistical analysis of a subset of 70 well defined switchbacks that were observed during Parker Solar Probe's first encounter with the Sun in November 2018.

We observed that approximately 30% of the switchbacks present compressional signatures of the magnetic field, with a significant correlation or anticorrelation between magnetic field magnitude and proton density variations with respect to the surrounding plasma. These (anti-)correlations allow us to classify them as slow and fast mode-like. Such a classification is useful for constraining the different generation mechanisms.

In Chapter 3, we review five models that have recently been proposed for explaining the origin of SBs.

The model proposed by Squire, Chandran, and Meyrand (2020) and (Mallet et al., 2021) that interpret the switchbacks as the steepening of Alfvén waves in the radial expanding solar wind offers the best match with our constraints. (Mallet et al., 2021) shows that the observation of both correlation and anticorrelation between magnetic field magnitude and proton density is dependent on the plasma beta and on the angle of propagation of the SBs with respect the mean magnetic field. When $\beta < 1$ we have fast mode-like correlation whereas with $\beta > 1$ we have slow mode-like correlation. The dependence on the angle of propagation that they found could be tested against our observations to estimate the accuracy of the model.

Another promising model is the firehose instability for alpha particles. Interestingly, the temperature anisotropy of the alpha particles was shown to decrease with radial distance (Stansby et al., 2019) from 0.3 AU onwards, in agreement with the particles lying near the firehose instability (parallel and oblique) thresholds. This radial evolution is also consistent with the decrease of the rate of SBs per kilometer as estimated from PSP and Ulysses data (Tenerani et al., 2021). However, the ability of alpha particles firehose to produce slow and fast mode-type structures has not yet been investigated in detail. This is clearly a subject of future work. The statistical analysis of the SBs has been published in (Larosa et al., 2021).

The increased level of magnetic fluctuations which we observe inside SBs is consistent with other observations of increased power of fluctuations inside switchbacks (Dudok de Wit et al., 2020; Martinović et al., 2021). However, whether SBs can be considered as being part or not of the turbulent wavefield is still an open question.

Studying separately the radial evolution of the SBs intervals versus the radial evolution of the quiescent field could give some hint with respect to this question. Of particular interest would be to study the evolution of compressibility for the two different regimes and to assess whether the compressible SBs evolve differently from the alfvénic ones and whether the compressibility evolution is different for the quiescent field respect to the two types of SBs.

In Chapter 3 we also investigated the boundaries of SBs and classified them as MHD discontinuities, revealing the presence of both open boundaries (rotational discontinuities) and closed ones (tangential discontinuities). This analysis required a careful application of the minimum variance analysis technique and therefore was applied to a small subset only of structures during PSP's first encounter with the Sun. A next obvious step would be to extend this analysis to other encounters in order to determine how the properties evolve radially. Of particular interest here would be to determine which type of boundary survives longer. One may expect rotational ones to be longer-lived because they are alfvénic and in the MHD approximation travel without distortion. Such an analysis, however, requires great caution because if new structures are indeed generated locally then this could bias the results. In fact, an increasing count of SBs per kilometer was observed in HELIOS data (Tenerani et al., 2021)), in constrast to what was found for PSP and Ulysses.

The second topic of this thesis is dedicated to the analysis and interpretation of the first ever observation of the magnetic signatures of the waves that belong to the slow extraordinary mode. Several works (e.g., Bale et al., 1998) had predicted or inferred the electromagnetic nature of these wave modes from properties such as the polarization of the electric field. However, no experience yet had revealed the magnetic signature of these waves. PSP thus offers the first direct evidence for the existence of a magnetic component. We were able to establish the link between these signatures and the wave propagation in inhomogeneous plasma, demonstrating that one of the key ingredients for their observation is the presence of density fluctuations associated with strong electric fields. This work has been published in (Larosa et al., 2022).

A further step of this work could be to perform a full Vlasov-Maxwell simulation (maybe with immovable ions), trying to reproduce the observed phenomenology, in order to obtain a more detailed understanding of the physics at play.

So far, in three years of observations, we have observed few events only with clear evidence of magnetic signatures. There are several possible reasons for this scarcity. One has to do with the small amplitude of the magnetic signatures, which often barely exceed the noise floor and the resolution of the TDS instrument that samples the high frequency waveforms. A shown by (Dudok de Wit et al., 2021), more events may potentially have a magnetic signature, which, however, is too weak to be seen because the amplitude of the electric field is relatively modest.

When moving closer to the Sun in the years to come, PSP will presumably observe stronger electric fields and also stronger density fluctuations (Krupar et al., 2020) which are favorable for the generation of the magnetic component. At the same time the noise level (turbulent fluctuations plus spacecraft related noise) should increase. Finally, electron beams should occur more frequently near the spacecraft, especially if the level of solar activity increases.

Taken together, these conditions should enable more frequent observations of the magnetic signature of slow extraordinary modes.

5.1 Résumé en français: Conclusions

Les observations du champ magnétique sont le leitmotiv de cette thèse. Parker Solar Probe nous a donné l'opportunité d'étudier les structures et les ondes du champ magnétique depuis les échelles MHD jusqu'à la fréquence plasma. Ces observations ont été effectuées dans l'héliosphère interne, dans un vent solaire jeune et beaucoup plus structuré que ce qui est habituellement observé à proximité de la Terre.

Dans cette thèse, nous nous sommes concentrés sur deux sujets différents. Le premier concerne les déflexions magnétiques soudaines, appelées switchbacks, qui sont omniprésentes dans le vent solaire lent et alfvénique. Ces switchbacks font actuellement l'objet de beaucoup d'attention. L'une des principales questions ouvertes est la nature des processus physiques qui leur donnent naissance.

Pour répondre à cette question, nous avons étudié les propriétés des switchbacks en étudiant de près leurs frontières. Nous avons aussi effectué l'analyse statistique détaillée d'un sous-ensemble de 70 switchbacks bien définis qui ont été observés lors du premier passage au Soleil de Parker Solar Probe, en novembre 2018.

Nous avons observé qu'environ 30% des switchbacks présentent des signatures de compression dans le champ magnétique, avec une corrélation ou une anticorrélation significative entre la magnitude du champ magnétique et les variations de densité des protons par rapport au plasma aux alentours. Ces (anti-)corrélations nous permettent de les classer en mode lent et rapide. Une telle classification est utile pour contraindre les différents mécanismes de génération de ces structures.

Dans le chapitre 3, nous passons en revue cinq modèles qui ont été récemment proposés pour expliquer l'origine des switchbacks. Le modèle proposé par Squire, Chandran, and Meyrand (2020) et par Mallet et al. (2021), qui interprètent les switchbacks comme le raidissement d'ondes d'Alfvén dans le vent solaire en expansion radiale, offrent le meilleur accord avec nos contraintes. Mallet et al. (2021) montrent que l'observation de la corrélation et de l'anticorrélation entre la magnitude du champ magnétique et la densité de protons dépend du β du plasma et de l'angle de propagation des switchbacks par rapport au champ magnétique moyen. Lorsque $\beta < 1$, nous avons une corrélation de type mode rapide alors que lorsque $\beta > 1$, nous avons une corrélation de type mode lent. La dépendance de l'angle de propagation qu'ils ont trouvée pourrait être testée par rapport à nos observations pour estimer la précision de leur modèle.

Un autre modèle prometteur est l'instabilité de type firehose pour les particules alpha. Il est intéressant de noter que l'anisotropie de la température des particules alpha diminue avec la distance radiale à partir de 0.3 UA (Stansby et al., 2019), ce qui est en accord avec le fait que les particules se trouvent près des seuils d'instabilité firehose. Cette évolution radiale est également cohérente avec la diminution du taux de switchbacks par kilomètre tel qu'elle a été estimée à partir des données de Parker Solar Probe et d'Ulysses par Tenerani et al. (2021). Cependant, la capacité de l'instabilité firehose des particules alpha à produire des structures de type mode lent et rapide n'a pas encore été étudiée en détail. Il s'agit clairement d'un sujet de travail futur. L'analyse statistique des switchbacks a été publiée dans (Larosa et al., 2021).

Le niveau accru de fluctuations magnétiques que nous observons à l'intérieur des switchbacks est cohérent avec d'autres observations (Dudok de Wit et al., 2020; Martinović et al., 2021). Cependant, la question de savoir si les switchbacks peuvent être considérés comme faisant partie ou non du champ turbulent reste ouverte.

Dans le chapitre 3, nous avons également étudié la frontière des switchbacks et les avons classées comme des discontinuités MHD, révélant la présence de frontières ouvertes (discontinuités rotationnelles) et fermées (discontinuités tangentielles). Cette analyse a nécessité une application minutieuse de la technique d'analyse de variance minimale et n'a donc été appliquée qu'à un petit sous-ensemble de 70 structures observées lors du premier passage au Soleil de Parker Solar Probe. Une prochaine étape évidente serait d'étendre cette analyse à d'autres rencontres afin de déterminer comment les propriétés évoluent radialement. Nous pensons cependant que son extension à différentes distances radiales pourrait être utile pour comprendre l'évolution des switchbacks. Une piste serait d'étudier la variation de la fraction rotationnelle et tangentielle des structures avec la distance, normalisée par le nombre de switchbacks à chaque distance. Il serait particulièrement intéressant de déterminer quel type de discontinuité survit le plus longtemps. On pourrait s'attendre à ce que les frontières rotationnelles aient une durée de vie plus longue car elles sont alfvéniques et, dans l'approximation MHD, se déplacent sans distorsion. Une telle analyse nécessite cependant une grande prudence car si de nouvelles structures sont effectivement générées localement, cela pourrait fausser les résultats. Dans les données de la mission Helios le nombre de switchbacks par kilomètre croît avec la distance au Solei (Tenerani et al., 2021) , contrairement à ce qui a été trouvé pour Parker Solar Probe et Ulysses.

Le second sujet de cette thèse est l'analyse et à l'interprétation de la toute première observation de signatures magnétiques d'ondes de type extraordinaire lent. Plusieurs travaux avaient prédit ou déduit la nature électromagnétique de ces modes d'ondes à partir de propriétés telles que la polarisation du champ électrique. Cependant, aucune sonde spatiale n'avait encore révélé la signature magnétique de ces ondes. Parker Solar Probe offre donc la première preuve directe de l'existence d'une composante magnétique. Nous avons pu établir le lien entre ces signatures et la propagation des ondes dans un plasma inhomogène, en démontrant que un des éléments-clé pour leur observation est la présence de fluctuations de densité associées à de forts champs électriques. Ce travail vient de paraître dans (Larosa et al., 2022).

Jusqu'à présent, en trois années d'observations, nous n'avons observé qu'un seul événement avec des preuves aussi claires de la signature magnétique. Il y a plusieurs raisons possibles à cela. L'une d'elles est liée à la faible amplitude de cette signature magnétique, qui dépasse souvent de peu le niveau de bruit. Comme l'ont montré Dudok de Wit et al. (2021), un plus grand nombre d'événements pourrait potentiellement avoir une signature magnétique, qui reste cependant trop faible pour être vue car l'amplitude du champ électrique est relativement modeste.

En se rapprochant du Soleil dans les années à venir, Parker Solar Probe observera vraisemblablement des champs électriques plus intenses ainsi que de plus grosses fluctuations de densité (Krupar et al., 2020). De telles conditions sont qui sont favorables à la génération de la composante magnétique. En même temps, le niveau de bruit devrait lui aussi augmenter. Enfin, les faisceaux d'électrons devraient être plus fréquents, surtout si l'activité solaire regagne en intensité. L'ensemble de ces conditions devrait permettre des observations plus fréquentes de la signature magnétique des modes extraordinaires lents.

Appendix A

Relation between $\vec{B}$, $\vec{E}$ and $\vec{N}$

In this appendix we detail the derivation of relation 4.2, with the objective to find the relationship between magnetic field $\vec{B}$, electric field $\vec{E}$ and the refractive index $\vec{N}$ by means of the linearised Vlasov-Maxwell, combined with the Faraday equation. In the following, $\vec{N}$ is a vector whose magnitude equals the value of the refractive index N and which is directed along the wave-vector $\vec{k}$ of the wave.

The linearised Vlasov-Maxwell system in the Fourier space for a cold plasma has the form of equation A.1, see for example equation 4.3.1.10 in Akhiezer et al., 1975.

$$\begin{pmatrix} \varepsilon_1 - \frac{k_z^2 c^2}{\omega^2} & -i\varepsilon_2 & \frac{k_x k_z c^2}{\omega^2} \\ i\varepsilon_2 & \varepsilon_1 - \frac{k^2 c^2}{\omega^2} & 0 \\ \frac{k_x k_z c^2}{\omega^2} & 0 & \varepsilon_3 - \frac{k_x^2 c^2}{\omega^2} \end{pmatrix} \begin{pmatrix} E_x \\ E_y \\ E_z \end{pmatrix} = 0 \tag{A.1}$$

Here the magnetic field is along the z direction and the wave-vector k is in the xz plane. We indicate with k_x, k_z, k the x component, the z component and the magnitude of the wave-vector respectively. As is customary, c indicates the light speed and ω the wave frequency. ε_1, ε_2 and ε_3 are the elements of the dielectric permittivity tensor of a cold plasma (see Akhiezer et al., 1975 eq 5.1.1.5) but in ε_3 we consider the contribution of the electron temperature. This is the largest input in the limit of $\omega_p \gg \Omega_c$. The equations in A.2 lead to an expression for a single species as we neglect the contribution of the ions since we are interested in high-frequency waves.

$$\varepsilon_1 = 1 - \frac{\omega_p^2}{\omega^2 - \Omega_c^2} \quad \varepsilon_2 = -\frac{\omega_p^2 \Omega_c}{\omega(\omega^2 - \Omega_c^2)} \quad \varepsilon_3 = 1 - \frac{\omega_p^2 (1 + 3k^2 \lambda_D^2)}{\omega^2} \tag{A.2}$$

From equation A.1 we can obtain two components of the electric field as functions of the third one (we know that the matrix must not have maximum rank in order to avoid trivial solutions). The choice of E_z as the free one gives equation A.3, where $N = \frac{kc}{\omega}$ is the refractive index.

$$\mathbf{E} = \begin{pmatrix} -\frac{(\varepsilon_3 - N^2 \sin^2\theta)}{N^2 \sin\theta\cos\theta} \\ i\frac{\varepsilon_2}{(\varepsilon_1 - N^2)} \frac{(\varepsilon_3 - N^2 \sin^2\theta)}{N^2 \sin\theta\cos\theta} \\ 1 \end{pmatrix} E_z. \tag{A.3}$$

Let us rewrite equation A.3 as

$$N^2 \sin\theta\cos\theta \mathbf{E} = \begin{pmatrix} -(\varepsilon_3 - N^2 \sin^2\theta) \\ i\frac{\varepsilon_2(\varepsilon_3 - N^2 \sin^2\theta)}{(\varepsilon_1 - N^2)} \\ N^2 \sin\theta\cos\theta \end{pmatrix} E_z; \tag{A.4}$$

which, considering that $N \gg 1$, takes the form:

$$N^2 \sin\theta\cos\theta \mathbf{E} = \begin{pmatrix} N^2 \sin^2\theta - \varepsilon_3) \\ \frac{i\varepsilon_2}{N^2}(1 + \frac{\varepsilon_1}{N^2})(N^2 \sin^2\theta - \varepsilon_3) \\ N^2 \sin\theta\cos\theta \end{pmatrix} E_z. \tag{A.5}$$

We can use this last expression in the Faraday equation in the Fourier space in order to have a relation between electric and magnetic fields and the refractive index. We have $\mathbf{B} = \mathbf{N} \times \mathbf{E}$ and we can multiply both sides by $N^2 \sin\theta\cos\theta$ from this follows:

$$N^2 \sin\theta\cos\theta \mathbf{B} = \begin{pmatrix} -i\frac{\varepsilon_2}{N^2}(1 + \frac{\varepsilon_1}{N^2})(N^2 \sin^2\theta - \varepsilon_3) N\cos\theta \\ -N\cos\theta\varepsilon_3 \\ iN\sin\theta\frac{\varepsilon_2}{N^2}(1 + \frac{\varepsilon_1}{N^2})(N^2 \sin^2\theta - \varepsilon_3) \end{pmatrix} E_z. \tag{A.6}$$

Let us simplify with some approximations, considering that $N \gg \varepsilon_1$:

$$\mathbf{B} \simeq \begin{pmatrix} -i\frac{\varepsilon_2}{N^3 \sin\theta}(N^2 \sin^2\theta - \varepsilon_3) \\ -\frac{\varepsilon_3}{N \sin\theta} \\ i\frac{1}{N^3 \cos\theta}\varepsilon_2(N^2 \sin^2\theta - \varepsilon_3) \end{pmatrix} E_z. \tag{A.7}$$

At this point is useful to consider the explicit form of ε_3 using the dispersion relation

$$\begin{aligned} \varepsilon_3 &= 1 - \frac{\omega_p^2(1+3k^2\lambda_D^2)}{\omega^2} \\ &= \frac{\omega_p^2(1+3k_z^2\lambda_D^2) + \Omega_c^2 \sin^2\theta(1-\frac{\omega_p^2}{k^2c^2}) - \omega_p^2(1+3k^2\lambda_D^2)}{\omega^2} \\ &= \frac{-3k^2\lambda_D^2\omega_p^2 \sin^2\theta + \Omega_c^2 \sin^2\theta(1-\frac{\omega_p^2}{k^2c^2})}{\omega^2} \\ &= [-3k^2\lambda_D^2 + \frac{\Omega_c^2}{\omega_p^2}(1-\frac{\omega_p^2}{k^2c^2})] \sin^2\theta. \end{aligned} \tag{A.8}$$

Equation A.8 reveals, taking into account the considerations of Section 4.4.1, that ε_3 is much smaller than one, allowing us to approximate the term $N^2 \sin^2\theta - \varepsilon_3$ by $N^2 \sin^2\theta$ in equation A.7. Considering that $E_z = E\cos\theta$, $\varepsilon_2 \simeq \frac{\Omega_c}{\omega_p}$ and using equations A.8 and A.7 gives:

$$\mathbf{B} \simeq \begin{pmatrix} -i\frac{\Omega_c}{\omega_p}\frac{\cos\theta\sin\theta}{N} \\ -\frac{\cos\theta\sin\theta}{N}[-3k^2\lambda_D^2 + \frac{\Omega_c^2}{\omega_p^2}(1-\frac{\omega_p^2}{k^2c^2})] \\ i\frac{\Omega_c}{\omega_p}\frac{\sin^2\theta}{N} \end{pmatrix} E. \tag{A.9}$$

Following the considerations made earlier we know that $k^2\lambda_D^2 \gg \frac{\Omega_c^2}{\omega_p^2}$. This allows us to further approximate equation A.9 and obtain our final result for the magnetic field component of the slow extraordinary wave:

$$\mathbf{B} \simeq \begin{pmatrix} -i\frac{\Omega_c}{\omega_p}\frac{\cos\theta\sin\theta}{N} \\ 3k^2\lambda_D^2\frac{\cos\theta\sin\theta}{N} \\ i\frac{\Omega_c}{\omega_p}\frac{\sin^2\theta}{N} \end{pmatrix} E \tag{A.10}$$

As expected, all the components of the magnetic field vanish when $\theta \to 0$.

Appendix B

Hamiltonian system approach

In this appendix we detail the calculations that lead to a hamiltonian system of equations for the dispersion relation of slow extraordinary waves given in equation 4.7.

Let us start from equation 4.4, which expresses the dispersion relation for quasi-electrostatic slow extraordinary waves. In the following, we neglect the contribution from ions and without loss of generality consider the magnetic field be along the z direction. If we define the components of the wave-vector as as $k_z = k\cos\theta$ and $k_x = k\sin\theta$, then

$$\omega = \omega_p \left[1 + \frac{3}{2} k_z^2 \lambda_D^2 + \frac{\Omega_c^2}{2\omega_p^2} \frac{k_x^2}{k^2} \left(1 - \frac{\omega^2}{c^2 k^2} \right) \right]. \tag{B.1}$$

The hamiltonian system 4.6, expresed in individual components, reads:

$$\frac{dk_x}{dt} = -\frac{\partial \omega}{\partial x} \tag{B.2a}$$

$$\frac{dk_z}{dt} = -\frac{\partial \omega}{\partial z} \tag{B.2b}$$

$$\frac{dx}{dt} = V_{gr_x} = \frac{\partial \omega}{\partial k_x} \tag{B.2c}$$

$$\frac{dz}{dt} = V_{gr_z} = \frac{\partial \omega}{\partial k_z} \tag{B.2d}$$

Equation B.2b becomes after applying the derivative and considering as variable parameters only Ω_c and the density (which is implicit in the Debye length)

$$\frac{dk_z}{dt} = \frac{\omega_p}{2n_0}\frac{\partial n}{\partial z} + \frac{\Omega_c^2}{\omega_p^2}\frac{k_x^2}{k^2}(1 - \frac{\omega_p^2}{k^2c^2})\frac{\partial \Omega_c}{\partial z}. \tag{B.3}$$

Since the magnetic field is one-directional and solenoidal the term $\frac{\partial \Omega_c}{\partial z}$ must vanish and equation B.3 reads:

$$\frac{dk_z}{dt} = \frac{\omega_p}{2n_0}\frac{\partial n}{\partial z}. \tag{B.4}$$

In equation B.2d the right hand side (rhs) is equal to $3\omega_p\lambda_D^2 k_z$. Now let us consider equation B.2c, for which the explicit form of the rhs is

$$\begin{aligned}\frac{\partial \omega}{\partial k_x} &= \frac{\Omega_p^2}{2\omega_p}\frac{\partial}{\partial k_x}\left(\frac{k_x^2}{k^2} - \frac{\omega_p^2}{c^2}\frac{k_x^2}{k^4}\right)\\ &= \frac{\Omega_p^2}{\omega_p}\frac{k_x}{k^4}\left(k_z^2 - \frac{\omega_p^2}{c^2}\frac{k^2 - 2k_x^2}{k^2}\right).\\ &= \frac{\Omega_p^2}{\omega_p}\frac{k_x}{k^4}\left(k_z^2 - \frac{\omega_p^2}{c^2}\frac{k_z^2 - k_x^2}{k^2}\right)\end{aligned} \tag{B.5}$$

The derivative on the rhs of equation B.2a is expressed in equation B.6

$$\frac{\partial \omega}{\partial x} = \frac{\omega_p}{2n_0}\frac{\partial n}{\partial x} + \frac{\Omega_c}{\omega_p}\frac{k_x^2}{k^2}\left(1 - \frac{\omega_p^2}{k^2c^2}\right)\frac{\partial \Omega_c}{\partial x}. \tag{B.6}$$

System B.2 then reads

$$\frac{dk_x}{dt} = \frac{\omega_p}{2n_0}\frac{\partial n}{\partial x} + \frac{\Omega_c}{\omega_p}\frac{k_x^2}{k^2}\left(1 - \frac{\omega_p^2}{k^2c^2}\right)\frac{\partial \Omega_c}{\partial x} \tag{B.7a}$$

$$\frac{dk_z}{dt} = -\frac{\omega_p}{2n_0}\frac{\partial n}{\partial z} \tag{B.7b}$$

$$\frac{dx}{dt} = \frac{\Omega_p^2}{\omega_p}\frac{k_x}{k^4}\left(k_z^2 - \frac{\omega_p^2}{c^2}\frac{k_z^2 - k_x^2}{k^2}\right) \tag{B.7c}$$

$$\frac{dz}{dt} = \omega_p\lambda_D^2 k_z \tag{B.7d}$$

In order to perform a numerical simulation we normalize system B.7 by using the dimensionless variables $\hat{k} = k\lambda_D$, $\hat{t} = t\omega_p$, $\hat{x} = \frac{x}{\lambda_D}$, $\hat{z} = \frac{z}{\lambda_D}$. We introduce the variable $\xi = \frac{\Omega_c}{\omega_p}$ and the constant $v = \frac{v_{th}}{c}$. Using these definitions, we obtain the normalized system of equations 4.7, which are the basis for the simulations that are run and discussed in Section 4.5.

Bibliography

Agapitov, O. V. et al. (Feb. 2020). "Sunward-propagating Whistler Waves Collocated with Localized Magnetic Field Holes in the Solar Wind: Parker Solar Probe Observations at 35.7 Solar Radii". In: *The Astrophysical Journal Letters* 891.1, p. L20. DOI: 10.3847/2041-8213/ab799c.

Akhiezer, A. I. et al. (Jan. 1975). "Plasma electrodynamics. Volume 1 - Linear theory. Volume 2 - Non-linear theory and fluctuations". In: *Oxford Pergamon Press International Series on Natural Philosophy* 1.

Alfvén, H. (Jan. 1957). "On the theory of comet tails." In: *Tellus* 9, p. 92. DOI: 10.3402/tellusa.v9i1.9064.

Artemyev, Anton V. et al. (May 2018). "Dynamics of Intense Currents in the Solar Wind". en. In: *The Astrophysical Journal* 859.2, p. 95. ISSN: 1538-4357. DOI: 10.3847/1538-4357/aabe89.

Bale, S. D. et al. (1996). "Phase coupling in Langmuir wave packets: Possible evidence of three-wave interactions in the upstream solar wind". In: *Geophysical Research Letters* 23, pp. 109–112. DOI: 10.1029/95GL03595.

Bale, S. D. et al. (1998). "Transverse z-mode waves in the terrestrial electron foreshock". In: *Geophysical Research Letters* 25, pp. 9–12. DOI: 10.1029/97GL03493.

Bale, S. D. et al. (Dec. 2016). "The FIELDS Instrument Suite for Solar Probe Plus. Measuring the Coronal Plasma and Magnetic Field, Plasma Waves and Turbulence, and Radio Signatures of Solar Transients". In: *Space Science Reviews* 204.1-4, pp. 49–82. DOI: 10.1007/s11214-016-0244-5.

Bale, S. D. et al. (Dec. 2019). "Highly structured slow solar wind emerging from an equatorial coronal hole". In: *Nature* 576.7786, pp. 237–242. DOI: 10.1038/s41586-019-1818-7.

Bale, S. D. et al. (Dec. 2019). "Highly structured slow solar wind emerging from an equatorial coronal hole". en. In: *Nature* 576.7786, pp. 237–242. ISSN: 0028-0836, 1476-4687. DOI: 10.1038/s41586-019-1818-7.

Bale, S. D. et al. (Dec. 2021). "A Solar Source of Alfvénic Magnetic Field Switchbacks: In Situ Remnants of Magnetic Funnels on Supergranulation Scales". In: 923.2, 174, p. 174. DOI: 10.3847/1538-4357/ac2d8c. arXiv: 2109.01069 [astro-ph.SR].

Balogh, A. et al. (Jan. 1999). "Heliospheric magnetic field polarity inversions at high heliographic latitudes". In: *Geophysical Research Letters* 26.6, pp. 631–634. DOI: 10.1029/1999GL900061.

Balogh, André and Géza Erdõs (June 2013). "The Heliospheric Magnetic Field". In: *Space Science Reviews* 176.1-4, pp. 177–215. DOI: 10.1007/s11214-011-9835-3.

Bastian, T. S., A. O. Benz, and D. E. Gary (1998). "Radio Emission from Solar Flares". In: *Annual Review Astronomy Astrophysics* 36, pp. 131–188. DOI: 10.1146/annurev.astro.36.1.131.

Biermann, L. (Jan. 1951). "Kometenschweife und solare Korpuskularstrahlung". In: *Zeitschrift für Astrophysik* 29, p. 274.

Borovsky, Joseph E. (Sept. 2010). "Contribution of Strong Discontinuities to the Power Spectrum of the Solar Wind". en. In: *Physical Review Letters* 105.11, p. 111102. ISSN: 0031-9007, 1079-7114. DOI: 10.1103/PhysRevLett.105.111102.

Bowen, Trevor A. et al. (Feb. 2020). "Ion-scale Electromagnetic Waves in the Inner Heliosphere". In: *The Astrophysical Journal Supplement Series* 246.2, p. 66. DOI: 10.3847/1538-4365/ab6c65.

Braginskii, S. I. (Jan. 1965). "Transport Processes in a Plasma". In: *Reviews of Plasma Physics* 1, p. 205.

Bruno, R. and V. Carbone (Sept. 2013). "The Solar Wind as a Turbulence Laboratory". In: *Living Reviews in Solar Physics* 2, p. 4. DOI: 10.12942/lrsp-2013-2.

Burlaga, Leonard F. (May 1968). "Micro-scale structures in the interplanetary medium". en. In: *Solar Physics* 4.1, pp. 67–92. ISSN: 0038-0938, 1573-093X. DOI: 10.1007/BF00146999.

Burlaga, Leonard F. and Norman F. Ness (Oct. 1969). "Tangential Discontinuities in the Solar Wind". In: *Solar Physics* 9.2, pp. 467–477. DOI: 10.1007/BF02391672.

Case, A. W. et al. (Feb. 2020). "The Solar Probe Cup on the Parker Solar Probe". In: *The Astrophysical Journal Supplement* 246.2, 43, p. 43. DOI: 10.3847/1538-4365/ab5a7b.

Chapman, Sydney and Harold Zirin (Jan. 1957). "Notes on the Solar Corona and the Terrestrial Ionosphere". In: *Smithsonian Contributions to Astrophysics* 2, p. 1.

Chaston, C. C. et al. (Mar. 2020). "MHD Mode Composition in the Inner Heliosphere from the *Parker Solar Probe* 's First Perihelion". en. In: *The Astrophysical Journal Supplement Series* 246.2, p. 71. ISSN: 1538-4365. DOI: 10.3847/1538-4365/ab745c.

Chen, C. H. K. (Nov. 2016). "Recent progress in astrophysical plasma turbulence from solar wind observations". In: *Journal of Plasma Physics* 82.6, p. 535820602. DOI: 10.1017/S0022377816001124.

Chen, Q., A. Otto, and L. C. Lee (Jan. 1997). "Tearing instability, Kelvin-Helmholtz instability, and magnetic reconnection". In: *Journal of Geophysical Research* 102.A1, pp. 151–162. DOI: 10.1029/96JA03144.

Cohen, R. H. and R. M. Kulsrud (Dec. 1974). "Nonlinear evolution of parallel-propagating hydromagnetic waves." In: *Physics of Fluids* 17, pp. 2215–2225. DOI: 10.1063/1.1694695.

Cranmer, Steven R., Adriaan A. van Ballegooijen, and Richard J. Edgar (Aug. 2007). "Self-consistent Coronal Heating and Solar Wind Acceleration from Anisotropic Magnetohydrodynamic Turbulence". In: *The Astrophysical Journal Supplement* 171.2, pp. 520–551. DOI: 10.1086/518001.

Culhane, J. L. et al. (Oct. 2014). "Tracking Solar Active Region Outflow Plasma from Its Source to the Near-Earth Environment". In: *Solar Physics* 289.10, pp. 3799–3816. DOI: 10.1007/s11207-014-0551-5.

D'Amicis, R. and R. Bruno (May 2015). "On the origin of highly alfvénic slow solar wind". In: 805.1, p. 84. DOI: 10.1088/0004-637x/805/1/84.

DeForest, C. E. et al. (June 2016). "Fading Coronal Structure and the Onset of Turbulence in the Young Solar Wind". In: *The Astronomical Journal* 828.2, p. 66. DOI: 10.3847/0004-637X/828/2/66.

Drake, J. F. et al. (June 2021). "Switchbacks as signatures of magnetic flux ropes generated by interchange reconnection in the corona". In: *Astronomy & Astrophysics* 650, A2, A2. DOI: 10.1051/0004-6361/202039432.

Dudok de Wit, T. et al. (2021). "Three years of results from the SCM search-coil on Parker Solar Probe". In: *Journal of Geophysical Research* submitted.

Dudok de Wit, Thierry et al. (Feb. 2020). "Switchbacks in the Near-Sun Magnetic Field: Long Memory and Impact on the Turbulence Cascade". In: *The Astrophysical Journal Supplement* 246.2, 39, p. 39. DOI: 10.3847/1538-4365/ab5853.

Ergun, R. E. et al. (Apr. 2018). "Magnetic Reconnection, Turbulence, and Particle Acceleration: Observations in the Earth's Magnetotail". In: *Geophysical Research Letters* 45.8, pp. 3338–3347. DOI: 10.1002/2018GL076993.

Fargette, Naïs et al. (Sept. 2021). "Characteristic scales of magnetic switchback patches near Sun and their possible association with solar supergranulation and granulation". In: *arXiv e-prints*, arXiv:2109.01519.

Farrell, W M (2020). "Magnetic Field Dropouts at Near-Sun Switchback Boundaries: A Superposed Epoch Analysis". en. In: *The Astrophysical Journal Supplement Series*, p. 10.

Farrell, W. M. et al. (Aug. 2020). "Magnetic Field Dropouts at Near-Sun Switchback Boundaries: A Superposed Epoch Analysis". In: *The Astrophysical Journal Supplement* 249.2, 28, p. 28. DOI: 10.3847/1538-4365/ab9eba.

Fisk, L. A. (Apr. 2003). "Acceleration of the solar wind as a result of the reconnection of open magnetic flux with coronal loops". In: *Journal of Geophysical Research (Space Physics)* 108.A4, 1157, p. 1157. DOI: 10.1029/2002JA009284.

— (June 2005). "The Open Magnetic Flux of the Sun. I. Transport by Reconnections with Coronal Loops". In: *The Astrophysical Journal* 626.1, pp. 563–573. DOI: 10.1086/429957.

Fisk, L. A. and J. C. Kasper (Apr. 2020). "Global Circulation of the Open Magnetic Flux of the Sun". en. In: *The Astrophysical Journal* 894.1, p. L4. ISSN: 2041-8213. DOI: 10.3847/2041-8213/ab8acd.

Fisk, L. A., N. A. Schwadron, and T. H. Zurbuchen (Sept. 1999). "Acceleration of the fast solar wind by the emergence of new magnetic flux". In: *Journal of Geophysical Research* 104.A9, pp. 19765–19772. DOI: 10.1029/1999JA900256.

Foukal, Peter V. (2004). *Solar Astrophysics, 2nd, Revised Edition*.

Fox, N. J. et al. (Nov. 2015). "The Solar Probe Plus Mission: Humanity's First Visit to Our Star". In: *Space Science Reviews* 204.1–4, pp. 7–48. ISSN: 1572-9672. DOI: 10.1007/s11214-015-0211-6. URL: http://dx.doi.org/10.1007/s11214-015-0211-6.

— (Dec. 2016). "The Solar Probe Plus Mission: Humanity's First Visit to Our Star". en. In: *Space Science Reviews* 204.1-4, pp. 7–48. ISSN: 0038-6308, 1572-9672. DOI: 10.1007/s11214-015-0211-6.

Froment, C. et al. (June 2021). "Direct evidence for magnetic reconnection at the boundaries of magnetic switchbacks with Parker Solar Probe".

In: *Astronomy and Astrophysics* 650, A5. DOI: 10.1051/0004-6361/202039806.

Galeev, A. A. et al. (Oct. 1977a). "Langmuir turbulence and dissipation of high frequency energy". In: *Zhurnal Eksperimentalnoi i Teoreticheskoi Fiziki* 73, pp. 1352–1369.

— (Feb. 1977b). "Relaxation of high-current electron beams and the modulational instability". In: *Zhurnal Eksperimentalnoi i Teoreticheskoi Fiziki* 72, pp. 507–517.

Gary, S. Peter (1993). *Theory of Space Plasma Microinstabilities.*

Ginzburg, V. L. and V. V. Zhelezniakov (Jan. 1958). "On the Possible Mechanisms of Sporadic Solar Radio Emission (Radiation in an Isotropic Plasma)". In: *Astronomicheskii Zhurnal* 35, p. 694.

Gosling, J. T. et al. (Apr. 2009). "A One-Sided Aspect of Alfvénic Fluctuations in the Solar Wind". In: *The Astrophysical Journal Letters* 695.2, pp. L213–L216. DOI: 10.1088/0004-637X/695/2/L213.

Grappin, R., M. Velli, and A. Mangeney (June 1991). ""Alfvénic" versus "standard" turbulence in the solar wind." In: *Annales Geophysicae* 9, pp. 416–426.

Grappin, Roland, Andre Mangeney, and Eckart Marsch (June 1990). "On the origin of solar wind MHD turbulence: Helios data revisited". In: *Journal of Geophysical Research* 95.A6, pp. 8197–8209. DOI: 10.1029/JA095iA06p08197.

Grappin, Roland, Marco Velli, and André Mangeney (Apr. 1993). "Nonlinear wave evolution in the expanding solar wind". In: *Physical Research Letters* 70.14, pp. 2190–2193. DOI: 10.1103/PhysRevLett.70.2190.

Gurnett, D. A. and L. A. Frank (Dec. 1975). "Electron Plasma Oscillations Associated with Type III Radio Emissions and Solar Electrons". In: *Solar Physics* 45.2, pp. 477–493. DOI: 10.1007/BF00158464.

Gurnett, D. A. et al. (Feb. 1995). "The Polar Plasma Wave Instrument". In: *Space Science Reviews* 71, pp. 597–622. DOI: 10.1007/BF00751343.

Halekas, J. S. et al. (Feb. 2020). "Electrons in the Young Solar Wind: First Results from the *Parker Solar Probe*". en. In: *The Astrophysical Journal Supplement Series* 246.2, p. 22. ISSN: 1538-4365. DOI: 10.3847/1538-4365/ab4cec.

Hau, L. N. and B. U. Ö. Sonnerup (Sept. 1993). "On slow-mode waves in an anisotropic plasma". en. In: *Geophysical Research Letters* 20.17, pp. 1763–1766. ISSN: 00948276. DOI: 10.1029/93GL01706.

Hellinger, P. and H. Matsumoto (May 2000). “New kinetic instability: Oblique Alfvén fire hose”. en. In: *Journal of Geophysical Research: Space Physics* 105.A5, pp. 10519–10526. ISSN: 01480227. DOI: 10.1029/1999JA000297.

Hellinger, Petr and Pavel TráVníčEk (Jan. 2006). “Parallel and oblique proton fire hose instabilities in the presence of alpha/proton drift: Hybrid simulations”. In: *Journal of Geophysical Research (Space Physics)* 111.A1, A01107, A01107. DOI: 10.1029/2005JA011318.

Hinkel-Lipsker, D. E., B. D. Fried, and G. J. Morales (Apr. 1991). “Conversion of electrostatic and electromagnetic waves in a plasma at the peak of a parabolic density profile”. en. In: *Physical Review Letters* 66.14, pp. 1862–1865. ISSN: 0031-9007. DOI: 10.1103/PhysRevLett.66.1862.

Hoffmeister, C. (Jan. 1943). “Physikalische Untersuchungen an Kometen. I. Die Beziehungen des primären Schweifstrahls zum Radiusvektor. Mit 2 Abbildungen.” In: *Zeitschrift für Astrophysik* 22, p. 265.

Hollweg, J. V. (Oct. 1982). “Surface Waves on solar wind tangential discontinuities”. In: *Journal of Geophysical Research* 87.A10, pp. 8065–8076. DOI: 10.1029/JA087iA10p08065.

Horbury, T. S., L. Matteini, and D. Stansby (Aug. 2018). “Short, large-amplitude speed enhancements in the near-Sunfast solar wind”. In: *Monthly Notices of the Royal Astronomical Society* 478.2, pp. 1980–1986. DOI: 10.1093/mnras/sty953.

Horbury, Timothy S. et al. (Feb. 2001). “Three spacecraft observations of solar wind discontinuities”. en. In: *Geophysical Research Letters* 28.4, pp. 677–680. ISSN: 00948276. DOI: 10.1029/2000GL000121.

Horbury, Timothy S. et al. (Feb. 2020). “Sharp Alfvénic Impulses in the Near-Sun Solar Wind”. en. In: *The Astrophysical Journal Supplement Series* 246.2, p. 45. ISSN: 1538-4365. DOI: 10.3847/1538-4365/ab5b15.

Huang, Jia et al. (Mar. 2020). “Proton Temperature Anisotropy Variations in Inner Heliosphere Estimated with the First *Parker Solar Probe* Observations”. en. In: *The Astrophysical Journal Supplement Series* 246.2, p. 70. ISSN: 1538-4365. DOI: 10.3847/1538-4365/ab74e0.

Jagarlamudi, V. K. et al. (June 2021). “Whistler wave occurrence and the interaction with strahl electrons during the first encounter of Parker Solar Probe”. In: *Astronomy & Astrophysics* 650, A9, A9. DOI: 10.1051/0004-6361/202039808. arXiv: 2101.06723 [physics.space-ph].

Jannet, G. et al. (Feb. 2021). “Measurement of Magnetic Field Fluctuations in the Parker Solar Probe and Solar Orbiter Missions”. en. In: *Journal of*

Geophysical Research: Space Physics 126.2. ISSN: 2169-9380, 2169-9402. DOI: 10.1029/2020JA028543.

Kasper, J. C. et al. (Dec. 2019). "Alfvénic velocity spikes and rotational flows in the near-Sun solar wind". In: *Nature* 576.7786, pp. 228–231. DOI: 10.1038/s41586-019-1813-z.

Kasper, Justin C. et al. (Dec. 2016a). "Solar Wind Electrons Alphas and Protons (SWEAP) Investigation: Design of the Solar Wind and Coronal Plasma Instrument Suite for Solar Probe Plus". In: *Space Science Reviews* 204.1-4, pp. 131–186. DOI: 10.1007/s11214-015-0206-3.

Kasper, Justin C. et al. (Dec. 2016b). "Solar Wind Electrons Alphas and Protons (SWEAP) Investigation: Design of the Solar Wind and Coronal Plasma Instrument Suite for Solar Probe Plus". In: *Space Science Reviews* 204.1-4, pp. 131–186. DOI: 10.1007/s11214-015-0206-3.

Kellogg, P. J. et al. (Aug. 1999). "Langmuir waves in a fluctuating solar wind". In: *Journal of Geophysical Research* 104, pp. 17069–17078. DOI: 10.1029/1999JA900163.

Kellogg, P. J. et al. (2013). "Observations of transverse Z mode and parametric decay in the solar wind". In: *Journal of Geophysical Research: Space Physics* 118.8, pp. 4766–4775. ISSN: 2169-9402. DOI: 10.1002/jgra.50443. URL: http://dx.doi.org/10.1002/jgra.50443.

Kiyani, Khurom H., Kareem T. Osman, and Sandra C. Chapman (Apr. 2015). "Dissipation and heating in solar wind turbulence: from the macro to the micro and back again". In: *Philosophical Transactions of the Royal Society of London A: Mathematical, Physical and Engineering Sciences* 373.2041. DOI: 10.1098/rsta.2014.0155.

Klein, K. G. and G. G. Howes (Mar. 2015). "Predicted impacts of proton temperature anisotropy on solar wind turbulence". In: *Physics of Plasmas* 22.3, p. 032903. DOI: 10.1063/1.4914933.

Krasnoselskikh, V. et al. (Apr. 2020). "Localized Magnetic-field Structures and Their Boundaries in the Near-Sun Solar Wind from Parker Solar Probe Measurements". en. In: *The Astrophysical Journal* 893.2, p. 93. ISSN: 0004-637X. DOI: 10.3847/1538-4357/ab7f2d.

Krasnoselskikh, V. V., T. Dudok de Wit, and S. D. Bale (Mar. 2011). "Determining the wavelength of Langmuir wave packets at the Earth's bow shock". In: *Annales Geophysicae* 29, pp. 613–617. DOI: 10.5194/angeo-29-613-2011. eprint: 1107.4439 (physics.space-ph).

Krasnoselskikh, Vladimir, Andrii Voshchepynets, and Milan Maksimovic (July 2019). "On the Efficiency of the Linear-mode Conversion for Generation of Solar Type III Radio Bursts". en. In: *The Astrophysical Journal* 879.1, p. 51. ISSN: 1538-4357. DOI: 10.3847/1538-4357/ab22bf.

Krupar, V. et al. (Apr. 2018). "Interplanetary Type III Bursts and Electron Density Fluctuations in the Solar Wind". In: 857.2, p. 82. DOI: 10.3847/1538-4357/aab60f. URL: https://doi.org/10.3847/1538-4357/aab60f.

Krupar, Vratislav et al. (Feb. 2020). "Density Fluctuations in the Solar Wind Based on Type III Radio Bursts Observed by Parker Solar Probe". In: *The Astrophysical Journal Supplement* 246.2, p. 57. DOI: 10.3847/1538-4365/ab65bd.

Laker, R. et al. (June 2021). "Statistical analysis of orientation, shape, and size of solar wind switchbacks". In: *Astronomy & Astrophysics* 650, A1, A1. DOI: 10.1051/0004-6361/202039354.

Larosa, A. et al. (June 2021). "Switchbacks: statistical properties and deviations from Alfvénicity". In: *Astronomy & Astrophysics* 650, A3, A3. DOI: 10.1051/0004-6361/202039442.

Larosa, A. et al. (2022). "Slow extraordinary mode magnetic signatures observations with Parker Solar Probe". In: *The Astrophysical Journal* submitted.

Leblanc, Yolande, George A. Dulk, and Jean-Louis Bougeret (Nov. 1998). "Tracing the Electron Density from the Corona to 1au". In: *Solar Physics* 183.1, pp. 165–180. DOI: 10.1023/A:1005049730506.

Lin, R. P. and H. S. Hudson (Apr. 1971). "10-100 keV electron acceleration and emission from solar flares". In: *Solar Physics* 17.2, pp. 412–435. DOI: 10.1007/BF00150045.

Lin, R. P. et al. (Dec. 1981). "Energetic electrons and plasma waves associated with a solar type III radio burst". en. In: *The Astrophysical Journal* 251, p. 364. ISSN: 0004-637X, 1538-4357. DOI: 10.1086/159471.

Maksimovic, M. et al. (Sept. 2005). "Radial evolution of the electron distribution functions in the fast solar wind between 0.3 and 1.5 AU". In: *Journal of Geophysical Research (Space Physics)* 110.A9, A09104. DOI: 10.1029/2005JA011119.

Malaspina, D. M. and R. E. Ergun (Dec. 2008). "Observations of three-dimensional Langmuir wave structure: 3D Langmuir structure". en. In: *Journal of Geophysical Research: Space Physics* 113.A12, n/a–n/a. ISSN: 01480227. DOI: 10.1029/2008JA013656.

Malaspina, David M., Iver H. Cairns, and Robert E. Ergun (July 2011). "Dependence of Langmuir wave polarization on electron beam speed in type

III solar radio bursts". In: *Geophysical Research Letters* 38.13, L13101, p. L13101. DOI: 10.1029/2011GL047642.

Malaspina, David M., Iver H. Cairns, and Robert E. Ergun (July 2011). "Dependence of Langmuir wave polarization on electron beam speed in type III solar radio bursts: Langmuir wave polariszation". en. In: *Geophysical Research Letters* 38.13. DOI: 10.1029/2011GL047642.

Malaspina, David M. et al. (June 2016). "The Digital Fields Board for the FIELDS instrument suite on the Solar Probe Plus mission: Analog and digital signal processing". In: *Journal of Geophysical Research (Space Physics)* 121.6, pp. 5088–5096. DOI: 10.1002/2016JA022344.

Mallet, Alfred et al. (Sept. 2021). "Evolution of Large-amplitude Alfvén Waves and Generation of Switchbacks in the Expanding Solar Wind". In: *The Astrophysical Journal* 918.2, 62, p. 62. DOI: 10.3847/1538-4357/ac0c12.

Marsch, E., X. Z. Ao, and C. Y. Tu (Apr. 2004). "On the temperature anisotropy of the core part of the proton velocity distribution function in the solar wind". In: *Journal of Geophysical Research (Space Physics)* 109.A4, A04102. DOI: 10.1029/2003JA010330.

Martinović, Mihailo M. et al. (May 2021). "Multiscale Solar Wind Turbulence Properties inside and near Switchbacks Measured by the Parker Solar Probe". In: *The Astrophysical Journal* 912.1, p. 28. DOI: 10.3847/1538-4357/abebe5.

Matteini, L. et al. (Oct. 2015). "Fire Hose Instability Driven by Alpha Particle Temperature Anisotropy". In: *The Astrophysical Journal* 812.1, p. 13. DOI: 10.1088/0004-637X/812/1/13.

Matthaeus, W. H. et al. (Apr. 6, 2015). "Intermittency, nonlinear dynamics and dissipation in the solar wind and astrophysical plasmas". In: *Philosophical Transactions of the Royal Society of London A: Mathematical, Physical and Engineering Sciences* 373.2041. DOI: 10.1098/rsta.2014.0154.

McComas, D. J. et al. (Dec. 2016). "Integrated Science Investigation of the Sun (ISIS): Design of the Energetic Particle Investigation". en. In: *Space Science Reviews* 204.1-4, pp. 187–256. ISSN: 0038-6308, 1572-9672. DOI: 10.1007/s11214-014-0059-1.

McManus, Michael D. et al. (Feb. 2020). "Cross Helicity Reversals in Magnetic Switchbacks". In: *The Astrophysical Journal Supplement Series* 246.2, p. 67. DOI: 10.3847/1538-4365/ab6dce.

Mel'Nik, V. N. (1995). *"Gas-dynamic" expansion of a fast-electron flux in a plasma*. arXiv: 1802.07806 [physics.plasm-ph].

Mel'Nik, V. N., V. Lapshin, and E. Kontar (Feb. 1999). "Propagation of a Monoenergetic Electron Beam in the Solar Corona". In: *Solar Physics* 184.2, pp. 353–362. DOI: 10.1023/A:1005191910544.

Melrose, D. B. (July 1982). "Fundamental Emission for Type-Iii Bursts in the Interplanetary Medium - the Role of Ion-Sound Turbulence". In: *Solar Physics* 79.1, pp. 173–185. DOI: 10.1007/BF00146981.

Meyer-Vernet, N., K. Issautier, and M. Moncuquet (Aug. 2017). "Quasi-thermal noise spectroscopy: The art and the practice". In: *Journal of Geophysical Research (Space Physics)* 122.8, pp. 7925–7945. DOI: 10.1002/2017JA024449.

Miles, David M. et al. (Oct. 2018). "A hybrid fluxgate and search coil magnetometer concept using a racetrack core". In: *Geoscientific Instrumentation, Methods and Data Systems* 7.4, pp. 265–276. DOI: 10.5194/gi-7-265-2018.

Moncuquet, Michel et al. (Feb. 2020). "First In Situ Measurements of Electron Density and Temperature from Quasi-thermal Noise Spectroscopy with Parker Solar Probe/FIELDS". In: *The Astrophysical Journal Supplement* 246.2, p. 44. DOI: 10.3847/1538-4365/ab5a84.

Mozer, F. S. et al. (Feb. 2020). "Switchbacks in the Solar Magnetic Field: Their Evolution, Their Content, and Their Effects on the Plasma". In: *The Astrophysical Journal Supplement* 246.2, p. 68. DOI: 10.3847/1538-4365/ab7196.

Mozer, F. S. et al. (July 2021). "On the Origin of Switchbacks Observed in the Solar Wind". In: *The Astrophysical Journal* 919.1, p. 60. DOI: 10.3847/1538-4357/ac110d.

Müller, D. et al. (July 2013). "Solar Orbiter - Exploring the Sun-Heliosphere Connection". In: *Solar Physics* 285, pp. 25–70. DOI: 10.1007/s11207-012-0085-7.

Muschietti, L, MV Goldman, and D Newman (1985). "Quenching of the beam-plasma instability by large-scale density fluctuations in 3 dimensions". In: *Solar physics* 96.1, pp. 181–198.

Musmann, G., F. M. Neubauer, and E. Lammers (1977). "Radial variation of the interplanetary magnetic field between 0.3 AU and 1.0 AU". In: *Journal of Geophysics / Zeitschrift für Geophysik* 42.6, pp. 591–598.

Neugebauer, M. (2006). “Comment on the abundances of rotational and tangential discontinuities in the solar wind”. en. In: *Journal of Geophysical Research* 111.A4, A04103. ISSN: 0148-0227. DOI: 10.1029/2005JA011497.

Neugebauer, M. et al. (1984). “A reexamination of rotational and tangential discontinuities in the solar wind”. en. In: *Journal of Geophysical Research* 89.A7, p. 5395. ISSN: 0148-0227. DOI: 10.1029/JA089iA07p05395.

Neugebauer, Marcia and Conway W. Snyder (Oct. 1966). “Mariner 2 Observations of the Solar Wind, 1, Average Properties”. In: *Journal of Geophysical Research* 71, p. 4469. DOI: 10.1029/JZ071i019p04469.

Owens, M. J. and R. J. Forsyth (Nov. 2013). “The Heliospheric Magnetic Field”. In: *Living Reviews in Solar Physics* 10. DOI: 10.12942/lrsp-2013-5.

Parker, E. N. (Nov. 1958). “Dynamics of the Interplanetary Gas and Magnetic Fields.” In: *The Astrophysical Journal* 128, p. 664. DOI: 10.1086/146579.

— (Sept. 1965). “Dynamical Theory of the Solar Wind”. In: *Space Science Reviews* 4.5-6, pp. 666–708. DOI: 10.1007/BF00216273.

Perrone, D. et al. (Jan. 2013). “Vlasov Simulations of Multi-ion Plasma Turbulence in the Solar Wind”. In: 762.2, 99, p. 99. DOI: 10.1088/0004-637X/762/2/99. arXiv: 1207.5379 [physics.space-ph].

Phan, T. D. et al. (Feb. 2020). “*Parker Solar Probe* In Situ Observations of Magnetic Reconnection Exhausts during Encounter 1”. en. In: *The Astrophysical Journal Supplement Series* 246.2, p. 34. ISSN: 1538-4365. DOI: 10.3847/1538-4365/ab55ee.

Pick, M. and N. Vilmer (Oct. 2008). “Sixty-five years of solar radioastronomy: flares, coronal mass ejections and Sun Earth connection”. In: *The Astronomy and Astrophysics Review* 16, pp. 1–153. DOI: 10.1007/s00159-008-0013-x.

Pierrard, Viviane, Milan Maksimovic, and Joseph Lemaire (June 2001). “Core, Halo and Strahl Electrons in the Solar Wind”. In: *Astrophysics and Space Science* 277, pp. 195–200. DOI: 10.1023/A:1012218600882.

Pulupa, M. et al. (Mar. 2017). “The Solar Probe Plus Radio Frequency Spectrometer: Measurement requirements, analog design, and digital signal processing”. In: *Journal of Geophysical Research (Space Physics)* 122.3, pp. 2836–2854. DOI: 10.1002/2016JA023345.

Pulupa, M. et al. (Mar. 2017). “The Solar Probe Plus Radio Frequency Spectrometer: Measurement requirements, analog design, and digital signal processing". en. In: *Journal of Geophysical Research: Space Physics* 122.3, pp. 2836–2854. ISSN: 2169-9380, 2169-9402. DOI: 10.1002/2016JA023345.

Reid, Hamish Andrew Sinclair and Heather Ratcliffe (July 2014). "A review of solar type III radio bursts". en. In: *Research in Astronomy and Astrophysics* 14.7, pp. 773–804. ISSN: 1674-4527. DOI: 10.1088/1674-4527/14/7/003.

Robinson, P. A. (May 1992). "Clumpy Langmuir waves in type III radio sources". en. In: *Solar Physics* 139.1, pp. 147–163. ISSN: 0038-0938, 1573-093X. DOI: 10.1007/BF00147886.

Rouillard, Alexis P. et al. (2021). "The Solar Wind". In: *Solar Physics and Solar Wind*. Ed. by Nour E. Raouafi et al. Geophysical Monograph Series. Washington, DC: American Geophysical Union (AGU). Chap. 1, pp. 1–33. ISBN: 9781119815600. DOI: 10.1002/9781119815600.ch1.

Ruffolo, D. et al. (Oct. 2020a). "Shear-driven Transition to Isotropically Turbulent Solar Wind Outside the Alfvén Critical Zone". In: *The Astrophysical Journal* 902.2, p. 94. DOI: 10.3847/1538-4357/abb594.

— (Oct. 2020b). "Shear-driven Transition to Isotropically Turbulent Solar Wind Outside the Alfvén Critical Zone". In: *The Astrophysical Journal* 902.2, p. 94. DOI: 10.3847/1538-4357/abb594.

Sagdeev, R. Z. and A. Galeev (1969). *Nonlinear plasma theory*. W.A. Benjamin, 1969.

Santolík, O., M. Parrot, and F. Lefeuvre (Feb. 2003). "Singular value decomposition methods for wave propagation analysis: SVD methods for wave propagation analysis". en. In: *Radio Science* 38.1. ISSN: 00486604. DOI: 10.1029/2000RS002523.

Scarf, F. L. et al. (1971). "Nonthermal electrons and high-frequency waves in the upstream solar wind, 1. Observations". In: *Journal of Geophysical Research* 76.22, pp. 5162–5171. ISSN: 0148-0227. DOI: 10.1029/ja076i022p05162.

Schwadron, N. A. and D. J. McComas (Mar. 2021). "Switchbacks Explained: Super-Parker Fields—The Other Side of the Sub-Parker Spiral". In: *The Astrophysical Journal* 909.1, 95, p. 95. DOI: 10.3847/1538-4357/abd4e6.

Söding, A. et al. (2001). "Radial and latitudinal dependencies of discontinuities in the solar wind between 0.3 and 19 AU and -80 ° and +10 °". en. In: *Annales Geophysicae* 19.7, pp. 667–680. ISSN: 1432-0576. DOI: 10.5194/angeo-19-667-2001.

Sonnerup, Bengt U. Ö. and Maureen Scheible (Jan. 1998). "Minimum and Maximum Variance Analysis". In: *ISSI Scientific Reports Series* 1, pp. 185–220.

Squire, J., B. D. G. Chandran, and R. Meyrand (Mar. 2020). "In-situ Switchback Formation in the Expanding Solar Wind". In: *The Astrophysical Journal Letters* 891.1, p. L2. DOI: 10.3847/2041-8213/ab74e1.

Stansby, D. et al. (Mar. 2019). "Alpha particle thermodynamics in the inner heliosphere fast solar wind". en. In: *Astronomy & Astrophysics* 623, p. L2. ISSN: 0004-6361, 1432-0746. DOI: 10.1051/0004-6361/201834900.

Sterling, Alphonse C. and Ronald L. Moore (June 2020). "Coronal-jet-producing Minifilament Eruptions as a Possible Source of Parker Solar Probe Switchbacks". In: *The Astrophysical Journal Letters* 896.2, p. L18. DOI: 10.3847/2041-8213/ab96be.

Stix, Thomas Howard (1992). *Waves in plasmas*. American Institute of Physics.

Sturrock, P. A. (1964). "Type III Solar Radio Bursts". In: *NASA Special Publication*. Vol. 50, p. 357.

Suchy, Kurt (Nov. 1981). "Real Hamilton equations of geometric optics for media with moderate absorption". en. In: *Radio Science* 16.6, pp. 1179–1182. ISSN: 00486604. DOI: 10.1029/RS016i006p01179.

Tenerani, Anna and Marco Velli (Nov. 2018). "Nonlinear Firehose Relaxation and Constant- B Field Fluctuations". en. In: *The Astrophysical Journal* 867.2, p. L26. ISSN: 2041-8213. DOI: 10.3847/2041-8213/aaec01.

Tenerani, Anna et al. (Oct. 2021). "Evolution of Switchbacks in the Inner Heliosphere". In: *The Astrophysical Journal Letters* 919.2, p. L31. DOI: 10.3847/2041-8213/ac2606.

Tsurutani, B. T. et al. (Oct. 1994). "The relationship between interplanetary discontinuities and Alfvén waves: Ulysses observations". en. In: *Geophysical Research Letters* 21.21, pp. 2267–2270. ISSN: 00948276. DOI: 10.1029/94GL02194.

van Driel-Gesztelyi, L. et al. (Nov. 2012). "Magnetic Topology of Active Regions and Coronal Holes: Implications for Coronal Outflows and the Solar Wind". In: *Solar Physics* 281.1, pp. 237–262. DOI: 10.1007/s11207-012-0076-8.

Vasquez, Bernard J. and Joseph V. Hollweg (Jan. 1998). "Formation of spherically polarized Alfvén waves and imbedded rotational discontinuities from a small number of entirely oblique waves". In: *Journal of Geophysical Research* 103.A1, pp. 335–348. DOI: 10.1029/97JA02992.

Velli, M. et al. (Oct. 2020). "Understanding the origins of the heliosphere: integrating observations and measurements from Parker Solar Probe, Solar Orbiter, and other space- and ground-based observatories". In: *Astronomy and Astrophysics* 642, A4, A4. DOI: 10.1051/0004-6361/202038245.

Verniero, J. L. et al. (Apr. 2020). "Parker Solar Probe observations of proton beams simultaneous with ion-scale waves". en. In: *The Astrophysical Journal Supplement Series* 248.1, p. 5. ISSN: 1538-4365. DOI: 10.3847/1538-4365/ab86af.

Verscharen, Daniel and Benjamin D. G. Chandran (Jan. 2013). "The dispersion relations and instability thresholds of oblique plasma modes in the presence of an ion beam". en. In: *The Astrophysical Journal* 764.1, p. 88. ISSN: 0004-637X, 1538-4357. DOI: 10.1088/0004-637X/764/1/88.

Verscharen, Daniel et al. (2021). "A Case for Electron-Astrophysics". In: *Experimental Astronomy*. DOI: 10.1007/s10686-021-09761-5.

Viall, Nicholeen M. and Joseph E. Borovsky (July 2020). "Nine Outstanding Questions of Solar Wind Physics". In: *Journal of Geophysical Research (Space Physics)* 125.7, e26005. DOI: 10.1029/2018JA026005.

Vidotto, Aline A. (2021). "The evolution of the solar wind". In: *Living Reviews in Solar Physics* 18.1, p. 3. DOI: 10.1007/s41116-021-00029-w.

Voshchepynets, A. and V. Krasnoselskikh (Dec. 2015). "Probabilistic model of beam-plasma interaction in randomly inhomogeneous solar wind". en. In: *Journal of Geophysical Research: Space Physics* 120.12, pp. 10,139–10,158. ISSN: 21699380. DOI: 10.1002/2015JA021705.

Voshchepynets, A. et al. (June 2015). "Probabilistic model of beam-plasma interaction in randomly inhomogeneous plasma". en. In: *The Astrophysical Journal* 807.1, p. 38. ISSN: 1538-4357. DOI: 10.1088/0004-637X/807/1/38.

Vourlidas, Angelos et al. (Dec. 2016). "The Wide-Field Imager for Solar Probe Plus (WISPR)". In: *Space Science Reviews* 204.1-4, pp. 83–130. DOI: 10.1007/s11214-014-0114-y.

Wang, Y. M. (Dec. 1994). "Two Types of Slow Solar Wind". In: *The Astrophysical Journal Letters* 437, p. L67. DOI: 10.1086/187684.

Wang, Y. M. and Jr. Sheeley N. R. (June 1990). "Solar Wind Speed and Coronal Flux-Tube Expansion". In: *The Astrophysical Journal* 355, p. 726. DOI: 10.1086/168805.

Whittlesey, Phyllis L. et al. (Mar. 2020). "The Solar Probe ANalyzers—Electrons on the *Parker Solar Probe*". en. In: *The Astrophysical Journal Supplement Series* 246.2, p. 74. ISSN: 1538-4365. DOI: 10.3847/1538-4365/ab7370.

Woodham, L. D. et al. (June 2021). “Enhanced proton parallel temperature inside patches of switchbacks in the inner heliosphere”. In: *Astronomy and Astrophysics* 650, p. L1. DOI: 10.1051/0004-6361/202039415.

Woolley, Thomas et al. (Oct. 2020). “Proton core behaviour inside magnetic field switchbacks”. en. In: *Monthly Notices of the Royal Astronomical Society* 498.4, pp. 5524–5531. ISSN: 0035-8711, 1365-2966. DOI: 10.1093/mnras/staa2770.

Woolley, Thomas et al. (Nov. 2021). “Plasma properties, switchback patches, and low α-particle abundance in slow Alfvénic coronal hole wind at 0.13 au”. In: *Monthly Notices of the Royal Astronomical Society* 508.1, pp. 236–244. DOI: 10.1093/mnras/stab2281.

Xu, F. and J. E. Borovsky (Jan. 2015). “A new four-plasma categorization scheme for the solar wind”. In: *Journal of Geophysical Research (Space Physics)* 120, pp. 70–100. DOI: 10.1002/2014JA020412.

Yamauchi, Y. et al. (Apr. 2004). “The Magnetic Structure of Hα Macrospicules in Solar Coronal Holes”. In: *The Astrophysical Journal* 605.1, pp. 511–520. DOI: 10.1086/381240.

Yang, Liu et al. (Apr. 2019). “Electron Acceleration by ICME-driven Shocks at 1 au”. In: 875.2, p. 104. DOI: 10.3847/1538-4357/ab1133.

Zank, G. P. et al. (Nov. 2020). “The Origin of Switchbacks in the Solar Corona: Linear Theory”. In: *The Astrophysical Journal* 903.1, 1, p. 1. DOI: 10.3847/1538-4357/abb828.

Andrea LAROSA

Contraintes sur les mécanismes de génération des Switchbacks et modélisation des signatures magnétiques des Modes Extraordinaires Lents : observations de Parker Solar Probe

Résumé :

La mission Parker Solar Probe, qui a été lancée en 2018, est la première à pénétrer profondément dans la couronne solaire, ouvrant de nouvelles perspectives pour étudier in situ le jeune vent solaire jusqu'à 9.85 rayons solaires du Soleil. Parmi les principales découvertes de la mission figure l'omniprésence de brusques inversions du champ magnétique appelées switchbacks. Ces structures suscitent un fort intérêt mais leur origine n'est pas bien comprise. Dans cette thèse, nous présentons et étudions deux nouveaux résultats. Premièrement, nous donnons une description détaillée des propriétés locales des switchbacks et nous nous concentrons sur leurs propriétés ainsi que sur leurs frontières. Nous montrons que leur écart par rapport à l'alfvénicité et les corrélations entre le champ magnétique et la densité du plasma sont indicatifs de fluctuations de type mode lent et rapide. Ce résultat est important car il permet de contraindre les mécanismes de génération de ces structures. Nous postulons que l'instabilité du tuyau d'incendie pourrait générer certains des switchbacks. Un deuxième résultat est la première observation de la signature magnétique des modes extraordinaires lents associés aux sursauts radio solaires de type III. Pour comprendre l'apparition de ces signatures, nous fournissons un cadre théorique qui révèle une proportionnalité inverse entre l'intensité du champ magnétique et l'indice de réfraction du plasma. En utilisant des simulations de propagation d'ondes dans des plasmas inhomogènes, nous démontrons que la signature magnétique (jusqu'ici invisible) des ondes devient observable parce que les inhomogénéités de densité font chuter l'indice de réfraction.

Mots clés : Parker Solar Probe, Switchbacks, modes extraordinaires

Constraints on the Switchbacks generation mechanisms and modeling of the Slow Extraordinary Modes magnetic signatures: Parker Solar Probe observations

Summary :

The Parker Solar Probe mission, which was launched in 2018, is the first to penetrate deep into the inner solar corona, opening new opportunities for studying in situ the young solar wind down to 9.85 solar radii from the Sun. Among the major findings of the mission is the omnipresence of sudden magnetic field reversals called switchbacks. These structures have received considerable attention but their origin is still unclear. In this thesis we present and investigate two novel results. First we give a detailed description of the local properties of switchbacks and focus on their properties and on their boundaries. We show that their deviation from alfvénicity and the correlations between magnetic field and plasma density are indicative of slow and fast mode-type fluctuations. This result is important as it helps constrain the possible generation mechanisms. We argue that the firehose instability could generate some of the switchbacks. A second result is the first observation of the magnetic signature of slow extraordinary modes associated with type III solar radio bursts. To understand the occurrence of these signatures we provide a theoretical framework that reveals an inverse proportionality between the intensity of the magnetic field and the plasma refractive index. Using simulations of wave propagation in inhomogeneous plasmas, we demonstrate that the (hitherto unseen) magnetic signature of the waves become observable because density inhomogeneities cause the refractive index to drop

Keywords : Parker Solar Probe, Switchbacks, Slow Extraordinary Modes

LPC2E, 3 Av. de la Recherche Scientifique,
45071 Orléans, France